Quantum Effects in Atomic Nanofabrication Using Light Forces

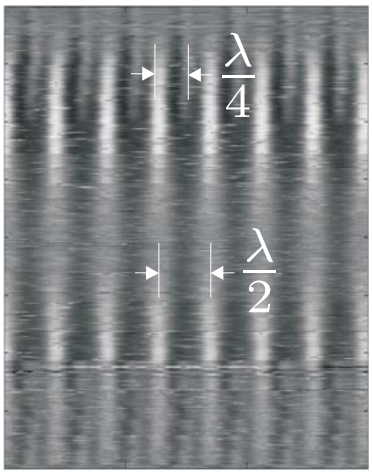

Dissertation

zur Erlangung des akademischen Grades des
Doktors der Naturwissenschaften
(Dr. rer. nat.)

an der Universität Konstanz
Mathematisch-Naturwissenschaftliche Sektion
Fachbereich Physik

vorgelegt von
Dirk Jürgens
Juni 2004

Zusammenfassung

Ziel dieser Arbeit war die Untersuchung der atomaren Nanofabrikation mit Lichtkräften im Quantenregime. In den vorangegangenen Arbeiten wurde für die nanostrukturierte Deposition neutraler Atome stets die klassisch beschreibbare induzierte Dipolkraft in weit verstimmten stehenden Lichtwellen verwendet. In exakt resonanten Lichtfeldern erwartet man aber klassisch keine Dipolkraft, da in diesem Fall der induzierte Dipol des Atoms und das Lichtfeld um 90° außer Phase schwingen. Quantenmechanisch befindet sich ein atomares Grundzustandswellenpaket, das sich in einem exakt resonanten Lichtfeld bewegt, in einer Superposition, die zu gleichen Teilen aus den Eigenzuständen des gekoppelten Systems, den so genannten dressed states besteht. Ist die Intensitätsverteilung des Lichtfeldes inhomogen, so erfahren die beiden dressed-state-Wellenpakete eine Kraftwirkung proportional zum Intensitätsgradienten, aber in entgegengesetzte Richtung. Während ein Teil zum Intensitätsmaximum gezogen wird, erfährt der andere Teil eine Kraftwirkung zum Intensitätsminimum. Verwendet man nun im atomaren Nanofabrikationsexperiment eine exakt resonante stehende Lichtwelle, führt dieser Effekt zu einer Halbierung der Periodizität der Nanostrukturen, so dass das für Zwei-Niveau Systeme gültige $\frac{\lambda}{2}$-Limit des konventionellen Schemas unterboten wird. Desweiteren zeigen die durchgeführten Experimente, dass die atomare Bewegung im resonanten Lichtfeld nicht nur durch die Kraftwirkung eines Intensitätsgradienten, sondern auch durch den Phasengradienten des Lichtfeldes am Knoten einer nicht perfekten stehenden Welle bestimmt wird.

Ein weiterer Schwerpunkt der Arbeit war die Herstellung exakt periodisch angeordneter ferrimagnetischer Nanostrukturen. Dafür wurde die Anlage so umgebaut, dass die Nanostrukturen jetzt unter definierten Ultrahochvakuumbedingungen wachsen können. Um die Proben anschließend in die Molekularstrahlepitaxieanlage der Arbeitsgruppe Schatz transferieren zu können musste sie entsprechend kompatibel gestaltet werden.

Basierend auf dem klassischen, weitverstimmten Nanofabrikationsschema konnten in der Ultrahochvakuumanlage reine Proben mit Chromnanostrukturen hohen Kontrastes produziert werden. Anschließend gelang der Transport in die Molekularstrahlepitaxieanlage, wo anschließend eine Platinschicht auf den Nanostrukturen abgeschieden wurde. Leider haben technische Probleme in der Epitaxieanlage den thermischen Annealingprozess, der letztendlich zur ferrimagnetischen Phase des Chrom-Platin-Systems führen sollte, bislang verhindert.

Für die Erzeugung strukturierter ferrimagnetischer Nanolegierungen, aber auch für andere mögliche Anwendungen, ist es von entscheidender Bedeutung, dass die deponierten Nanostrukturen ein hohes Kontrastverhältnis aufweisen, d.h. der Untergrund muss soweit wie möglich reduziert werden. Weit rotverstimmte stehende Wellen sind dafür besser geeignet, da die Form des Dipolpotentials, das die Fokussierung des Atomstrahls

bestimmt, sehr viel harmonischer ist als im blauverstimmten Fall, obwohl der Einfluss der spontanen Emission eher das Gegenteil vermuten ließe. Die experimentellen Untersuchungen zeigen, dass der Untergrund im rotverstimmten Fall auf 13% reduziert wird, was auch mit theoretischen Rechnungen sehr gut übereinstimmt.

Contents

1 Introduction

1.1 Entering the Nano Age

The rapid development of nanotechnology during the past decade has now entered a phase where the inventions and discoveries made, become more and more attractive for the economy. A true economic boom is expected and it is believed that 'nanotechnology will be the next major growth innovation' (Fleischhauer, 2004). The revolutionary devices and products that are anticipated to emerge from the nanoworld comprise nearly all fields of everyday life. The textile industry, for example, pursues the development of fabrics made of polymer nanofibers produced by electro-spinning. These materials are promising candidates for specialty filters and protective clothing as well as for biomedical applications, in particular tissue engineering (Dersch *et al.*, 2003). Besides that, nanoengineered devices like nanobots, smart medical agents that are injected into blood circulation, might revolutionize many fields of medical and natural sciences. Overall, it is estimated that nanotechnology has a market potential of 1000 billion US$ according to the National science foundation (Fleischhauer, 2004).

Within the sixth framework program of European Union the issue of nanotechnologies is among the top priority fields of research that are financially supported. For the years 2002-2006, the total budget of the sixth framework program amounts to 17.5 billion€, which shows that the european research politics also sets large hopes into nanotechnology.

These trends accompany the development in the semiconductor industry towards smaller and faster computer chips that lasts for several decades already. In this context one often refers to the famous Moore's law that states that the number of transistors on a chip quadruples every three years (Moore, 1965). According to the SIA roadmap for the semiconductor industry, 'lithography continues to be the key enabler for the semiconductor industry' (SIA, 2003). The currently used ultraviolet wavelength for photolithographic systems is 193nm and structure sizes of around 100nm are reached. However, it is already foreseeable that in the near future alternative nanostructuring concepts are required to keep up the pace of innovation. Industry strongly prefers the development of compact plasma sources that generate extreme ultraviolet radiation at a wavelength of 13nm for next generation lithography[1]. Lithography projection systems based on this technology will begin to dominate the chip production market in the second half of this decade.

Besides these conventional optical lithography technologies there is increasing interest in different strategies for nanofabrication. Aside from charged particle techniques like

[1] Just recently the development of optical lithography at 157nm was stopped because of incalculable technological and financial risks.

electron-beam or ion-beam lithography with resolutions of only few nanometer that are nowadays used for optical lithography mask production, a plethora of alternative methods was established that proved successful in the realization of nanostructures. Among these, only scanning-probe techniques that achieve atomic resolution shall be mentioned here (Eigler and Schweitzer, 1990; Manoharan *et al.*, 2000).

Electron-beam and ion-beam lithography utilize static electric or magnetic fields to focus and guide a beam of charged particles onto a sensitive resist layer. These methods offer the great advantage that any arbitrary pattern can be written serially with high accuracy what makes these machines unrivaled on this field.

Since the 1980s novel nanofabrication schemes based on manipulating the trajectories of neutral atoms were investigated. Neutral atoms from a thermal source have extremely short de Broglie wavelengths of typically only few picometers and thus one could in principal achieve resolutions of few nanometers. But to manipulate the trajectories of neutral atoms in such a way that a nanostructured topography on a surface is produced, one has to utilize the interaction of near-resonant laser fields with the induced dipole moment of an atom, or magnetic fields that act on the magnetic moment. Therefore, the range of potential applications for neutral atom based nanofabrication, or atomic nanofabrication, is limited to some special cases. Nonetheless, the method has specific strengths that make it attractive for further research. From a fundamental point of view, the method is interesting because the deposition technique allows to detect the position of atoms with nanometer resolution and thus allows to study the interaction of atoms with light or magnetic fields at highest accuracy. Furthermore, the atomic nanofabrication is perfectly suited to fabricate periodic arrays in one, two and three dimensions because standing wave light fields that act as focusing masks for atoms are intrinsically periodic with spectroscopic accuracy[2]. A third aspect that provides a large potential for neutral atom nanofabrication is the compatibility with epitaxial methods. This opens up the way towards novel periodically nanostructured materials such as wood pile structures discussed in the context of photonic crystals.

1.2 Atomic Nanofabrication Using Light Forces

The field of atom optics has seen an enormous boom through the advent of laser cooling techniques (Phillips and Metcalf, 1982), the availability of tunable laser sources and a detailed understanding of the atom-light interaction. The purpose of atom optics is to gain control over the atomic motion by manipulating neutral atoms in the same way as light by optical elements such as mirrors, lenses, waveguides, resonators, interferometers, diffraction gratings etc. In particular the manipulation of atomic trajectories by light or magnetic forces is very attractive because the interaction strengths can be efficiently tuned. The earliest work that demonstrated such forces goes back to Stern and Gerlach in the 1920s who showed that inhomogeneous magnetic fields exert a force on atomic magnetic moments (Gerlach and Stern, 1921). Soon afterwards Frisch showed that an atomic beam can be deflected by light pressure (Frisch, 1933). But it took almost another 50 years to realize the first focusing of an atomic beam in a near-resonant co-propagating laser beam using light forces (Bjorkholm *et al.*, 1978).

[2]For this reason, these nanostructures are perfectly suited as calibration standards in the nanometer regime.

The extension of atom lenses based on optical forces towards nanofabrication was demonstrated in 1992 (Timp *et al.*, 1992) where a near-resonant optical standing wave with a period of $\frac{\lambda}{2} = 294.5$nm was employed to grow an array of periodic sodium lines with structure widths of only 15nm FWHM[3] on a surface. The standing light wave field acts as an array of cylindrical lenses for atoms.

After this pioneering experiment several groups started with atomic nanofabrication experiments based on the same scheme but now with more suitable atomic elements.

1.2.1 Elements for Atomic Nanofabrication

In the groups of J. J. McClelland at the National Institute of Standards and Technology (NIST) and J. Mlynek at University Konstanz two atomic nanofabrication experiments with chromium were built and the majority of new nanostructures were realized. Using chromium in the standard one dimensional standing wave setup structure widths of 28nm and periodicity of $\frac{\lambda}{2} = 213$nm were reported from the NIST group (Anderson *et al.*, 1999). In the group of S. A. Lee at Colorado State University direct deposition with aluminum in one dimensional standing waves was demonstrated and nanostructures with a period of $\frac{\lambda}{2} = 155$nm were realized. In particular chromium has proven to be an excellent material for atomic nanofabrication using light forces because its atomic level scheme provides closed dipole transitions at wavelengths accessible by state-of-the-art laser sources, and the grown nanostructures are robust and can thus be analyzed in air with an atomic force microscope (AFM). Just recently the first successful depositions of iron nanostructures were reported (te Sligte, 2004). Furthermore several groups are currently working towards direct deposition of the technologically interesting group III elements gallium (Rehse *et al.*, 2001; Marago, 2003) and indium (Meschede and Metcalf, 2003).

However, the level schemes of iron and aluminum are less advantageous because the optical transitions used for lasers cooling are not closed so that one either has to apply repumping lasers or a large structure background will grow. Nanofabrication with chromium, aluminum, sodium and iron is typically referred to as direct deposition nanofabrication since the interaction of the atomic beam with a standing wave light field leads to a direct growth of a nanostructured array on a surface. Besides that, a second scheme has been developed that utilizes the chemical modification of a resist material on a surface and subsequent etching to fabricate nanostructures (Berggren *et al.*, 1995). This technique has so far been employed for four chemical elements: the metastable noble gases argon, helium, neon and the alkali metal cesium. A comprehensive overview of the results on atomic nanofabrication based on lithography techniques is given in (Meschede and Metcalf, 2003). Because the latter method is similar to optical lithography techniques, the nomenclature used in this thesis is such that direct deposition is simply called atomic nanofabrication and the schemes based on resist technique are called atom lithography.

1.2.2 Extension Towards Higher Dimensions

The demonstration that neutral atoms can be utilized to realize nanostructures with resolutions distinctly below 100nm have lead to further efforts to extend the method to-

[3]Full width at half maximum.

wards higher dimensions, smaller feature sizes and smaller feature spacings. The extension to two dimensional structures was achieved by using two perpendicularly arranged orthogonally polarized standing waves. The resulting light pattern represents a square lattice and leads to a corresponding chromium nanodot pattern with feature spacings of $\frac{\lambda}{2} = 213$nm and structure sizes of 80nm on the surface (Gupta *et al.*, 1995; Schulze *et al.*, 2000). Further periodic two dimensional patterns utilizing multiple-beam interference were subsequently demonstrated. An detailed review of the demonstrated work is given in (Oberthaler and Pfau, 2003).

Arbitrary patterns can not be easily realized because the decomposition of a desired light field distribution into the corresponding wave vectors is not known in general, however it would certainly require a multitude of laser beams (Meschede and Metcalf, 2003). A first step towards more complex, not strictly periodic patterns was demonstrated in the group of D. Meschede at University Bonn (Mützel *et al.*, 2002). They used a volume hologram stored in a photorefractive crystal to produce a complex interference pattern that acted as the focusing mask.

One of the largest potentials for applications of atomic nanofabrication is the possibility to extend it to three dimensions. Since the focusing mask for atoms relies on the resonant interaction of the laser light with an atomic dipole, such a light field will only focus the atoms when their resonance frequency is near the frequency of the laser. Other materials will not be affected by the light field. Thus a co-deposition of two materials will lead to a film with structured doping because only one atomic species is addressed. This scheme was demonstrated in our group in the early stage of my thesis work with a two component beam of chromium and magnesium fluoride (MgF_2) where chromium was the dopant and MgF_2 the host material (Schulze *et al.*, 2001). The potential of this method lies in its extensibility to ultra high vacuum conditions necessary for molecular-beam epitaxy and extension to other materials. The combination of group III and V materials would allow to grow laterally modulated heterostructures (Rehse *et al.*, 2000). This could open up the way to create complex three-dimensional electronic potentials, e.g. channel-like three-dimensional conductor networks.

In any case, the step towards clean nanostructures fabricated in ultra high vacuum is essential for further application and comes along with the goals of improved nanostructure contrast of the produced nanostructures. Both objectives are pursued in this thesis and will be extensively discussed. A material system of special interest is the ferrimagnetic phase of chromium-platinum alloys. Using our method to produce low background chromium nanostructures is the starting point for the fabrication of ferrimagnetic nanoalloys periodically arranged on a substrate. This work was pursued in collaboration with the group of Professor Schatz.

1.2.3 Period Reduction Schemes: Quantum Mechanics

Another important aspect for applications is the problem of attainable feature spacings. From a classical standpoint, atomic nanofabrication using light forces cannot overcome the resolution limit of $\frac{\lambda}{2}$ given by the highest spatial resolution of the patterning light masks. However, smaller feature spacings can be achieved using classical light forces by using a double exposure technique (Schulze *et al.*, 1999): for this purpose, two depositions are performed one after another. First, the detuning is chosen negative and afterwards positive. Depending on the sign of the detuning, the dipole potential associated with

the intensity distribution changes its sign and, thus, atoms are attracted either to the intensity maxima or minima. Using this scheme, one dimensional nanostructures with a periodicity of $\frac{\lambda}{4}$ were demonstrated[4].

Another method that can be used to significantly reduce the feature spacings relies on the chromium specific polarization dependence of the atom-light interaction. Light forces do also arise from light fields with constant intensity but position dependent polarization. This effects is also the basis for Sisyphus laser cooling (Dalibard and Cohen-Tannoudji, 1989). The chromium atom consists of 16 magnetic substates whose interaction energy with the light field depends on the polarization. In the special case of a light field that constitutes of two counterpropagating orthogonally polarized light waves, one can show that the minima of the corresponding light potentials for the different magnetic substates are spaced at only $\frac{\lambda}{8}$ and thus a significant reduction of the periodicity is achieved (Gupta *et al.*, 1996). Later, in our group this scheme was extended to two dimensions utilizing a light field made of three orthogonally polarized beams (Brezger *et al.*, 1999). A drawback of this method is, that it is based on the specific magnetic substructure of chromium and thus it is not directly transferable to other elements that might be interesting for atomic nanofabrication.

A very general approach applicable to all two-level systems, that allows to reduce the periodicity of the nanostructures, can be deduced from a full quantum picture of the atom-light interaction. In the regime where the laser frequency is tuned exactly on resonance, it is expected classically that the force on the atom vanishes. However, in the quantum picture the atomic wave function will split into two parts whereas one part is attracted to intensity minima of the light field and the other part to intensity maxima. Thus one obtains a halving of the periodicity and the $\frac{\lambda}{2}$ periodicity limit is surpassed. This fundamental problem represents the third main focus of this work. It will be shown that the experiment reveals several surprising quantum features of the atom-light interaction in atomic nanofabrication.

1.3 Organization of this Thesis

This thesis is organized as follows. In chapter 2, the atom-light interaction is discussed in detail. First, a semiclassical treatment of the atomic motion in light fields will be given that is well suited to describe the case of off-resonant fields before a fully quantum mechanical description of atomic motion explains the exactly on-resonant case. Chapter 3 presents the experimental setup with special emphasis on the new ultra high vacuum system. The experimental results of this thesis work are given in chapter 4. Off-resonant light masks were studied with respect to improved applicability, in particular for the pursued work towards ferrimagnetic $CrPt_3$ nanoalloys. It will be shown how red detuned standing waves can be used to suppress the background of the structures. On-resonant light fields are a non-classical problem because the classical picture of the induced dipole force suggests that the force vanishes. It will be shown that the quantum character of the interaction results in a splitting of the atomic wave function leading to smaller periodicities of the nanostructures compared to the off-resonant case. Finally, in chapter 5 a summary of the presented work and an outlook will be given.

[4]Changing the detuning slightly alters the periodicity of the light field. This effect is however negligibly small for the detunings used in the experiments.

2 Atom-Light Interaction

Atomic nanofabrication relies on the manipulation of atoms by optical forces. The simplest example of using light forces for atomic nanofabrication is a standing wave light field perpendicular to an atomic beam because the typical dimensions of optical interferences are on the order of a half wavelength. A standing wave light field acts as an immaterial focusing mask for atoms and thus leads to a periodically modulated atomic flux. This inhomogeneous beam can now be deposited on an appropriate substrate such that periodic nanostructures on the substrate surface are formed. In this chapter, the light forces utilized for atomic nanofabrication are introduced. First, a simple classical model for the atom light interaction which is sufficient to understand the formation of nanostructures in most experiments is presented. Furthermore, the atom-light interaction will be treated quantum mechanically. This is especially important for the description of the nonclassical regime of exactly resonant light fields which is a main topic in this thesis. The quantum picture is introduced for a two-level system but it is straight forward to extend it to multi-level system as used in the experiment. In addition, the focusing properties of standing light waves will be discussed.

2.1 Classical Picture

The interaction of light with a neutral atom can be understood classically as shown in figure 2.1: Here, the atom is modelled as a harmonic oscillator with resonance frequency ω_0 that consists of two mass points with opposite charges. A linearly polarized electric field oscillating with frequency ω_l given by $\mathbf{E}(x,t) = E_0(x)\mathbf{e}_y \cos(\omega_l t)$ leads to a driving force on the electron and, thus, an electric dipole is induced as shown in figure 2.1(a). The dynamics of the electron is determined by the electric field amplitude $E_0(x)$ and the difference between driving frequency ω_l and resonance frequency ω_0 called detuning $\Delta = \omega_l - \omega_0$. For detunings much larger than the resonance linewidth the electron motion has an analytical solution

$$y(x,t) = \frac{e}{2m_e\omega_l\Delta} E_0(x)\cos(\omega_l t), \tag{2.1}$$

where e is the electron charge and m_e is the electron mass. Near resonance, the amplitude of the electron motion is resonantly enhanced. Positive detunings lead to an electron oscillation in phase with the driving field and negative detunings to an oscillation in antiphase, respectively. The electron motion induces a dipole moment $D(x,t) = -ey(x,t)$. The local interaction energy of the dipole moment with the outer electric field

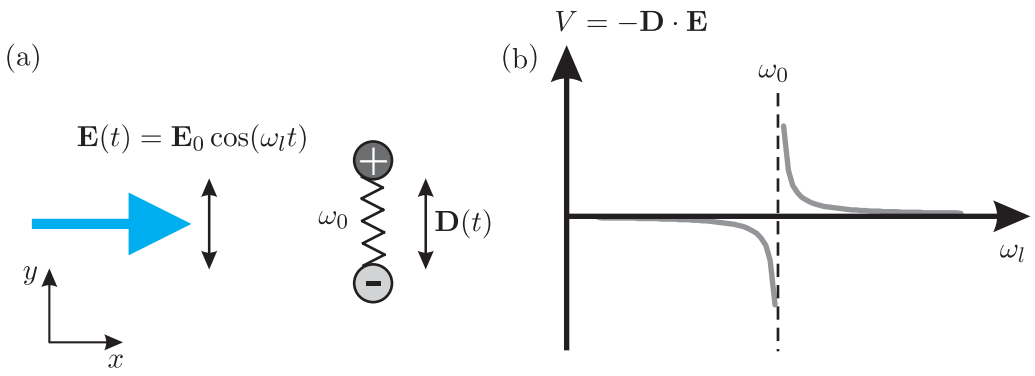

Figure 2.1: Classical picture of atom-light interaction. A linearly polarized electric field $\mathbf{E}(t)$ drives an atom modelled as a positive core with a harmonically bound electron. When the light field frequency is tuned close to the resonance frequency a time-dependent dipole moment is induced which oscillates in (out of) phase with the driving electric field if the light field frequency is below (above) the resonance frequency. The resulting interaction energy of the induced dipole and driving field is resonantly enhanced near the resonance frequency and minimized for red (blue) detuning at intensity maxima (minima).

is given by

$$V(x,t) = -\mathbf{D}(x,t) \cdot \mathbf{E}(x,t). \tag{2.2}$$

Averaging over one oscillation cycle leads to the so-called light induced potential given by

$$\langle V(x) \rangle_t = \frac{e^2}{4m_e\omega_l} \frac{E_0^2(x)}{\Delta} = \frac{e^2}{2c\epsilon_0 m_e \omega_l} \frac{I(x)}{\Delta}, \tag{2.3}$$

where c is the speed of light, ϵ_0 is the dielectric constant and $I(x)$ is the light intensity distribution. Near resonance the interaction is resonantly enhanced as shown in figure 2.1(b). The dipole force that is derived from this light induced potential determines the atomic motion according to Newton's equations of motion. It is therefore proportional to the intensity gradient of the light field. Hence, the atom is attracted to the potential minima that are found at the intensity minima for $\Delta > 0$ (low field seeker) and at the intensity maxima for $\Delta < 0$ (high field seeker), respectively.

This picture gives a qualitative understanding of the dipole force. However, this picture breaks down in the case of exact resonance. Classically, one expects that the atomic dipole oscillates at $\pi/2$ phase shifted with respect to the light field and, thus, no classical force is expected. The next section outlines a quantum mechanical description of the dipole force associated with the atom-light interaction.

2.2 Quantum Picture

In the following, a quantum mechanical derivation of the dipole force will be given. The interaction of a two-level atom with a coherent, monochromatic light field as depicted schematically in figure 2.2 will be discussed. In the absence of spontaneous emissions,

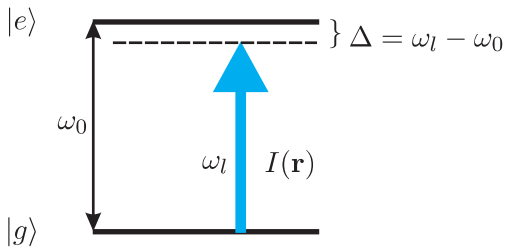

Figure 2.2: Two-level atom interacting with a near resonant light field. The atom can be described by its ground state $|g\rangle$ and excited state $|e\rangle$. The important parameters governing the interaction are the laser detuning Δ and the intensity $I(\mathbf{r})$.

the interaction is represented by a threepart Hamilton operator (Dalibard and Cohen-Tannoudji, 1985)

$$\hat{H} = \hat{H}_{\text{atom}} + \hat{H}_{\text{light}} + \hat{H}_{\text{int}}. \tag{2.4}$$

Here, the atomic Hamilton operator $\hat{H}_{\text{atom}}$ is the sum of the kinetic and internal energies of the two-level atom

$$\hat{H}_{\text{atom}} = \frac{\hat{\mathbf{p}}^2}{2m} + \frac{\hbar\omega_0}{2}\left(|e\rangle\langle e| - |g\rangle\langle g|\right), \tag{2.5}$$

where $\hat{\mathbf{p}}$ is the momentum operator, m is the atomic mass, and ω_0 is the transition frequency between ground state $|g\rangle$ and excited state $|e\rangle$. The Hamiltonian for the quantized light field of a single laser mode l is

$$\hat{H}_{\text{light}} = \hbar\omega_l \hat{a}_l^\dagger \hat{a}_l, \tag{2.6}$$

where $\hat{a}_l^\dagger$ and $\hat{a}_l$ are the creation and annihilation operators for a photon with energy $\hbar\omega_l$.

In the electric dipole approximation, the interaction Hamiltonian of the atom with the light field is given by

$$\hat{H}_{\text{int}}(t) = -\hat{\mathbf{d}} \cdot \hat{\mathbf{E}}_l(\hat{\mathbf{r}}, t), \tag{2.7}$$

where $\hat{\mathbf{d}} = e\hat{\mathbf{r}}$ is the atomic dipole operator, e is electron charge and $\hat{\mathbf{E}}_l(\hat{\mathbf{r}}, t)$ is the electric field operator of mode l. In this notation, $\hat{\mathbf{r}}$ is the atomic position operator.

Depending on the physical situation the dynamics of the two-level atom can be described either in a semiclassical picture, where the atom is treated as a classical particle, or fully quantum mechanically: the atom is then treated as a wave packet and the dynamics is described in terms of matter wave propagation. For most experimental situations of atomic nanofabrication however the particle picture is adequate. Therefore, in the following the semiclassical dressed-atom approach for a two-level atom is introduced. Afterwards, the spontaneous emission rates between different dressed levels are determined and the problem is extended to a real multi-level atom. Finally, in section 2.3 it will be shown, how standing wave light fields act as an array of focusing lenses in atomic nanofabrication.

2.2.1 Dressed States

In deriving the eigenstates of an atom in a light field, the atom itself is considered as a classical particle. Therefore, the kinetic part of the two-level atom Hamilton operator

$\hat{H}_{\text{atom}}$ given in equation 2.5 may be neglected. The temporal evolution of the atomic state $|\Psi\rangle$ is described by the explicitly time-dependent Schrödinger equation

$$i\hbar\frac{\mathrm{d}}{\mathrm{d}t}|\Psi\rangle = \hat{H}|\Psi\rangle, \tag{2.8}$$

where the Hamilton operator $\hat{H}$ is given in equation 2.4. By solving this equation, the new eigenenergies corresponding to the light-induced potential associated with the atom-light interaction and the new eigenstates of the coupled atom-light system can be deduced. The atomic position operator is replaced by its average value $\langle\hat{\mathbf{r}}\rangle = \mathbf{r}$. Furthermore, the light field is treated classically as well. The total Hamilton operator (equation (2.4)) describing the atom light interaction therefore simplifies to

$$\hat{H} = \hat{H}_{\text{atom}} + \hat{H}_{\text{int}} = \frac{\hbar\omega_0}{2}\left(|e\rangle\langle e| - |g\rangle\langle g|\right) - \hat{\mathbf{d}}\cdot\mathbf{E}_l(\mathbf{r})\cos(\omega_l t). \tag{2.9}$$

The atom-laser coupling is characterized by the complex Rabi frequency defined by

$$\Omega(\mathbf{r}) = \Omega_0(\mathbf{r})\mathrm{e}^{i\varphi(\mathbf{r})} = -\mathbf{E}_l(\mathbf{r})\frac{\langle e|\hat{\mathbf{d}}|g\rangle}{\hbar}. \tag{2.10}$$

The magnitude of the Rabi frequency depends on the intensity $I(\mathbf{r})$ of the light field

$$\Omega_0(\mathbf{r}) = \Gamma\sqrt{\frac{I(\mathbf{r})}{2I_{\text{sat}}}}, \tag{2.11}$$

where Γ is the natural linewidth of the transition and $I_{\text{sat}} = \frac{\hbar\Gamma\omega_0^3}{12\pi c^2}$ is the corresponding saturation intensity. The phase of the Rabi frequency is derived from the electric field components that constitute the total light field.

In the $|g\rangle, |e\rangle$ basis the Hamilton operator in matrix notation reads

$$\hat{H} = \frac{\hbar}{2}\begin{pmatrix} -\omega_0 & 2\Omega(\mathbf{r})\cos(\omega_l t) \\ 2\Omega^*(\mathbf{r})\cos(\omega_l t) & \omega_0 \end{pmatrix}. \tag{2.12}$$

The time dependence is eliminated by a transformation into a frame rotating at half the excitation frequency such that

$$|g\rangle = |\tilde{g}\rangle\cdot\mathrm{e}^{\frac{i}{2}\omega_l t} \tag{2.13}$$

$$|e\rangle = |\tilde{e}\rangle\cdot\mathrm{e}^{-\frac{i}{2}\omega_l t}. \tag{2.14}$$

All terms with $\mathrm{e}^{\pm 2i\omega_l t}$ may be neglected. This is the well known rotating wave approximation. In the $|\tilde{g}\rangle, |\tilde{e}\rangle$ basis, the Hamilton operator then simplifies to

$$\tilde{H} = \frac{\hbar}{2}\begin{pmatrix} \Delta & \Omega_0(\mathbf{r})\mathrm{e}^{i\phi(\mathbf{r})} \\ \Omega_0(\mathbf{r})\mathrm{e}^{-i\varphi(\mathbf{r})} & -\Delta \end{pmatrix}, \tag{2.15}$$

where the laser detuning $\Delta = \omega_l - \omega_0$ was introduced. The atom-light interaction leads to off-diagonal elements in the 2×2 matrix. Therefore, $|g\rangle$ and $|e\rangle$ are no longer eigenstates of the coupled two-level atom. The new eigenstates are obtained by diagonalizing the

new Hamilton operator given in equation (2.15) by a unitary transformation according to

$$\hat{\tilde{H}}' = \hat{U}^\dagger \hat{\tilde{H}} \hat{U}, \qquad \text{where} \qquad \hat{U}(\mathbf{r}) = \begin{pmatrix} \mathrm{e}^{i\varphi(\mathbf{r})/2}\cos\theta(\mathbf{r}) & \mathrm{e}^{i\varphi(\mathbf{r})/2}\sin\theta(\mathbf{r}) \\ -\mathrm{e}^{-i\varphi(\mathbf{r})/2}\sin\theta(\mathbf{r}) & \mathrm{e}^{-i\varphi(\mathbf{r})/2}\cos\theta(\mathbf{r}) \end{pmatrix}. \tag{2.16}$$

The angle $\theta(\mathbf{r})$ of the diagonalization matrix $\hat{U}$ is given by

$$\cos 2\theta(\mathbf{r}) = -\frac{\Delta}{\Omega_{\text{eff}}(\mathbf{r})}, \qquad \sin 2\theta(\mathbf{r}) = \frac{\Omega_0(\mathbf{r})}{\Omega_{\text{eff}}(\mathbf{r})}, \tag{2.17}$$

where $\Omega_{\text{eff}}(\mathbf{r}) = \sqrt{\Delta^2 + \Omega_0(\mathbf{r})^2}$ is the effective Rabi frequency. The new eigenstates are the so-called dressed states. They are superpositions of the bare states $|g\rangle$ and $|e\rangle$ with relative amplitudes depending on the detuning, the Rabi frequency (light intensity) and phase $\varphi(\mathbf{r})$ of the laser field, and angle $\theta(\mathbf{r})$:

$$\begin{aligned} |1;\mathbf{r}\rangle &= \mathrm{e}^{-i\varphi(\mathbf{r})/2}\sin\theta(\mathbf{r})\,|g\rangle + \mathrm{e}^{i\varphi(\mathbf{r})/2}\cos\theta(\mathbf{r})\,|e\rangle \\ |2;\mathbf{r}\rangle &= \mathrm{e}^{-i\varphi(\mathbf{r})/2}\cos\theta(\mathbf{r})\,|g\rangle - \mathrm{e}^{i\varphi(\mathbf{r})/2}\sin\theta(\mathbf{r})\,|e\rangle \end{aligned} \tag{2.18}$$

The excited state $|e\rangle$ of the atom is not stable, therefore, one can distinguish between long and short lived dressed states depending on the amplitude of the excited state. For blue detuning, state $|1\rangle$ has only a small contribution of the excited state and, thus, represents the long living state, while for red detuning, it mainly consists of the excited state and, thus, has a short lifetime. The excited state amplitude for state $|1\rangle$ in dependence on the detuning is plotted in figure 2.3. The new eigenenergies E_1, E_2 of the two-level atom in the light field are

$$E_1(\mathbf{r}) = \frac{\hbar}{2}\mathrm{sgn}(\Delta)\sqrt{\Delta^2 + \Omega_0^2(\mathbf{r})} \tag{2.19}$$

$$E_2(\mathbf{r}) = -\frac{\hbar}{2}\mathrm{sgn}(\Delta)\sqrt{\Delta^2 + \Omega_0^2(\mathbf{r})}. \tag{2.20}$$

The dressed state energies are intensity dependent, whereas the phase does not play a role. Therefore, in a light field with space dependent intensity distribution $I = I(\mathbf{r})$ the eigenenergies will also vary with position $\mathbf{r}$. It is this spatial variation of the dressed state energies that leads to the so-called dipole force on an atom.

Qualitatively, the dipole force can be understood in the following way: in a blue detuned standing wave ($\Delta > 0$) the $|1\rangle$-state is the long-lived dressed state. Just like in the classical picture (figure 2.1(b)) the dressed state energy increases in high intensity regions as shown in figure 2.4. The atom is therefore attracted to intensity minima. In the red detuned case, the situation is diametrical: the long-lived dressed state is now the $|2\rangle$-state and, thus, the atom is attracted to the intensity maxima.

The dressed state eigenenergies are schematically shown in figure 2.4 for a Gaussian laser beam. In deriving the dressed states and their eigenenergies, the light field was treated classically. But when the light field quantization is incorporated, the combined atom-laser state is described by $|k, n\rangle$, where k is the state of the atom and n is the photon number of the light field mode.

Considering this quantization, the dressed states are bunched in well-separated two-dimensional manifolds $\mathcal{E}_n$. Each manifold consists of two eigenstates separated by $\hbar\Omega$ and the different manifolds are separated by one photon energy $\hbar\omega_l$.

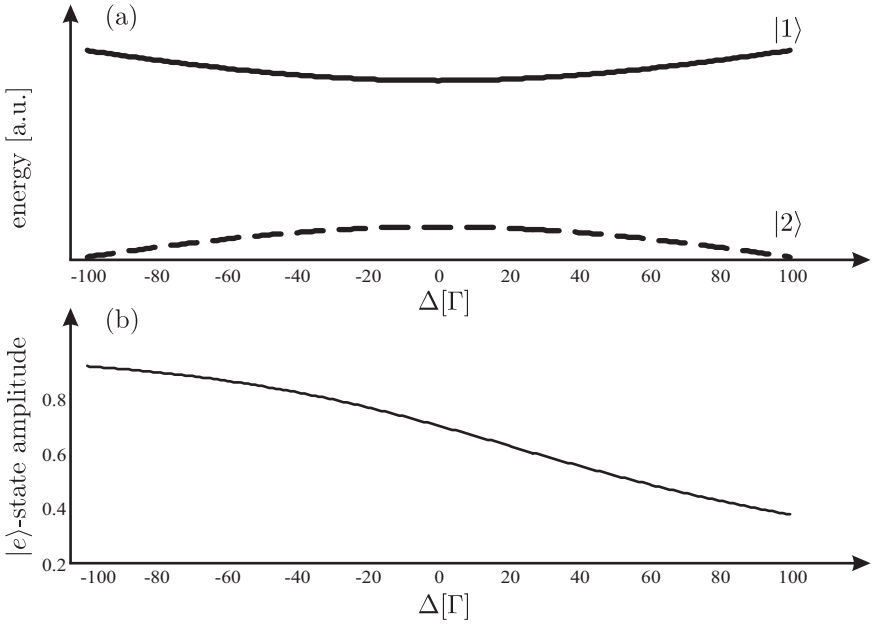

Figure 2.3: (a) Dressed state eigenenergies vs. detuning for a fixed Rabi frequency of 100Γ and (b) corresponding excited state amplitude of state $|1\rangle$. For red detuning ($\Delta < 0$) the $|1\rangle$-state mainly consists of the excited state and thus has a short lifetime while for blue detuning the $|1\rangle$-state has only a small contribution of the excited state and thus represents the long lived state.

2.2.2 Spontaneous Emission

So far, spontaneous emission processes caused by the coupling of the atom to the empty modes of the field were neglected. Nevertheless, spontaneous emissions can be incorporated into the framework of dressed states. First, a spontaneous emission between two dressed states leads to a random momentum recoil on the atom and, in general even more important, it may lead to a change of the dressed state and subsequently to fluctuations of the dipole force.

In the basis of bare states, the only allowed transition is from the $|e, n\rangle$-state to the $|g, n\rangle$-state at a rate $\Gamma \propto |\langle g|\hat{\mathbf{d}}|e\rangle|^2$. Because the dressed states are superpositions of both bare states, several transitions between dressed states are possible. Both, state changing and state preserving transitions, i.e. transitions to the same state in the lower manifold, are now allowed due to the admixture of the excited state to the dressed states. Any allowed spontaneous emissions between different dressed states are indicated on the right hand side of figure 2.4 for an atom in a Gaussian beam, where the arrow thickness indicates the transition probability. The associated transition rates can be calculated using

$$\Gamma_{i \leftarrow j} \propto |\langle i, n-1|\hat{\mathbf{d}}|j, n\rangle|^2. \tag{2.21}$$

In matrix form, the dressed state transition rates are

$$\Gamma_{i \leftarrow j} = \Gamma \begin{pmatrix} \cos^2\theta(\mathbf{r})\sin^2\theta(\mathbf{r}) & \cos^4\theta(\mathbf{r}) \\ \sin^4\theta(\mathbf{r}) & \cos^2\theta(\mathbf{r})\sin^2\theta(\mathbf{r}) \end{pmatrix}. \tag{2.22}$$

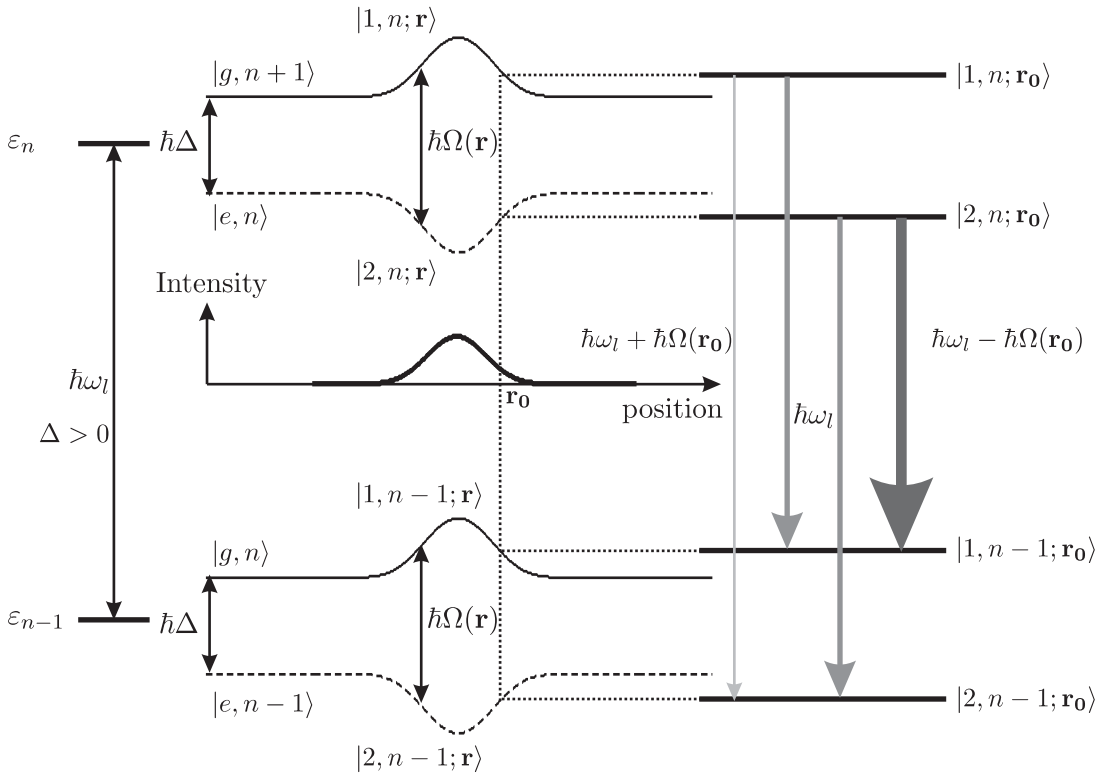

Figure 2.4: Dressed state eigenenergies of a two-level atom in a blue detuned ($\Delta > 0$) quantized light field with Gaussian intensity profile. The spontaneous emissions between two adjacent manifolds are shown on the right hand side. The arrow thickness indicates the corresponding transition probabilities.

The transition rates against the light field parameter Ω/Δ are depicted in figure 2.5. Spontaneously emitted photons carry the energy difference between participating dressed states, i.e. for $\Delta > 0$ a transition from $|1, n\rangle$ to $|2, n-1\rangle$ the photon energy is $\hbar(\omega_l + \Omega(\mathbf{r_0}))$, whereas the photon energy for a transition from $|2, n\rangle$ to $|1, n-1\rangle$ is $\hbar(\omega_l - \Omega(\mathbf{r_0}))$ and for spontaneous emissions without a change of state the photon energies are $\hbar\omega_l$. Therefore, the emission spectrum of an atom in a light field consists of three lines known as Mollow triplet (Mollow, 1969).

2.2.3 Magnetic Substructure

As a matter of fact, the atomic chromium transition ${}^7S_3 \rightarrow {}^7P_4$ used in the experiment is not a two-level transition. The state of an atom with quantum number of the total angular momentum J subdivides into $2J + 1$ Zeeman sublevels. Thus, the treated chromium ground state consists of seven and the excited state of nine Zeeman substates. In the absence of a magnetic field, these substates are degenerate. One can now extend the dressed state formalism used for the two-level atom to the more general situation of a real multi-level system. The internal atomic state describing an atomic transition

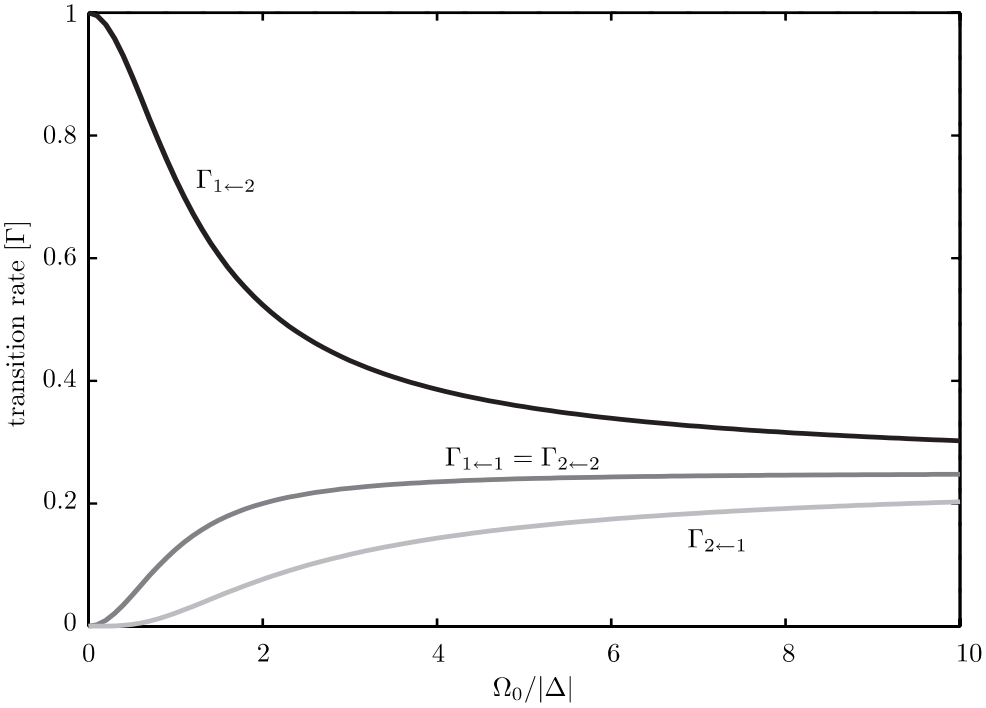

Figure 2.5: Spontaneous emission rates between dressed states in dependence on the ratio between Rabi frequency Ω and laser detuning Δ.

$J_g \rightarrow J_e$ is given by the following Hamilton operator

$$\hat{H}_{\text{atom}} = \frac{\hbar\omega_0}{2}\left(\sum_{m_e=-J_e}^{J_e} |m_e\rangle\langle m_e| - \sum_{m_g=-J_g}^{J_g} |m_g\rangle\langle m_g|\right), \tag{2.23}$$

where $m_{g,e}$ are the magnetic quantum numbers of the participating substates. The coupling strength between atom and light field depends on the polarization of the light field. Because of the selection rule for optical transitions $m_g + m_{\text{photon}} = m_e$, only those transitions depicted in figure 2.6 are allowed. The coupling strength of a particular pair of magnetic sublevels to a light field is given by the Clebsch-Gordan coefficients $C(m_g, m_e)$. The squared magnitudes for allowed transitions are given near the transition arrows in figure 2.6. The problem of an atom with Zeeman substructure in light fields with arbitrary polarization is discussed in detail in (Brezger, 1999). In this dissertation, even external magnetic fields are considered. When the light field is not purely linearly or circularly polarized, more than two levels can couple with the light field. This is important for the theoretical description of polarization gradient light masks where optical potentials with minima spacings smaller than $\frac{\lambda}{2}$ can be realized (Gupta *et al.*, 1996; Brezger *et al.*, 1999).

The scope of this work is confined to linear polarized light fields, which greatly simplifies the further description. The chromium multi-level system decouples into several two-level systems and noncoupling levels. In a light-field, the dressed state eigenenergies of a pair of magnetic sublevels are modified by the associated Clebsch-Gordan coefficient

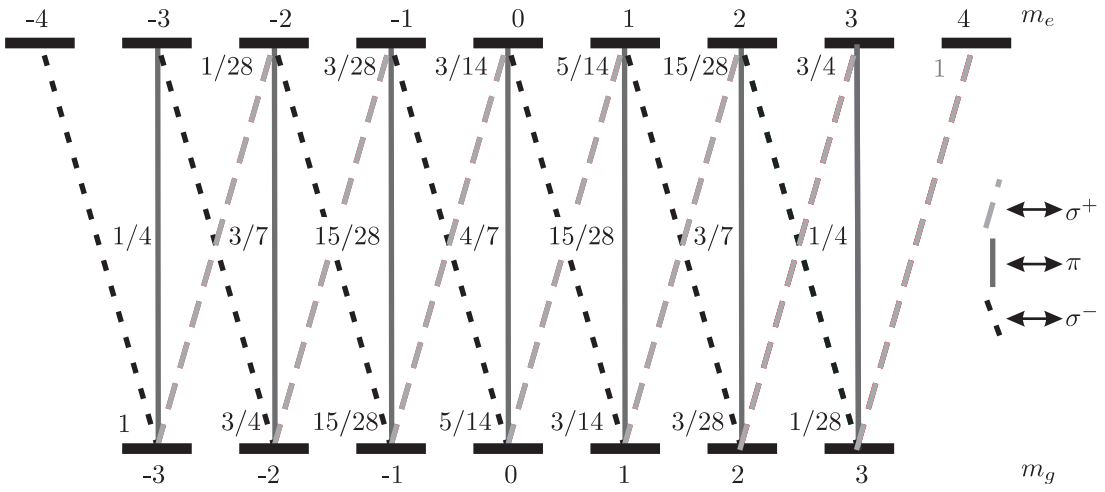

Figure 2.6: Zeeman sublevels and allowed transitions for a $J_g = 3 \rightarrow J_e = 4$ transition. The squares of the Clebsch-Gordan coefficients for the corresponding polarization indicate the coupling strengths of the plotted transition.

such that

$$E_1 = \frac{\hbar}{2}\mathrm{sgn}(\Delta)\sqrt{\Delta^2 + C^2(m_g, m_e)\Omega^2} \tag{2.24}$$

$$E_2 = -\frac{\hbar}{2}\mathrm{sgn}(\Delta)\sqrt{\Delta^2 + C^2(m_g, m_e)\Omega^2}. \tag{2.25}$$

Effectively, the magnetic substructure leads to a reduced coupling strength of the atom with the light field represented by the Rabi frequency $\Omega' = C(m_g, m_e)\Omega$. When the atomic ensemble used in an experiment is not prepared in a single magnetic substate, these differing interaction strengths will therefore lead to state dependent forces on the atom.

2.2.4 Light Forces

Up to this point, the atomic motion itself was not considered. But this is only appropriate in the case of slowly varying light intensity variations and the resulting semiclassical picture is useful to describe the atomic motion in conservative light potentials. Furthermore, it provides a good qualitative understanding of the induced dipole force. However, a more general description has to consider the effect of atomic motion on the light forces as well as spontaneous emissions.

In deriving the dressed states, the atomic motion in a light field was neglected. As a matter of fact, it leads to a nontrivial coupling between the internal and external degrees of freedom of the atom. Thus, the dressed state can be changed either due to spontaneous emissions or motionally induced nonadiabatic transitions. These nonadiabatic processes may occur especially when an atom experiences a rapid change of the dressed levels, i.e. in fields with large gradients, and small energy gaps.

The coupling between the internal and external degrees of freedom is best described in the formalism of density-matrix equations, called optical Bloch equations. For a two-level atom, the density operator ρ given by $\rho = |\Psi\rangle\langle\Psi|$ can be written in terms of a

2×2 density matrix. The wave function describing the atomic state can be expanded into an orthogonal basis set $\{\phi_n\}$

$$\Psi = \sum_{n=1}^{2} c_n \phi_n, \tag{2.26}$$

so that the density matrix elements are

$$\rho_{ij} = \langle \phi_i | \rho | \phi_j \rangle = \langle \phi_i | \Psi \rangle \langle \Psi | \phi_j \rangle = c_i c_j^*. \tag{2.27}$$

The density matrix provides full information about the total wave function such as amplitudes and relative phases. Starting from the dressed states given in equation 2.18 and neglecting spontaneous emissions, one obtains for the temporal evolution of the density operator in the dressed-state basis (equation (2.18)) for an atom moving with velocity $\mathbf{v} = \frac{\mathrm{d}\mathbf{r}}{\mathrm{d}t}$ (Dalibard and Cohen-Tannoudji, 1985)

$$\begin{aligned} \frac{\mathrm{d}\rho_{11}}{\mathrm{d}t} &= 2\mathbf{v}\nabla\theta(\mathbf{r})\mathrm{Re}(\rho_{12}) - \frac{i}{2}\mathbf{v}\nabla\varphi(\mathbf{r})\sin 2\theta(\mathbf{r})\mathrm{Im}(\rho_{12}) \\ \frac{\mathrm{d}\rho_{12}}{\mathrm{d}t} &= -i(\Omega(\mathbf{r}) + \mathbf{v}\nabla\varphi(\mathbf{r})\cos 2\theta(\mathbf{r}))\rho_{12} \\ &\quad +(\mathbf{v}\nabla\theta(\mathbf{r}) + \frac{i}{2}\mathbf{v}\nabla\varphi(\mathbf{r})\sin 2\theta(\mathbf{r}))(1 - 2\rho_{11}), \end{aligned} \tag{2.28}$$

where

$$\nabla\theta(\mathbf{r}) = -\frac{\Delta}{2\Omega(\mathbf{r})\sqrt{\Omega^2(\mathbf{r}) - \Delta^2}} \cdot \nabla\Omega(\mathbf{r}). \tag{2.29}$$

Here, $\rho_{ij} = \langle i, n|\rho|j, n\rangle$, with $(i, j = 1, 2)$, $\rho_{11} + \rho_{22} = 1$ and $\rho_{12} = \rho_{21}^*$.

The atomic motion itself is still treated classically according to Newton's equation of motion $m\dot{\mathbf{v}} = \mathbf{f}(\mathbf{r})$, where $\mathbf{f}(\mathbf{r})$ is the force averaged over both, field and internal atomic states. The force operator $\hat{\mathbf{F}}$ is given by the time derivative of the atomic momentum $\hat{\mathbf{p}}$

$$\hat{\mathbf{F}} = \frac{\mathrm{d}\hat{\mathbf{p}}}{\mathrm{d}t} = \frac{i}{\hbar}\left[\tilde{H}, \hat{\mathbf{p}}\right] = -\nabla\tilde{H}. \tag{2.30}$$

The averaged force in terms of the density operator is given by

$$\mathbf{f}(\mathbf{r}) = \langle\hat{\mathbf{F}}\rangle = \langle\Psi| - \nabla\tilde{H}|\Psi\rangle\langle\Psi|\Psi\rangle = \langle\Psi| - \nabla\tilde{H}\rho|\Psi\rangle, \tag{2.31}$$

and in the $|g\rangle, |e\rangle$-basis the averaged force is

$$\begin{aligned} \mathbf{f}(\mathbf{r}) &= \sum_{i,j=g,e} \langle i| - \nabla\tilde{H}\rho|j\rangle \\ &= -\frac{\hbar}{2}\nabla\Omega\left(\rho_{eg}\mathrm{e}^{-\mathrm{i}\varphi(\mathbf{r})} + \rho_{ge}\mathrm{e}^{\mathrm{i}\varphi(\mathbf{r})}\right) \\ &\quad +i\frac{\hbar}{2}\nabla\varphi(\mathbf{r})\Omega\left(\rho_{eg}\mathrm{e}^{-\mathrm{i}\varphi(\mathbf{r})} - \rho_{ge}\mathrm{e}^{\mathrm{i}\varphi(\mathbf{r})}\right). \end{aligned} \tag{2.32}$$

It is convenient to split this expression for force on the atom into two parts. The first part, proportional to the gradient of the Rabi frequency, is identified with the dipole force. Whereas the second part, called radiation pressure term, is proportional to the

phase gradient of the electric field. Both parts contributing to the mean force can be also expressed in the basis of dressed states: Here, the dipole force reads (Dalibard and Cohen-Tannoudji, 1985)

$$\mathbf{f}_{\mathrm{dip}}(\mathbf{r}) = \frac{\hbar\nabla\Omega(\mathbf{r})}{2}(1-2\rho_{11}) - 2\hbar\Omega(\mathbf{r})\mathrm{Re}(\rho_{12})\nabla\theta(\mathbf{r}). \tag{2.33}$$

and the radiation pressure force is

$$\mathbf{f}_{\mathrm{rpf}}(\mathbf{r}) = \frac{\hbar\Omega}{2} i\nabla\varphi(\mathbf{r}) \cdot 2\mathrm{Im}(\rho_{12}). \tag{2.34}$$

Although the basis was changed, the radiation pressure force is still proportional to the gradient of the phase of the light field, whereas the dipole force is proportional to the intensity gradient. Very often, the light fields under consideration have no spatial phase dependence such that the force on the atom is purely proportional to the intensity gradient. But in typical laser cooling problems, the light fields used are constant in intensity. In those problems, the cooling force exerted on the atoms arises from the phase gradient of the travelling wave components.

In addition, to complete the density-matrix description of atom-light interaction, one has to consider spontaneous emissions between different dressed states and incorporate it into the density-matrix formalism and, again, one has to calculate the associated transition rates. In section 2.2.2 these rates were already determined for transitions from one 'pure' dressed state to another in a lower manifold. But since the atom is in general in a superposition of both dressed states, the transition rates are modified. The atomic superposition state was given in equation 2.26. Starting from that, the corresponding spontaneous emission rates to any 'pure' dressed state $|1, n-1\rangle$ or $|2, n-1\rangle$, respectively, can be determined from the following relations (Chen *et al.*, 1993)

$$\begin{aligned}
\gamma_1 &\propto |\langle 1, n-1|\hat{\mathbf{d}}|\Psi\rangle|^2 \\
&= \Gamma \sin^2\theta \cdot (\rho_{11}\cos^2\theta + \rho_{22}\sin^2\theta - 2\mathrm{Re}(\rho_{12})\sin\theta\cos\theta) \qquad (2.35)\\
\gamma_2 &\propto |\langle 2, n-1|\hat{\mathbf{d}}|\Psi\rangle|^2 \\
&= \Gamma \cos^2\theta \cdot (\rho_{11}\cos^2\theta + \rho_{22}\sin^2\theta - 2\mathrm{Re}(\rho_{12})\sin\theta\cos\theta). \qquad (2.36)
\end{aligned}$$

In comparison to the spontaneous emission rates between 'pure' dressed states, the transition rates for an atom in a superposition are modified by the off-diagonal density matrix elements ρ_{ij}.

The dressed state description of atomic motion presented here is a useful tool that can also be implemented in numerical simulations of atomic nanofabrication. It is especially advantageous over the simplified potential pictures, since it also considers any nonconservative forces that may arise from nonadiabatic effects. Furthermore, it gives an accurate description of the involved spontaneous emissions and is applicable for a much wider range of experimental parameters.

Momentum Diffusion due to Spontaneous Emissions

As outlined in the preceding section, spontaneous emissions can be explicitly considered in the description of atomic motion. Especially Monte-Carlo simulations are a powerful numerical tool and can be implemented for both, semiclassical simulations or quantum

simulations (Dalibard *et al.*, 1992; Lee, 2000; Stützle *et al.*, 2003). However, for the latter case the computational effort can become quite large and a simpler, phenomenological approach is preferred. It utilizes the statistical character of spontaneous emissions that can be applied when a large quantity of atoms is regarded. The random spontaneous emission process then translates to a quantifiable momentum diffusion and subsequently to a broadening effect on the resulting atomic distribution.

In the dressed state picture a spontaneous emission leads to a recoil kick negligibly small for the velocities of our atoms and, much more important, the dressed state may change. In this case the dipole force instantaneously changes its sign. Exactly on resonance, the dipole force is directly proportional to the gradient of the Rabi frequency, i.e. $\mathbf{F_1} \sim -\hbar\nabla\Omega(x)$. Upon a state changing spontaneous emission the instantaneous force acting on the atom changes from $\mathbf{F_1}$ to $\mathbf{F_2} = -\mathbf{F_1}$. This fluctuating force leads to diffusion of the atomic momentum characterized by the diffusion coefficient (Cohen-Tanoudji *et al.*, 1992)

$$D_{\mathrm{dip}} = \int_0^\infty \mathrm{d}\tau \left[\langle F_{\mathrm{dip}}(t) F_{\mathrm{dip}}(t+\tau)\rangle - f_{\mathrm{dip}}^2\right], \tag{2.37}$$

where F_{dip} is the two-valued instantaneous dipole force with mean value f_{dip}. The mean value of the time interval spent in one of the dressed levels is Γ^{-1}. As mentioned above, the mean dipole force is zero exactly on resonance. Therefore, the diffusion coefficient simplifies to

$$D_{\mathrm{dip}} \sim \frac{\hbar^2(\nabla\Omega(x))^2}{\Gamma}. \tag{2.38}$$

Averaging the diffusion coefficient over one standing wave period leads to

$$\langle D_{\mathrm{dip}}\rangle \sim \frac{\hbar^2 k^2 \Omega_0^2}{4\Gamma}. \tag{2.39}$$

The momentum spread due to diffusion is $(\Delta p)^2 = \langle D_{\mathrm{dip}}\rangle \cdot t$. Therefore, the atomic position uncertainty due to momentum diffusion is

$$\Delta x = \int \mathrm{d}t \frac{\Delta p}{m}. \tag{2.40}$$

Rearranging equations 2.39 and 2.40, leads to the following relationship

$$\Delta x = \frac{v_{\mathrm{rec}}}{3} \frac{\Omega_0 t^{3/2}}{\sqrt{\Gamma}}. \tag{2.41}$$

For our experimental conditions, the corresponding position uncertainty can be estimated: the typical atom-light interaction time t_{int} is on the order of $2\Gamma^{-1}$. Equation 2.41 can therefore be rewritten as

$$\Delta x = \frac{2\sqrt{2} v_{\mathrm{rec}} \Omega_0}{3\Gamma^2} \approx \frac{v_{\mathrm{rec}}\Omega_0}{\Gamma^2}. \tag{2.42}$$

With the definition $\Omega_0 = c_\Omega \Gamma$, and introducing a characteristic diffusion length $x_0 = \frac{v_{\mathrm{rec}}}{\Gamma} = 6\text{Å}$, one furthermore obtains

$$\Delta x = c_\Omega \cdot x_0. \tag{2.43}$$

Thus, for a Rabi frequency of 100Γ and zero detuning, spontaneous emission induced momentum diffusion causes a position uncertainty of 60nm.

2.3 Focusing Atoms in Standing Light Waves

Having introduced an adequate description of the atom-light interaction it is now possible to sketch the fundamental scheme of atomic nanofabrication using light forces. For simplicity, the main properties of standing light waves will be presented in an idealized situation, i.e. the atomic beam is assumed to be monochromatic (all atoms have the same longitudinal velocity), perfectly collimated (no transversal velocity) and the atom is a pure two-level system.

The basic idea of atomic nanofabrication is shown in figure 2.7. A collimated beam of atoms with a longitudinal velocity (in z-direction) of around 1000m/s impinges perpendicularly on a standing light wave realized by retroreflecting a laser beam from a dielectric mirror. The periodic intensity distribution of the standing wave light field acts as a periodic lens array for atoms. According to the classical picture of the dipole force (section 2.1), atoms are low field seekers when the laser frequency is tuned above resonance ($\Delta > 0$) and therefore attracted to the intensity minima. For red detuning ($\Delta < 0$), the atoms are attracted to the antinodes of the standing wave. A more precise

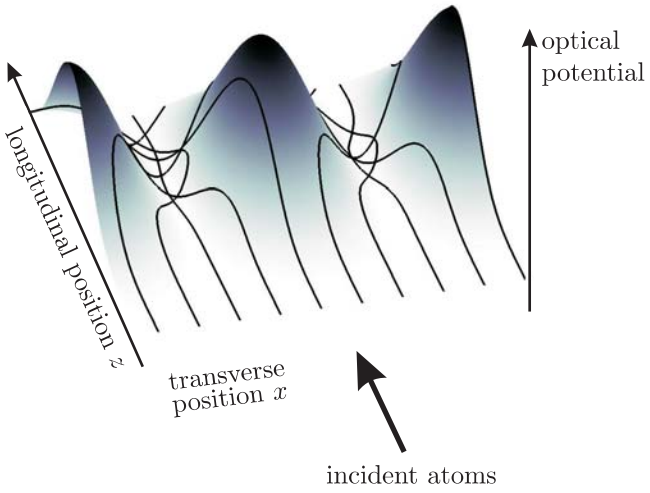

Figure 2.7: Atom lens array made of light: in the red detuned case, the atoms are focused to the antinodes of the standing light wave.

description of the atom optical properties of a standing light wave is derived from the semiclassical dressed state picture. In section 2.2.4 it was shown that the dipole force has both, velocity-dependent and conservative terms. But for a wide range of experimental parameters the velocity-dependent terms can be neglected and a conservative light potential can be found. For this regime, it will soon become apparent that atomic nanofabrication is in very close analogy to geometrical ray optics.

2.3.1 Adiabatic Light Potential

When the velocity-dependent terms of the dipole force are negligible, the light force is equivalent to the classical interaction of the induced dipole with the laser field. The key assumption for this purpose is the so called adiabatic condition: the atom has to move slowly enough in the spatially varying laser field so that the equilibrium between internal

state and radiation field is maintained (McClelland, 1995). In this situation, the kinetic energy term neglected in the derivation of dressed states does not lead to transitions between dressed states of the same manifold and the atom can be treated as a classical particle. Furthermore, this picture ignores spontaneous emissions.

For large detunings ($\Delta \gg \Gamma$) and low intensities, the excited state population of the mainly populated dressed state is small according to equations (2.17) and (2.18). Thus, the atom evolves into only one dressed states ($|1\rangle$-state for $\Delta > 0$ and $|2\rangle$-state for $\Delta < 0$) and remains there throughout the interaction. The dipole force acting on the slowly moving atom in state j stems from the spatial variation of the dressed state eigenenergies E_j given in equation (2.19)

$$\begin{aligned} \mathbf{F}_j(\mathbf{r}) &= -\nabla E_j(\mathbf{r}) \\ &= \frac{\hbar\Omega(\mathbf{r})}{2\Omega_{\text{eff}}(\mathbf{r})}\nabla\Omega(\mathbf{r}). \end{aligned} \tag{2.44}$$

The corresponding eigenenergy E_j is then referred to as dipole potential $U_{\text{dip}}(\mathbf{r})$. In a standing light wave, the intensity distribution is periodically modulated along the direction of incident and reflected wave vector $\Delta\mathbf{k} = \mathbf{k}_{\text{inc}} - \mathbf{k}_{\text{ref}}$. A travelling Gaussian laser beam of power P and waists w_y and w_z has a peak intensity $I_0 = 2\frac{P}{\pi w_y w_z}$. Upon perpendicular incidence on a mirror, the standing wave intensity distribution is given by

$$I(x,y,z) = 4I_0 \sin^2(kx) \exp\left(-2\frac{y^2}{w_y^2} - 2\frac{z^2}{w_z^2}\right). \tag{2.45}$$

The dressed state potentials along the standing wave direction x then read

$$U_{\text{dip}}(x) = \pm\frac{\hbar}{2}\sqrt{4\Omega_0^2 \sin^2(kx) + \Delta^2}, \tag{2.46}$$

where $\Omega_0 = \Gamma\sqrt{\frac{I_0}{2I_s}}$ is the peak Rabi frequency of the incident field. The standing wave potentials are plotted in figure 2.8. Around their local minima they are nearly parabolic[1] when the detuning Δ is much larger than the Rabi frequency Ω_0.

In a blue detuned standing wave, the ground state atoms primarily evolve in the dressed state $|1\rangle$. Hence, they are accelerated to the intensity minima and oscillate around the standing wave nodes with frequency[2] $\Omega_{\text{osc}} = \sqrt{\frac{\omega_{\text{rec}}}{\Delta}}\Omega_0$. When the atomic beam incident on the standing wave is perfectly collimated, i.e. the atoms have no transversal velocity ($v_x = 0$), all atoms cross the potential minimum simultaneously after a quarter of an oscillation time ($\tau = \frac{\pi}{2\Omega_{\text{osc}}}$), no matter at which x-position they enter the light field. Thus, each potential well acts as an atom lens and the periodic standing wave light field with Gaussian envelopes in y and z direction represents a cylindrical lens array.

2.3.2 Pseudopotential

In the experiment, the available laser power is a often a constraint. In order to achieve forces large enough for atomic nanofabrication, it is therefore often required to tune

[1] For Rabi frequencies much larger than the detuning this is only true for the potential of dressed state $|2\rangle$ near the antinode.

[2] The recoil frequency is given by $\omega_{\text{rec}} = \frac{\hbar k^2}{2m}$.

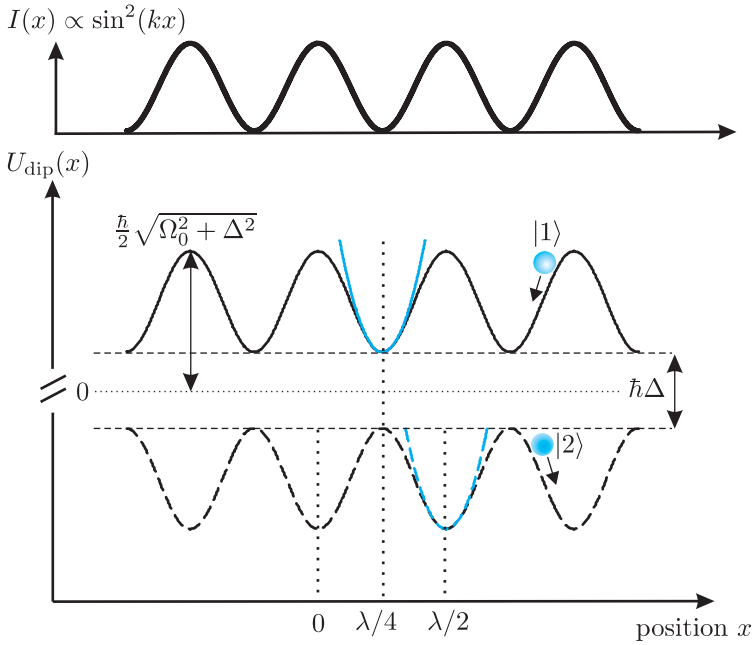

Figure 2.8: The dipole potentials are nearly harmonic around their minima for $\Delta \gg \Omega_0$. The parameters chosen are $\Delta = 50\Gamma$ and $\Omega_0 = 10\Gamma$. For $\Delta > 0$ the mainly populated dressed state $|1\rangle$ is attracted to the standing wave node whereas for $\Delta < 0$ the atom evolves primarily in its dressed state $|2\rangle$ and thus oscillates about the antinode of the standing wave.

the laser so close to the atomic resonance frequency, that the population of the short-living dressed state cannot be ignored. The effect on the dipole force can be considered by utilizing the steady-state populations of the dressed states and weighting the forces on each state with these populations. This results in a steady-state expression for the dipole force that accounts for saturation effects in high intensity fields. Furthermore, a conservative optical potential, sometimes referred to as pseudopotential, can be derived (McClelland, 1995):

$$U_{\mathrm{pp}}(\mathbf{r}) = \frac{\hbar\Delta}{2} \ln\left(1 + \frac{\Omega^2(\mathbf{r})}{2\Delta^2}\right) \tag{2.47}$$

It should be emphasized that this potential picture averages over many spontaneous emissions. Typically, the interaction times in our experiments are on the order of three natural lifetimes and it can be argued that the atomic population approaches its steady state after one lifetime. The discrepancy between using the pseudopotential and explicitly calculating spontaneous events might therefore be small, and most studies conducted to date, that utilized the pseudopotential proved quite successful in explaining the fundamental properties of atomic focusing with this model (McClelland, 1995; Jurdik, 2001). Nevertheless, care must be taken when using this description, especially when the laser field parameters are such that nonadiabatic and spontaneous emission effects become important. In this case one clearly has to revert to the more complex, but more general density-matrix description from section 2.2.4.

Despite these reservations against the simple potential pictures, they clarify the anal-

ogy between atomic focusing in periodic light fields and geometrical ray optics. In light optics, it is either the harmonic shape of refractive lens or the harmonic profile of the refractive index like in a graded-index lens, that focuses the light beam into a focal spot. In contrast, in atom optics, the harmonic shape of the light-induced potential is used to focus the beam of atoms into the same spot. As one can see, the roles played by light and matter are reversed in the latter case: the focusing element for atoms is an immaterial lens made of light. Additionally, one has to keep in mind that the focusing properties of such an atom lens made of light is influenced by the intensity dependence in the direction of propagation of the atoms.

2.3.3 Focusing Regimes

We have seen that due to the parabolic shape of the individual dipole potential wells of a standing light wave, an atom lens array is formed. As in light optics with refractive lenses, one can, dependent on the focal length, distinguish between three focusing regimes:

The standing wave acts as a thin lens array when the atoms are focused far behind the center of the Gaussian envelope standing wave. In this weak focusing regime, the atom lens simply deflects the atoms under a small angle and the harmonic potential shape leads to a flux concentration in the focal plane as shown in figure 2.9(a). The advantage of this thin lens is, that only small laser powers are required and the depth of focus is large. Furthermore, all beam power can be used and the beam does not suffer from beam clipping and diffraction at the substrate edges. The tradeoffs, however, are the difficult substrate alignment and a large focal spot because the achievable focal spot size s is proportional to the focal length f according to

$$s = f \cdot \alpha, \tag{2.48}$$

where α is the divergence angle of the incident atomic beam. In our experiments, α is typically on the order of 0.5mrad and the laser beam waists w are typically around 50μm. The focal spot size for an atomic beam focused $2w$ behind the beam center is then on the order of 100nm. Following this line of argument, shorter focal lengths will lead to smaller focal spots. J.J. McClelland from NIST has studied the focusing of atoms in a standing wave light field with a Gaussian envelope in great detail (McClelland, 1995).

Another case of special interest is the so-called thick lens or immersed focussing regime, i.e. the atoms are focused within the laser field as can be seen in figure 2.9 (b). The focal planes can be found by numerically solving the paraxial equation of motion with the dipole force derived from the pseudopotential given in equation 2.47. For the special (experimentally easily adjustable) case that the focal plane coincides with the center of the gaussian envelope of the standing wave, the following condition for the required laser power is found

$$P_{\text{focus}} = 5.37 \frac{\pi E_0 I_s \Delta}{\hbar \Gamma^2 k^2}, \tag{2.49}$$

where E_0 is the total kinetic energy of the atom in a field-free region. Interestingly, the light power required for focusing to the beam center is independent of the beam waist. Advantages of immersed focusing are the small spot sizes attainable with short focal lengths. Besides that, this method is also favorable from an experimental viewpoint, because it is not too difficult to position the substrate at the beam center.

A third regime for atomic nanofabrication is channeling. Therefore, a much longer standing wave with increasing potential depth in direction of propagation and similar peak intensities as for the previous cases must be used. Initially, the atoms are focused to the potential minima and then, due to the increasing potential depth, they are confined dynamically to the standing wave node (Salomon *et al.*, 1987). When the substrate is placed at the peak intensity position of the Gaussian envelope, optimal localization can be achieved. However, it will be shown later that this scheme depicted in figure 2.9 (c) is only true when spontaneous emissions can be ignored in the localization process. But when the chosen positive detuning is only on the order of few Γ and the intensity is high such that spontaneous emissions preferably occur at the antinodes of the standing wave, the light field can act as a dissipative light mask: the atoms are then simultaneously focused and cooled at the standing wave nodes (Aspect *et al.*, 1986; Chen *et al.*, 1993; Stützle *et al.*, 2003; Petra *et al.*, 2004). From a practical viewpoint, this scheme is the most appealing one, because it combines easy alignment with small attainable nanostructures. However, it requires laser powers that are two orders of magnitude larger than for thick lens focusing.

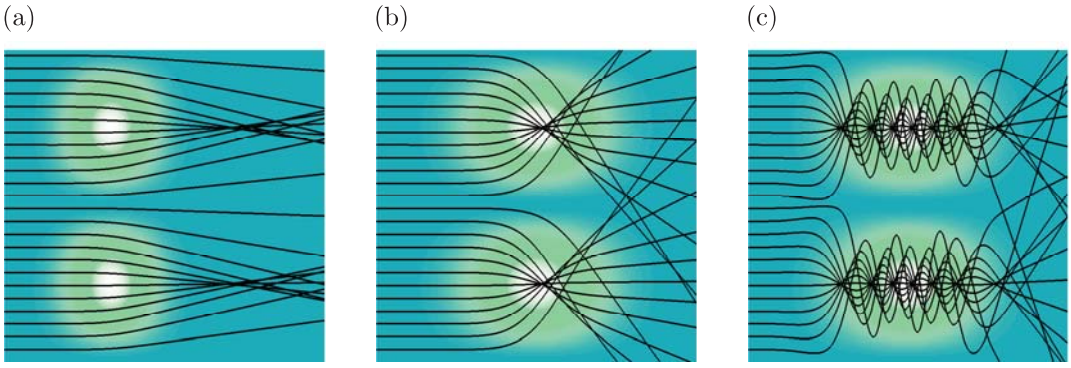

Figure 2.9: Focussing in Gaussian standing wave lenses. (a) thin lens focussing (b) thick lens regime (c) channeling. The background colors reflect the intensity distribution (white corresponds to maximum intensity).

Although the dipole potential picture used here to illustrate the focusing of atoms in a standing light wave somewhat oversimplifies the problem, it gets across the most important parameters and regimes that are experimentally feasible. Furthermore, the presented description based on optical Bloch equations provides an accurate model for simulating real experiments, especially the impact of spontaneous emissions on the formation of the nanostructure background.

2.3.4 Light Forces On Resonance

Using the dressed states description of atom-light interaction it was shown that the mean dipole force can be utilized to determine the classical motion of the atom in a light field. The averaged force given in equation 2.33 is proportional to the gradient of the Rabi frequency weighted by the population difference of both dressed states. In the far detuned case we have seen that primarily one (long-living) dressed state is populated and that the sign of the force, thus, depends on the detuning.

When the laser frequency is, however, tuned exactly on resonance, the situation appears at first glance somewhat ambiguous: In the exactly resonant case the dressed states and their eigenenergies are very simple (Dalibard and Cohen-Tannoudji, 1985) and are given by

$$\begin{aligned} |+;\mathbf{r}\rangle &= \frac{1}{\sqrt{2}}\left(\mathrm{e}^{-i\varphi(\mathbf{r})/2}|g\rangle + \mathrm{e}^{i\varphi(\mathbf{r})/2}|e\rangle\right), \\ |-;\mathbf{r}\rangle &= \frac{1}{\sqrt{2}}\left(\mathrm{e}^{-i\varphi(\mathbf{r})/2}|g\rangle - \mathrm{e}^{i\varphi(\mathbf{r})/2}|e\rangle\right), \\ E_{\pm}(\mathbf{r}) &= \pm\frac{\hbar}{2}|\Omega(\mathbf{r})|, \end{aligned}$$

where the complex Rabi frequency Ω is still defined by equation 2.10. For convenience, here, the notations $|1;\mathbf{r}\rangle$, $|2;\mathbf{r}\rangle$ given in equation 2.18 are replaced by $|+\rangle$ and $|-\rangle$.

An atom entering the light field in its ground state is (and remains) in a fifty-fifty superposition of both dressed states when nonadiabatic effects and spontaneous emissions are disregarded. This becomes also apparent by viewing the optical Bloch equations: the initial values of the diagonal density matrix coefficients (populations) for a ground state atom entering the light field are both $\frac{1}{2}$ and the coherences are zero. On resonance, equations 2.28 therefore decouple because the term $(1-2\rho_{11})$ vanishes and, thus, all density matrix coefficients remain constant. Obviously, the semiclassical particle picture fails because the expression for the dipole force used for determining atomic trajectories (equation 2.33), which is an expectation value for the force, also vanishes[3].

In the dressed state basis, a ground state atom is written as

$$|g\rangle = \frac{\sqrt{2}}{2}\mathrm{e}^{i\varphi(\mathbf{r})/2}\left(|+\rangle + |-\rangle\right). \tag{2.50}$$

Momentarily, the phase factor will be ignored as it can be done for perfect standing waves. The evolution of a ground state atom is governed by the corresponding dressed state potentials E_+ and E_-. Thus, the atomic wave packet will split onto two parts: the $|-\rangle$ is attracted to the intensity maxima while the $|+\rangle$-state is pulled to the intensity minima as indicated in figure 2.10(b). This splitting effect is known as optical Stern Gerlach effect and was proposed by R. J. Cook (Cook, 1987) and has already been observed by looking at the momentum distribution (Sleator *et al.*, 1992). In that experiment, performed in the group of J. Mlynek in Konstanz, the coherent splitting of a metastable Helium atomic beam in the intensity gradient of a long-periodic standing wave was observed.

The situation is sketched in figure 2.10 where the intensity distribution of a standing wave is shown in (a) and the associated dressed state eigenenergies in (b). The solid curve $(-)$ represents a perfectly modulated standing wave (mirror reflectivity $R = 1$) and the dashed line $(--)$ stands for an imperfect standing wave, i.e. $R < 1$. The offset from zero intensity is exaggerated for clarity.

By looking at the dressed state eigenenergies one finds that each individual eigenenergy curve exhibits the same $\frac{\lambda}{2}$ periodicity as the intensity distribution. However, the potential minima for the $|+\rangle$-state are spaced at only $\frac{\lambda}{4}$ with respect to the minima for

[3]The same difficulty arises with the pseudopotential (equation 2.47). On resonance, the potential and the resulting force are zero as it is the case for a classical driven oscillator.

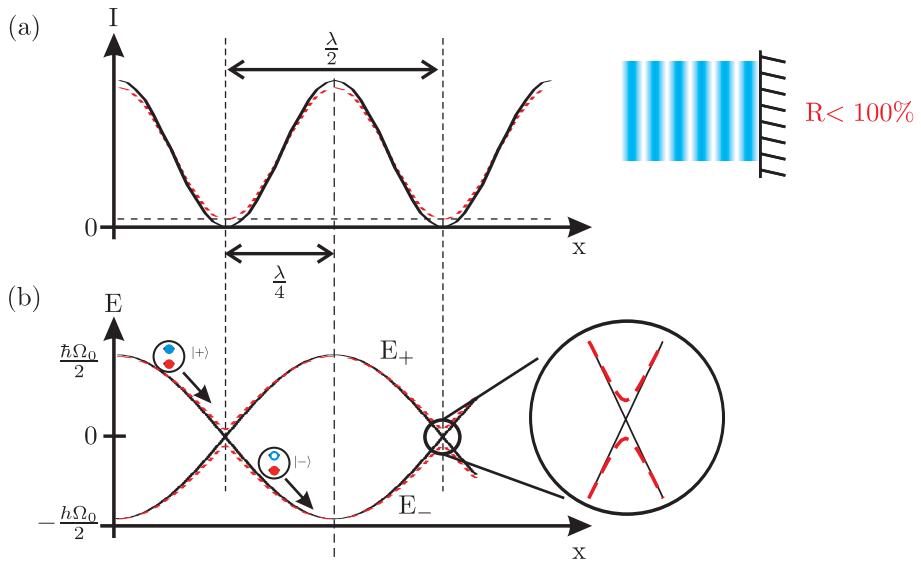

Figure 2.10: (a) Intensity distribution in a standing light wave. The solid curve (−) represents a perfectly modulated standing wave (mirror reflectivity $R = 1$) and the dashed line (−−) stands for an imperfect standing wave, i.e. $R = 0.9$. (b) Dressed state eigenenergies. The zoom emphasizes the energy gap that opens up when the standing wave is not perfect. An atom in the $|+\rangle$ state is attracted to the standing wave node whereas $|-\rangle$ state atoms are pulled to the antinode.

the $|-\rangle$-state. Since on resonance, 50% of all atoms are prepared in each of both dressed states, one expects that during interaction with the standing light wave half of the atoms are attracted to a minima that coincides with the intensity minima and the other half is attracted to the intensity maxima, thus the atomic flux should be modulated with a periodicity of $\frac{\lambda}{4}$. Another interesting aspect provides the different potential shape near the minima. Whereas the $|-\rangle$ potential is harmonic such that nearly ideal focusing can be expected, the $|+\rangle$ potential has a triangular shape and, thus, represents an atom-optical axicon.

2.3.5 Full Quantum Picture

So far, we restricted the description of atom-light interaction to the regime where a semiclassical dressed states formalism is sufficient. However, this model does not take into account the wave nature of the atom. In general, the assumption that the atom behaves like a particle is appropriate, since the de Broglie wavelength of a thermal Cr atom (1000m/s) is only 8pm. However, the transversal velocity in the experiment is typically on the order of few m/s. Therefore, quantum-mechanical effects such as nonadiabaticity and diffraction effects may play a role in atomic nanofabrication (Lee, 2000). In addition, this thesis has a strong emphasis on the problem of exactly resonant standing waves. It will be shown in chapter 4, that in this regime, the atomic motion is governed by both, intensity gradient and phase gradient of a nonperfect standing light wave. It is inherent to the full quantum description that phase effects are incorporated.

Qualitatively, the on-resonant interaction can be well understood in the dressed state

framework: an atom in its ground state is then a fifty-fifty superposition of the two dressed states. In an inhomogeneous light field, both dressed states then propagate independently of one another and experience opposite potentials $\pm\frac{\hbar\Omega(\mathbf{r})}{2}$ as can be seen from figure 2.10. However, this description neglects the phase term of the dressed states which varies dramatically at the nodes of an imperfect standing wave.

Using a fully quantum mechanical treatment of the atomic-light interaction overcomes this limitation because it allows to incorporate also the phase of the light field. In contrast to the semiclassical treatment of atomic motion, now, the motion of an atom is described fully quantum mechanically, i.e. the atom is treated as wave packet. In doing so, one has to solve the complete time-dependent Schrödinger equation including the kinetic part of the Hamilton operator (Efremov *et al.*, 2003) given by

$$i\hbar\frac{\partial\Psi}{\partial t} = \left\{-\frac{\hbar^2}{2m}\nabla^2 + \hat{H}_{at} - \hat{\mathbf{d}}\cdot\mathbf{E}(\mathbf{r},t)\right\}\Psi. \tag{2.51}$$

The wave function for an atom with center-of-mass momentum $\mathbf{p_0}$ can be expanded in its unperturbed ground and excited state wave functions. To simplify matters, the problem is represented as a one dimensional situation. The position vector $\mathbf{r}$ is replaced by the spatial coordinate x such that the wave function reads

$$|\Psi(x,t)\rangle = \sum_{i=g,e}|i\rangle\phi_i(x,t)\exp\left(-\frac{i}{\hbar}(E_i t + p_{0x}\cdot x - \frac{p_0^2 t}{2m})\right). \tag{2.52}$$

Here, $\phi_i(x,t)$ are the wave functions for the internal atomic state $|i\rangle$ and p_{0x} is the component of the momentum along the x-axis. The scheme of matter wave diffraction from a standing light wave is shown in figure 2.11.

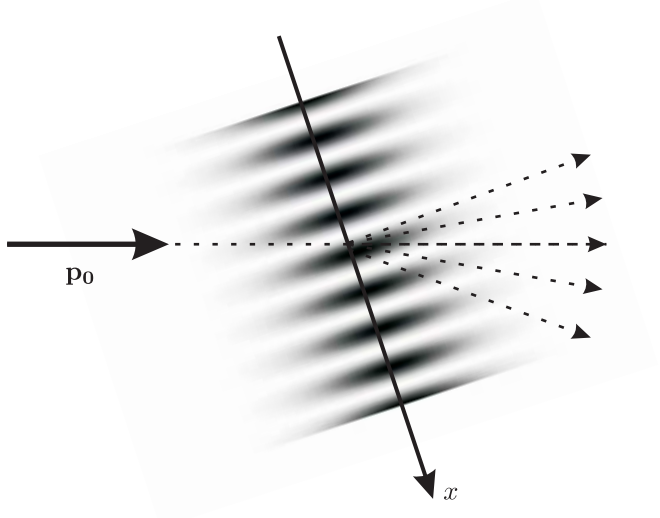

Figure 2.11: Atomic matter wave diffraction from a standing light wave.

Using equation 2.52, the Schrödinger equation can be rewritten as a set of differential equations for the wave functions $\phi_i(x,t)$. By applying the rotating wave approximation

as it was also done in section 2.2.1 one obtains

$$\begin{aligned} \Phi(x,t) &= \begin{pmatrix} \phi_g(x,t) \\ \phi_e(x,t) \end{pmatrix} \\ i\dot{\Phi}(x,t) &= \hat{\mathbf{H}}\Phi(x,t), \end{aligned} \tag{2.53}$$

with the matrix Hamiltonian

$$\hat{\mathbf{H}} = \begin{pmatrix} -\frac{\hbar}{2m}\nabla_x^2 - \frac{ip_{0x}}{m}\nabla_x - \Delta/2 & -\frac{\Omega(x)}{2} \\ -\frac{\Omega^*(x)}{2} & -\frac{\hbar}{2m}\nabla_x^2 - \frac{ip_{0x}}{m}\nabla_x + \Delta/2 \end{pmatrix}. \tag{2.54}$$

Here, $\Omega(x)$ is the complex Rabi frequency, i.e. $\Omega(x) = \Omega_0(x)\mathrm{e}^{i\varphi(x)}$, and $\varphi(x)$ is the phase of the light field.

In standing light waves as used in the experiment, the Rabi frequency $\Omega(x)$ is a spatially periodic function. So far, the standing wave intensity was assumed to be fully modulated, i.e. $I(x) = I_0 \sin^2(kx)$. But such a 'perfect' standing wave is not feasible in an experiment because a mirror is never 'perfect' but has a reflectivity $R = r^2 < 1$. Considering that, the Rabi frequency in direction of the standing wave is given by

$$\begin{aligned} \Omega(x) &= \Omega_i(\mathrm{e}^{ikx} + r\mathrm{e}^{-ikx}) \\ &= \Omega_i(1 + r^2 + 2r\cos 2kx) \cdot \mathrm{e}^{i\varphi(x)}, \end{aligned} \tag{2.55}$$

where the phase is $\varphi(x) = \arctan\left(\frac{1-r}{1+r}\tan kx\right)$ and Ω_i is the Rabi frequency of the incident field. The magnitude of the coupling strength is $\Omega_0(x) = \Omega_i(1+r^2+2r\cos 2kx)$. Evidently, the Rabi frequency is complex only when $r < 1$, whereas for perfect standing waves it is real and has no spatial phase dependence.

The atomic wave function within the light field is also expected to be periodic and can thus be expanded into a Fourier series according to

$$\Phi_{(g,e)}(x,t) = \sum_{n=-\infty}^{\infty} a_n^{(g,e)}(t)\exp(inkx). \tag{2.56}$$

The Fourier coefficient functions $a_n^{(g,e)}(t)$ are the probability amplitudes to find an atom at the levels E_g or E_e in the n-th order diffraction beam with momentum $p_{0x} + nk$. By inserting equations 2.56 and 2.55 into the Schrödinger equation (equation 2.53), one obtains the following set of coupled differential equations

$$\begin{aligned} i\dot{a}_n^{(g)}(t) &= (n^2\omega_{\mathrm{rec}} + n\delta - \frac{\Delta}{2}) \cdot a_n^{(g)}(t) - \frac{\Omega_i}{2}\left(a_{n-1}^{(e)}(t) + r \cdot a_{n+1}^{(e)}(t)\right), \\ i\dot{a}_n^{(e)}(t) &= (n^2\omega_{\mathrm{rec}} + n\delta + \frac{\Delta}{2}) \cdot a_n^{(e)}(t) - \frac{\Omega_i^*}{2}\left(a_{n+1}^{(g)}(t) + r \cdot a_{n-1}^{(g)}(t)\right), \end{aligned} \tag{2.57}$$

where ω_{rec} represents the recoil frequency and $\delta = kv_{0x}$ is the detuning due to an initial transverse velocity v_{0x}. This differential equation system can be solved numerically (see section 2.4.2). To find the atomic probability distribution, an inverse Fourier transform of the resulting momentum distribution into real space must be performed, and finally the magnitude squares of the wave functions for ground and excited state must be added.

As an example, a simulation of quantum mechanical focusing of a collimated atomic beam in a far detuned standing wave is shown in figure 2.12 (a). The plot shows the probability distribution of the atomic wave function in a Gaussian standing wave lens. The focal plane is found 30μm behind the Gaussian beam center. Near the focus, a fringe pattern that originates from matter wave diffraction can be seen. This result is in reasonable agreement with a simulation of 'classical' focusing based on a dressed atom where the focus is about 10μm behind the Gaussian beam center. Here, the 'classical' focal plane is located nearer to the beam center because the dipole force is overestimated.

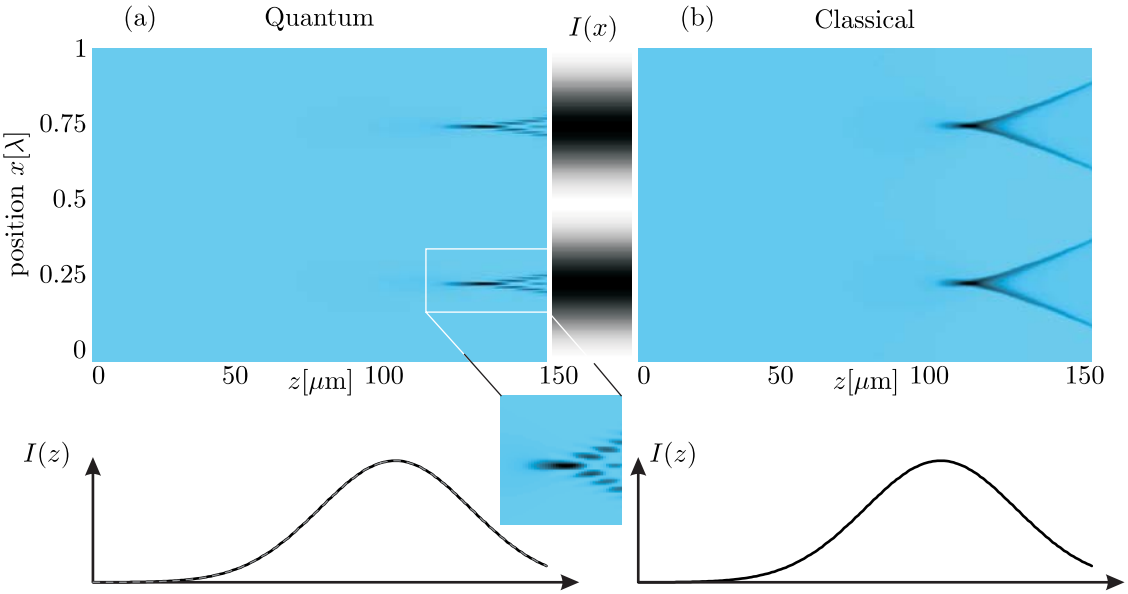

Figure 2.12: (a) Quantum focusing: the plot shows the probability distribution of the atomic wave function during interaction with a standing light wave. The interference fringes shown in the zoom can be attributed to the wave nature of the atoms. (b) 'Classical' focussing of dressed atoms in standing light wave. The parameters for both cases are $\Omega_0 = 100\Gamma$ and $\Delta = +50\Gamma$. A grayscale plot indicates the intensity distribution of the standing wave lens in x-direction and its Gaussian envelope in z-direction is plotted underneath.

This quantum model does unfortunately not include spontaneous emission events. But this simplification is only justifiable when either the laser detuning is large or the Rabi frequency is small, but when the laser is tuned exactly on resonance, these processes cannot be ignored. In these cases a Monte-Carlo wavefunction simulation is more suitable (Dalibard *et al.*, 1992). However, the primary effect of spontaneous emissions on the motion of the atoms is momentum diffusion as discussed in section 2.2.4. But this can be conveniently incorporated in a phenomenological approach. Since spontaneous emission induced dipole force fluctuation lead to broadening of the atomic flux distribution, in the case of the fully quantum mechanical calculations, diffusion leads to a broadening of the resulting probability distributions.

2.4 Numerical Simulations

The theoretical models based on either a particle or wave picture developed in the preceding part of this chapter can be implemented in numerical simulations for comparison with experimental results. For off-resonant light fields a semiclassical Monte-Carlo method based on the density-matrix equations in the dressed state basis derived in section 2.2.4 is used to investigate the atomic flux during and after interaction with the light field.

When the light field frequency is tuned exactly on resonance the density-matrix description cannot be used because the mean force used to calculate atomic trajectories vanishes. Hence, a model based on the full quantum picture described in section 2.3.5 is used.

2.4.1 Density-Matrix Equations

In section 2.3 the principle of atomic focusing in a Gaussian standing wave was explained in terms of the conservative dressed state dipole potential and a pseudopotential that accounts for saturation effects. Although these models are instructive for a qualitative understanding of focusing in standing light waves, several assumptions are not fulfilled in the experiment. First, at large field gradients the atoms are accelerated so fast that nonadiabatic effects may emerge. Furthermore, the interaction times are on the order of only few natural lifetimes, thus, instead of using the pseudopotential that averages over many spontaneous emission cycles, a model is used that reflects the random character of the associated dipole force fluctuations for the detuned case. This dressed-state Monte-Carlo method that accurately describes the atomic motion classically was developed and studied in the group of R. Hulet (Chen *et al.*, 1993) and is also used in this thesis. In the following the implemented Monte Carlo simulation will be presented in detail.

Internal Dynamics and Equation of Motion

Since the dressed states formalism treats atomic motion classically, the differential equation for the external motion and the evolution of the internal states must be solved numerically at the same time. In general, longitudinal and transversal motions are coupled. However, in the present case the longitudinal velocities v_z are three orders of magnitude larger than the transversal velocities v_x and the force that acts on the atom in z direction is negligible and the longitudinal velocities can be assumed as constant. This paraxial approximation allows to write the problem as one dimensional differential equation system. Here, it is convenient to rewrite the optical Bloch equations given in equations 2.28 and the expression for the mean dipole force given in equation 2.31 such that the independent position variable z substitutes the time variable t via $z = v_z t$ and $\mathrm{d}t = \frac{\mathrm{d}z}{v_z}$. This step simplifies the consideration of the longitudinal velocity spread in an atomic beam. Besides that, the experimentally accessible variable is rather the position z than the interaction time t.

Spontaneous Emissions

The decay rates for an atom in a superposition of two dressed states already were determined in section 2.2.4 and are given in equation 2.35. Hence, the total probability for a

spontaneous emission to any dressed state is given by

$$p_s = \Gamma \cdot (\rho_{11} \cos^2\theta + \rho_{22} \sin^2\theta - 2\mathrm{Re}(\rho_{12}) \sin\theta \cos\theta) \cdot \delta t, \tag{2.58}$$

where $\delta t \approx 1$ns is the time step used for the numerical integration method. The branching ratio between a decay from $|\Psi\rangle$ to $|1, n-1\rangle$ and a decay to $|2, n-1\rangle$, respectively is found from equations 2.35

$$\eta = \frac{\sin^2\theta}{\cos^2\theta}. \tag{2.59}$$

Magnetic Substructure

It was already mentioned above that the experimentally utilized chromium transition $^7S_3 \rightarrow {}^7P_4$ is not a two-level transition. In fact the ground state consists of seven magnetic substates. There is little known about the population of different sublevels for chromium atoms after leaving the laser cooling stage. In contrast to the work carried out at the NIST (Anderson *et al.*, 1999) and in Nijmegen (Jurdik, 2001), it is assumed here that the all sublevels are equally populated. Anderson argues that the sublevel population seen in polarization gradient cooling is such that the $m = 0$ and $m = \pm 1$ levels are primarily populated. This follows from a quantum wave function simulation for laser cooling of ^{85}Rb atoms (Marte *et al.*, 1993). However, in our setup the atoms propagate a distance of roughly 1m in a magnetically unshielded region after leaving the laser cooling stage before they impinge onto the standing wave. The impact of stray magnetic fields during this free flight without any interaction with laser light leads to a complete redistribution of the substate populations such that all sublevels are equally populated (Brezger, 1999). The coupling strength of an atom in a ground state sublevel m to the light field is given by the square of the Clebsch-Gordan coefficient $C^2(m_g, m_e)$ displayed in figure 2.6. For a linearly polarized light field as used in the experiments the only allowed transitions are those with $\Delta m = 0$. The associated coupling strengths are $\frac{4}{7}$ for $m = 0$, $\frac{15}{28}$ for $m = \pm 1$, $\frac{3}{7}$ for $m = \pm 2$, and $\frac{1}{4}$ for $m = \pm 3$.

Numerical Integration

The numerical integration of the equations of motion is tackled in the following way: the space of propagation (z-axis) is discretized into a lattice with step sizes at intervals typically 1μm. This corresponds to a time step of 1ns, i.e. significantly shorter than the spontaneous emission lifetime of 30ns. The evolution of the internal and external degrees of freedom of the atom is treated using a Runge-Kutta integration procedure of 4th order for a typical time step of $\delta t \sim 1$ ns. This algorithm is a one-step solver which is important because spontaneous emissions in combination with a rapid change of the internal state may occur at each lattice point. Therefore, the algorithm needs only the solution of the immediately preceding lattice point[4].

In between two spontaneous emission events the density-matrix elements evolve according to equations 2.28, and the atomic motion is given by solving Newtons equation of motion with the instantaneous acceleration given by equation 2.31. After this integration time the spontaneous emission probability for the evolved superposition state $|\Psi\rangle = c_1|1, n\rangle + c_2|2, n\rangle$ is computed.

[4]The programm code is written in MATLAB (The MathWorks Inc.; version 6R12).

For each integration step two pseudorandom numbers homogenously distributed over the interval $[0;1]$ are chosen. The first number is compared to the transition probability p_s given by equation 2.58 and determines whether a spontaneous emission event has occurred. The second random number is compared to η given by equation 2.59 and assigns onto which state the atom is projected as a new initial condition for further propagation. For our parameter set the effect of the recoil kick due to spontaneously emitted photons is small compared to the acceleration resulting from the potential change when the dressed state is altered. Therefore it has been neglected.

2.4.2 Quantum Mechanical Model

For a complete quantum treatment of the atomic motion in standing light waves the time-dependent Schrödinger equation including the kinetic term of the wave function $\Psi(x,z)$ has to be solved.

Coupled Equations for Momenta Probability Amplitudes

In section 2.3.5 it was shown that the periodicity of the laser field can be used to transform the problem into momentum space using a Fourier series expansion. The problem then simplifies to solving the coupled differential equation system in the basis of the bare states $|g\rangle$ and $|e\rangle$ given in equation 2.57.

The probability amplitudes $a_n^{(g,e)}$ of plane waves propagating with transversal wave vector components $n \cdot k$ are coupled to those with one recoil momentum higher or lower. In principle this set of differential equations has to be solved for an infinite number of n what is certainly not possible. Anyway, the computational effort for solving this problem can become very large. An estimate for the maximum n can be given by the maximum velocity a 'classical' atom reaches in the dressed state picture. Typically, they reach a few $\frac{\mathrm{m}}{\mathrm{s}}$ at the potential minima. The recoil velocity is $1.8\frac{\mathrm{cm}}{\mathrm{s}}$, hence up to $N = 300$ momentum states must be taken into account for a sufficiently accurate simulation of the quantum motion based on the coupled wave equations.

Numerical Integration and Spontaneous Emissions

The numerical integration of the evolution of the atomic wave function $\Psi(x,z)$ during interaction with the light field is tackled by solving the differential equation system given in equation 2.57. Therefore, the space of propagation (z-axis) is discretized into a lattice with step sizes at intervals typically 1μm corresponding to a time step of 1ns. The amplitudes of the considered $2N+1$ momentum states (positive and negative momenta) for ground and excites state are assigned to the components of a $4N+2$ vector a, where the first $2N+1$ components contain the ground state amplitudes and the last $2N+1$ those for the excites state. The coupling between adjacent momentum states is represented by a square $4N+2 \times 4N+2$ matrix, where the diagonal and off-diagonal elements can be directly taken from the differential equation system. This matrix differential equation can be again solved by the Runge-Kutta integration procedure of 4th order for a typical time step of $\delta t \sim 1$ns.

One then obtains the real space atomic wave function by performing an inverse Fourier transform. Since our experimental setup only allows us to measure the absolute

atomic distribution, i.e. the amplitude squares of the associated complex wave function, but not its phase, for comparison with the experiment, the calculated wave function must be squared to obtain the atomic probability distribution $|\Psi(x, z)|^2$.

As discussed above, this approach neglects spontaneous emissions. However, it was already shown in section 2.2.4 that the main feature broadening effect of spontaneous emission originates from momentum diffusion. This is phenomenologically incorporated into the simulation results by performing a convolution with a Gaussian function of width Δx according to equation 2.43. A more detailed discussion about this issue will be given in chapter 4.2.2.

3 Experimental Setup

In this chapter, the setup of the atomic nanofabrication experiment will be described. The choice of the element is a key point for implementing the scheme into a real experiment. Therefore, the important properties of chromium will be discussed. Afterwards, the optical part of the system will be presented. The most part of this thesis is dedicated to the work towards nanostructured magnetic nanoalloys, in particular the new ultra high vacuum system that allows to transfer pure chromium structures into the molecular beam epitaxy apparatus in the group of Professor Schatz. In the third part, this new vacuum chamber will be described and finally the sample manipulation and analysis will be briefly discussed.

3.1 Why Chromium?

Our chosen element is chromium because it provides excellent properties for both the manipulation with light forces and the nanostructured deposition onto a substrate.

Especially its low surface mobility and the stability of the deposited chromium film at ambient conditions makes it an ideal material for our experiments (Drodofsky, 1997). These special features allow to study the atom-optical properties of near-resonant light fields since the subsequent analysis of the nanostructured chromium film with an atomic force microscope offers an extremely high accuracy and thus our samples act as atom-detectors with nanometer resolution.

Above all chromium is of great technological interest with wide spread applications. It is a standard coating material in thin film technology and is used as mask material in photolithography because of its high optical density. This property was also utilized by E. Jurdik from University of Nijmegen to fabricate an optical grating with 44μm periodicity by beating two chromium resonances at slightly different wavelengths (Jurdik *et al.*, 2002).

Another fascinating perspective is the possibility to utilize chromium for the realization of nanostructured magnetic nanoalloys. The chromium-platinum materials system is an ideal candidate for this purpose and pursued in this thesis. More details are found in section 4.3.

Besides these perspectives for applications a fundamental requirement for the realization of such experiments is that chromium atoms have an appropriate level scheme for laser cooling and focusing. The main isotope of chromium is ^{52}Cr with a natural fraction of 84%. The relevant part of its level scheme is depicted in figure 3.1.

The ground state $^7S_3$ with quantum numbers $S = 3$, $L = 0$ and $I = 0$, has neither fine

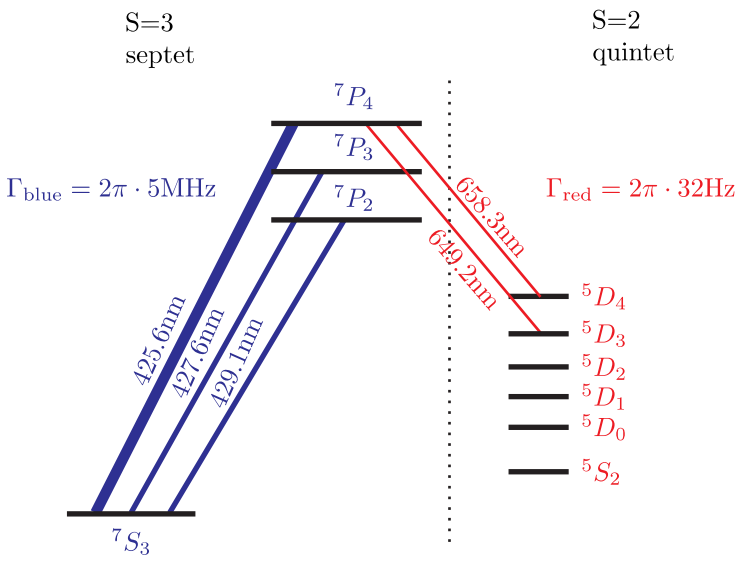

Figure 3.1: Level scheme of ^{52}Cr. The $^7S_3 \rightarrow {}^7P_4$ transition utilized for both laser cooling and focusing is nearly closed. Decays to metastable D-states become important when the interaction times are in the range of milliseconds.

structure nor hyper fine structure. The three dipole transitions indicated in figure 3.1 can be utilized for our experiment. They are all in the visible blue range of the spectrum. It was shown experimentally that each of them is suitable for laser cooling (Drewsen *et al.*, 1996). However, the $^7S_3 \rightarrow {}^7P_4$ transition is advantageous over the other transitions because one can simultaneously apply Doppler cooling and polarization gradient cooling and thus achieve larger atomic flux enhancements.

In the graph one can see that this transitions is not completely closed but has a small probability for decays to metastable states with quantum number $S = 2$. The branching ratio between both transitions is 1:150000, thus, only for long interaction times such as in atom traps the loss channel to the D-state must be closed by means of repumper lasers as used in the chromium MOT experiments in the group of T. Pfau (Stuhler, 2001). For interaction times on the order of tens of μs as in our laser cooling stage, only very few atoms are lost.

3.2 Laser System

The crucial issue of atomic nanofabrication utilizing light forces is the availability of a sufficient amount of laser power at the required wavelength at 425.555nm in the deep blue wavelength range. Since few years laser diodes in this wavelength range are commercially available. They are based on gallium nitride (GaN) technology and will be used for the next generation DVD players. However, the output power of these devices is still limited to approximately 60mW and thus not yet attractive for our experiment since here higher laser powers are required[1]. Besides that, the commercially GaN laser diodes are fabricated to emit in the wavelength range between 400 and 415nm and not at our

[1]These values stem from the Nichia website: `http://www.nichia.co.jp/product/laser-main.html`

required wavelength.

Another important requirement for the laser system is tunability with high accuracy around the resonance frequency of chromium because the dipole force used for focusing atoms is resonantly enhanced near an atomic transition.

3.2.1 Blue Light Generation

Blue laser light at a wavelength of 425.6nm is produced in a multi-stage process as shown in figure 3.2. An argon-ion laser[2] operating in its MLVS (Multi Line Visible) mode at typically 20W acts as pump laser for a single-frequency cw Ti-sapphire ring laser[3] tunable in the near IR range between 750-1000nm. Here, the output laser frequency is adjusted to 851.11nm and monitored by a wavemeter. The output power of the Ti-sapphire laser at an infrared wavelength of 851nm reaches up to 3.2W. This laser light is frequency doubled in an external cavity with a lithium triborate (LBO) crystal that acts as second harmonic medium. This frequency doubler is a redesign developed and setup by R Stützle and described in detail in his diploma thesis (Stützle, 2001). A schematic drawing of the cavity and a photograph are shown in figure 3.3. Here, the innovations and improvements about the former doubler are sketched briefly. In the former model, an anti reflection (AR) coated LBO crystal was used in the external cavity. Because of the large circulating light powers within the cavity, this AR coating was damaged and consequently the conversion efficiency of the doubler dropped. This could be repeatedly compensated by moving the crystal to a position where the coating was yet intact and realigning the optical path in the resonator.

This advantage was overcome by the use of a Brewster-cut LBO crystal. When the pump beam with polarization in the plane of incidence is exactly at the Brewster angle with the crystal surface, all light is transmitted through the crystal. However, such a Brewster-cut crystal introduces an astigmatism into the pump beam which must be compensated with a suitable cavity design. Furthermore, the mechanical stability was improved by a monolithical design. Using a Brewster-cut crystal that acts as a polarizing element, the stabilization scheme of the resonator was now changed from Pound-Drever-Hall to the Hänsch-Couillaud scheme (Hänsch and Couillaud, 1980).

The overall performance of the new frequency doubler was more than convincing. Up to 1.1W blue light power can be generated, i.e. the conversion efficiency is around 30%. In everyday operation, we had around 700mW available, this is twice as much as with the old doubler.

Due to the Brewster cut crystal geometry two side beams are produced from the crystal. They originate from a reflection at the output surface of the crystal because the blue light is s-polarized. Subsequently, this partial beam undergoes double refraction in the crystal before exciting on a polished side surface. These two beams are on the order of 10% of the total power in the main beam and are used for both fluorescence measurements on the chromium atoms and in particular for the spectroscopic frequency stabilization of the Ti-sapphire laser.

The main light beam coming from the frequency doubling cavity is used for the collimation of the atomic beam via laser cooling and the focusing stage realized by a standing light wave as shown in figure 3.2. It is therefore split into two beams that

[2]Coherent Inc., Model Sabre Innova
[3]Coherent Inc., Model 899-21

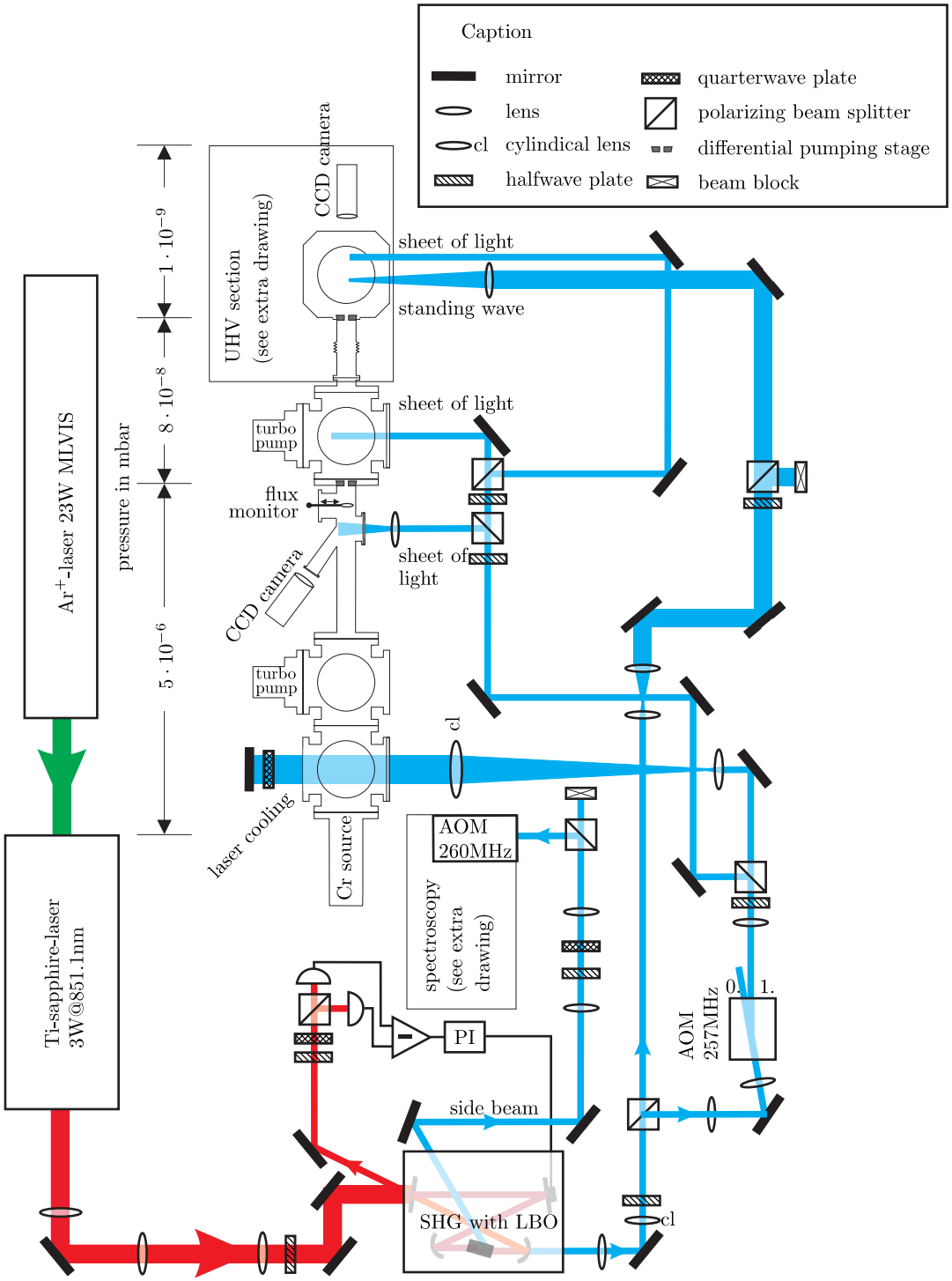

Figure 3.2: Experimental setup. Up to 1W of laser power at 425.6nm are available after the frequency doubler. The main beam is split and frequency shifted such that the laser wavelength is adjusted for both, laser cooling and focusing in the standing wave.

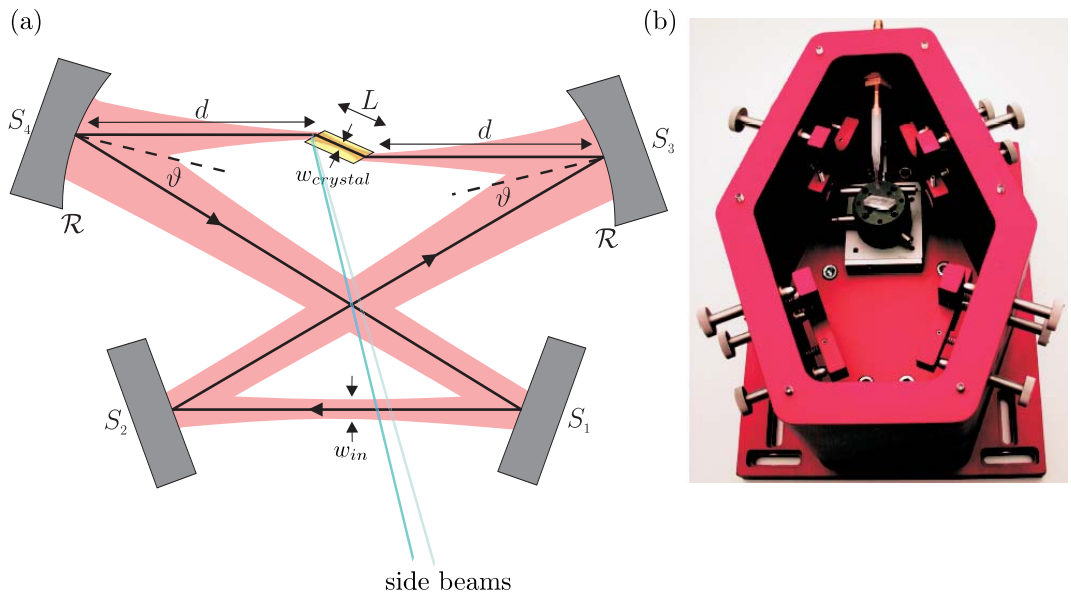

Figure 3.3: (a) Schematics of resonator for second harmonic generation. In its bow-tie configuration it is made of two plane mirrors S_1 and S_2 and two curved mirrors S_3 and S_4 with radius of curvature $\mathcal{R}$. The angle of incidence ϑ onto S_3 can be chosen such that the astigmatism is compensated. The two blue side beams produced upon reflection at the output surface of the LBO crystal are also indicated. (b) Photograph of the frequency doubling cavity.

are frequency shifted using tunable acousto-optic modulators (AOM) that operate at a central frequency of 260MHz. The required detunings for the different experimental stages are $\Delta = -\frac{\Gamma}{2}$ for laser cooling and $\Delta \approx -50\Gamma$ for the standing light wave (in the case of conventional far detuned light masks). These detunings can be accurately adjusted with our spectroscopy lock that stabilizes the frequency of the main beam exactly $\pm$260MHz from the chromium resonance depending on the sign of the detuning for the standing wave. Thus, the laser cooling beam has to be frequency shifted by $\mp$257MHz whereas the standing wave beam has the desired detuning.

3.2.2 Laser Frequency Stabilization

In order to have full control on the light forces acting on the chromium atoms the adjustment of the laser frequency itself is essential for laser cooling and the standing wave light fields. The internal stabilization of the Ti:sapphire laser is very stably on a short-time scale but drifts by several MHz on the time scale of few minutes. These slow drifts must be controlled with a closed-loop. To lock the laser frequency directly to the atomic transition frequency, we utilize polarization spectroscopy (Wieman and Hänsch, 1976). This method is based on a pump probe scheme that produces a Doppler-free spectroscopic signal. For polarization spectroscopy on chromium one first has to produce a vapor of chromium atoms. Because of the high melting point of chromium and its low gas pressure at room temperature, this is easiest achieved by means of an argon gas discharge. At a base pressure of around 1mbar in a hollow cathode cell a gas

discharge at a voltage of 650V and a current of 100mA is initiated (Drodofsky, 1997). The heavy argon ions produced via gas discharge sputter chromium atoms out of the hollow chromium cathode such that a chromium vapor is produced.

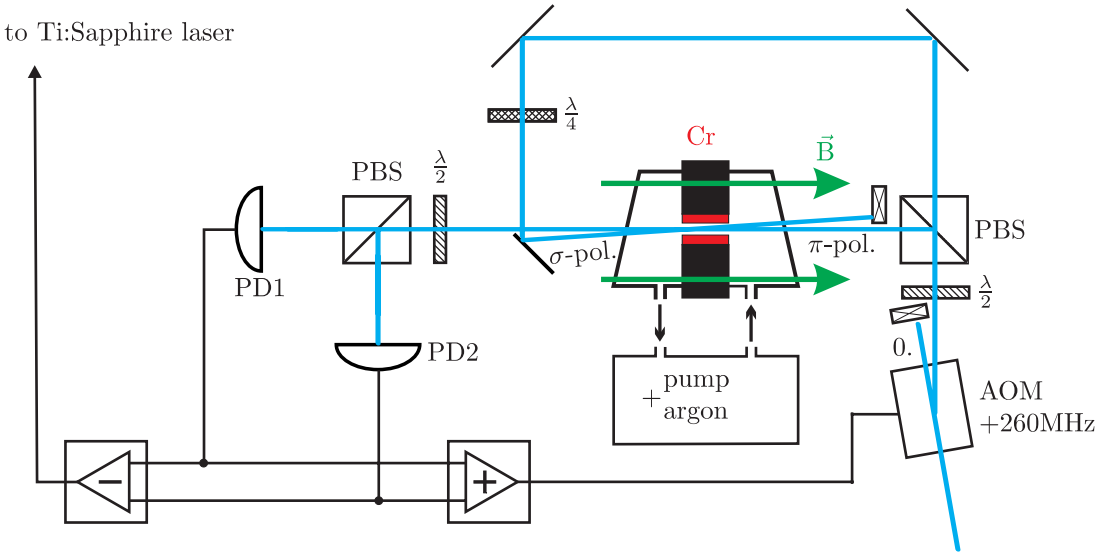

Figure 3.4: Experimental setup of Doppler-free polarization spectroscopy. The AOM shifts the frequency by +260MHZ, i.e. when the laser is locked to the resonance frequency, the light from the frequency doubler is detuned by -260MHz. The magnetic field that is drawn in here is only used for the Doppler-free DAWLL spectroscopy.

The spectroscopy scheme is depicted in figure 3.4. A side beam from the frequency doubler is frequency shifted by exactly +260MHz using an AOM and split with a halfwave plate and a polarizing beam splitter (PBS) into a weak probe and a more intense pump beam. The linear polarized probe beam is directed through the hollow cathode cell whereas the pump beam is passed through a quarterwave plate to achieve circular polarization and directed through the cell from the opposite side. The pump beam optically pumps the chromium atoms which leads to a redistribution of the magnetic substate population. This induces an optical anisotropy in the chromium vapor such that it acts as a birefringent medium (Demtröder, 2003). Pump and probe must be aligned nearly antiparallel through the cell such that they overlap within the hollow cathode cell.

The interaction of the linearly polarized probe beam when it propagates through the birefringent chromium vapor leads to a rotation of the direction of polarization that depends on the sign of the detuning. This rotation of the polarization vector can be detected with a PBS and two photo diodes. In front of the PBS, a halfwave plate is mounted that equals the power of the two beams split by the PBS in the absence of chromium vapor or without pump beam. The two photo diode (PD1/2) signals are electronically subtracted, i.e. without birefringence the difference signal vanishes. When the laser frequency is now scanned over the atomic resonance the detuning dependent polarization rotation leads to a dispersive spectroscopy signal as displayed in figure 3.5(a). Exactly on resonance ($\Delta = 0$) the difference signal is zero because the polarization is not rotated. The Doppler-free polarization spectroscopy signal provides a steep linear zero-crossing that is well appropriate for the frequency stabilization of the Ti:sapphire

laser with a PI controller.

It turns out that the reliability of the spectroscopy is one of most difficult issues of the experiment therefore a more detailed description shall be given here. In the past the signal-to-noise ratio of the spectroscopy signal was improved by lock-in technique but we found that this approach does not remove all difficulties. One important improvement is achieved by controlling the total power incident on PD1 and PD2 with the AOM in the optical path. Here it should be noted that we have observed an obscure rotation of the polarization angle that lead to a changed power ratio between pump and probe beam and a drift of the dispersion signal zero-crossing. We believe that this can be attributed to temperature drifts in the birefringent acousto-optical crystal (tellurium dioxide). A rise in temperature can therefore change the different refractive indices of the crystal and thus rotate the polarization. This can be avoided by ensuring that the direction of polarization of the incident beam coincides with the optical axis of the acousto-optical crystal. Furthermore, it was observed that controlling the rf total power level near its maximum helps to reduce temperature drifts.

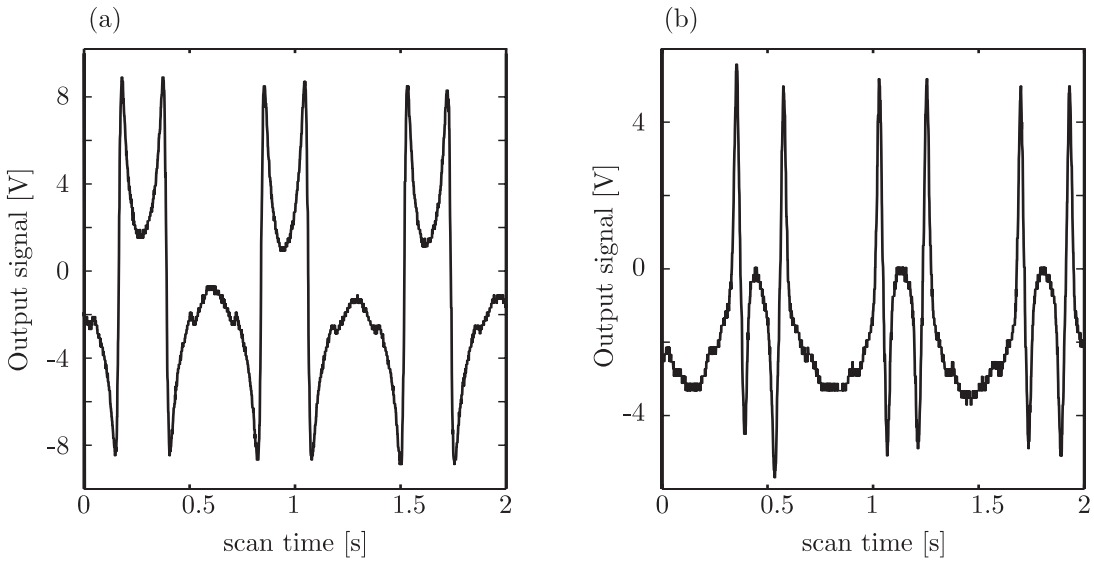

Figure 3.5: Spectroscopy signals for (a) polarization spectroscopy and (b) Doppler-free DAWLL spectroscopy. The widths of the linear range of the dispersive signal amounts to about 10MHz for both methods.

We found the optimal total light power for the spectroscopy to be 15mW with a probe-pump ratio of 1:3. Since the side beam is elliptically polarized, an additional quarterwave plate and a polarizing beam splitter was inserted before the AOM in order to achieve linear polarization. As a matter of fact, the stability of the spectroscopy is directly dependent on the (power) stability of the Ti:sapphire laser. It is therefore recommendable for the future to take the light for spectroscopy out of the main beam from the frequency doubler. Other than the light parameters we found that the attainable signal strength strongly depends on discharge current and argon pressure. Larger discharge currents and thus higher chromium sputter rate require more argon ions, i.e. the argon pressure must be increased but when the pressure is further increased the signal drops again because the discharge is optimal for a certain pressure. We found an optimal

signal strength for an argon pressure of 1.4mbar and a discharge current of 100mA.

In addition to the polarization spectroscopy locking scheme we have also studied a newer spectroscopy approach based on magnetically induced dichroism of atomic vapor called Doppler-free Dichroic Atomic Vapor Laser Lock (DAVLL) (Petelski *et al.*, 2003; Corwin *et al.*, 1998). It combines saturated absorption spectroscopy and DAVLL to produce a Doppler-free dispersive signal that can be utilized for frequency stabilization. It can be understood as follows: when the atomic vapor is exposed to a magnetic field along one of two counterpropagating pump- and probe beams, both circular components of a linearly polarized probe beam (σ^+ and σ^-) are generating a saturated absorption profile, each Zeeman-shifted by the same amount but in different directions. By separately detecting the two components and subtracting their signals from each other, a Doppler-free DAVLL signal is created.

To realize this method we modified the polarization spectroscopy setup from figure 3.4. For an external homogeneous magnetic field a pair of Helmholtz coils was built around the hollow cathode cell. In this scheme, both pump and probe beam are linearly polarized, the quarterwave plate in the optical path of the pump beam is therefore removed. But to detect the σ^+ and σ^- components separately, a quarterwave plate is additionally placed before the PBS in the detection stage. In figure 3.5(b) a Doppler-free DAVLL spectroscopy signal is shown. The magnetic field was around 50G here and the light powers similar as for polarization spectroscopy. The laser was again repeatedly scanned by 200MHz over the chromium resonance by applying a triangular voltage at the external input of the Ti:sapphire laser. From that we deduce that the linear slope of the dispersion signal has a width of around 20MHz which is roughly the same as we get for the polarization spectroscopy signal. We have not yet performed a systematic analysis of this scheme but it appears to be an attractive alternative for polarization spectroscopy because it should be less susceptible to drifts of the zero level.

3.3 Vacuum Chamber

All previous experiments on atomic nanofabrication with chromium were performed in a high vacuum chamber that is described elsewhere (Drodofsky, 1997). The base pressure in this apparatus was typically in the range of 10^{-6}mbar and, thus, sufficient to ensure that the thermal chromium atoms with velocities of around $1000\frac{\mathrm{m}}{\mathrm{s}}$ do not not collide with any background gas atoms. This vacuum pressure certainly allows for fundamental studies of atomic nanofabrication and the experimental results were quite impressive.

Here, it should be noted, that the experimental results on exactly resonant standing waves presented in 4.2 were still made with this 'old' setup. The drawback in this vacuum regime is, that large amounts of impurity atoms from the background gas are incorporated into the grown nanostructures and, since chromium is an excellent getter material, it easily binds oxygen and carbon atoms or compounds. Therefore, only a minor part ($\approx 15\%$) of the fabricated nanostructures consisted of chromium as it was found from a former photo electron spectroscopy analysis of our samples (Mertens, 1999).

However, the major strength of the method is its compatibility with molecular beam epitaxy (MBE) methods. When the vacuum conditions of the apparatus during growth of our nanostructures are better than 10^{-9}mbar, one expects that the chromium structures are at least pure, in a sense that no impurity atoms are present. Finally, such pure

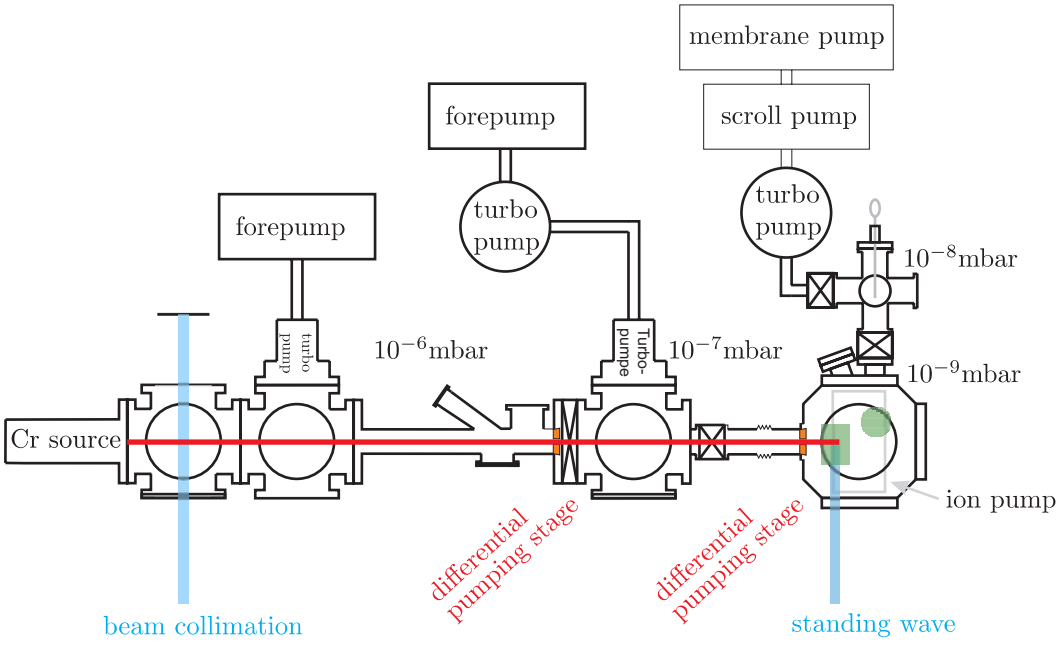

Figure 3.6: Vacuum system. The atomic beam is produced and collimated in a high vacuum stage with a base pressure of 5×10^{-6}mbar. An intermediate (turbo-pumped) high vacuum stage that reaches a base pressure of 8×10^{-8}mbar is required for the final ion-pumped UHV stage at 10^{-9}mbar.

samples represent an excellent base material for the fabrication of novel nanoalloys which was the goal of our work.

3.3.1 Atomic Beam Source

Besides the laser system, the chromium effusion cell is a key part of the experimental setup and has seen numerous stages of development due to continued problems during operation of the source (Drodofsky, 1997; Schulze, 2000). For a sufficient chromium flux ($\frac{\text{nm}}{\text{min}}$), the source temperature must be distinctly above 1600°, which sets high requirements to the utilizable oven materials. In addition, the horizontal orientation of the source poses some technical problems.

The source used at the beginning of this work was a model developed in close cooperation with Mr. Fischer[4]. In that design, the chromium powder was filled into a ceramic crucible made of calcium oxide-stabilized zirconium oxide. This ceramic material proves to be heat resistant up to 2300°. The heating-system is a self-supported tungsten filament and the temperature is monitored and controlled with a thermocouple and PID controller[5].

This design proved quite stable and the source ran for several months without further problems. But after an exchange of the ceramic crucible, another short-circuit repeatedly damaged the heating system of the source, because the new crucible had a tiny invisible crack, such that chromium could diffuse through it. To avoid further accidents

[4] CreaTec GmbH

[5] The history of the source design and a detailed description is found in (Schulze, 2000)

of this kind, we decided to use Createc's standard high temperature effusion cell (model HTC 40-10), but with an outer tungsten crucible and a smaller calcium oxide-stabilized zirconium oxide crucible filled with 99.99% chromium powder that just fits in. The inner crucible had a 1mm diameter exit aperture. The tungsten crucible then acts as a protective cover against the chromium that might evaporate out of the inner ceramic crucible. But to obtain chromium fluxes on the same order of magnitude as with the previous model, the oven temperature (measured with the thermocouple underneath the tungsten crucible) has to be adjusted around 100K higher. i.e. at $1750-1800°$. At these temperatures, the flux rates monitored with a quartz-oscillator mounted 80cm from the source were around $0.2 - 0.3\frac{\mathrm{nm}}{\mathrm{min}}$.

A water-cooled copper heat shield with a central 2mm aperture separates the source part from the remaining vacuum chamber and protects it from radiative heat and chromium vapor that would otherwise quickly cover the vacuum parts.

3.3.2 Laser Cooling

The discussion of atomic focusing in optical standing waves in chapter 2 has shown that the size of attainable nanostructures is primarily limited by the properties of the atomic beam used. Especially the beam divergence must be kept as small as possible analogous to focusing a laser beam with a glass lens. Laser cooling allows to collimate an atomic beam while the flux in the beam center is even enhanced. Thus the deposition times required for the growth of structures with heights of several nanometer reduces to few tens of minutes. We use standard laser cooling techniques on the $^7S_3 \rightarrow {}^7P_4$ transition of ^{52}Cr. Here, one can realize Doppler cooling and polarization gradient cooling simultaneously. Doppler cooling relies on the spontaneous scattering force, whereas polarization gradient cooling utilizes optical pumping between the magnetic substates (Dalibard and Cohen-Tannoudji, 1989; Drewsen *et al.*, 1996). With this scheme, one can in principal reduce the transversal velocity spread down to the recoil limit, i.e. $v_{\mathrm{rec}} = 1.8\frac{\mathrm{cm}}{\mathrm{s}}$. Since the longitudinal velocity is around $1000\frac{\mathrm{m}}{\mathrm{s}}$, one can theoretically reach divergences of few μrad. In practice, one is limited by the finite interaction time of the atomic beam with the laser cooling field, but angular widths on the order of several recoil velocities and well-below the Doppler limit are feasible (Scholten *et al.*, 1997).

The previous atomic nanofabrication experiments in our group had a strong focus on the realization of a plethora of two dimensional nanostructures (Drodofsky *et al.*, 1997a,b; Brezger *et al.*, 1997, 1999; Schulze *et al.*, 1999, 2000, 2001). Hence, the atomic beam had to be collimated in two dimensions. A laser cooling assembly that consisted of a triangular mirror setup in the beam chamber was used. The laser polarization was linear and in the plane of incidence such that a polarization gradient laser field in two dimensions was created (Drodofsky *et al.*, 1997b). Using this scheme, flux enhancements by a factor of seven and transversal velocity widths of $10v_{\mathrm{rec}}$ (Gaussian width) were realized.

The drawback of this setup was its extremely complex alignment procedure and the mechanical unreliability. As the experiments we considered to do were purely one dimensional, we switched back to the much simpler one dimensional laser cooling scheme. Several thorough studies on this issue had already been performed in our group (Drewsen *et al.*, 1996) and at NIST (Scholten *et al.*, 1997).

The laser cooling region, indicated in figure 3.2, is produced by retroreflecting an

elliptically shaped (3cm long, 5mm wide), linearly polarized laser beam from a dielectric mirror. In front of the mirror a quarter-wave plate is mounted such that the polarization of the reflected beam is perpendicular to the incident polarization. This constitutes the lin⊥lin light-field geometry for polarization gradient cooling. Both incident and reflected laser beam have to be orthogonal to the atomic beam but by slightly tilting the beams one can 'steer' the atomic beam through the differential pumping stage apertures and subsequently onto the desired substrate position directly in front of the standing wave mirror.

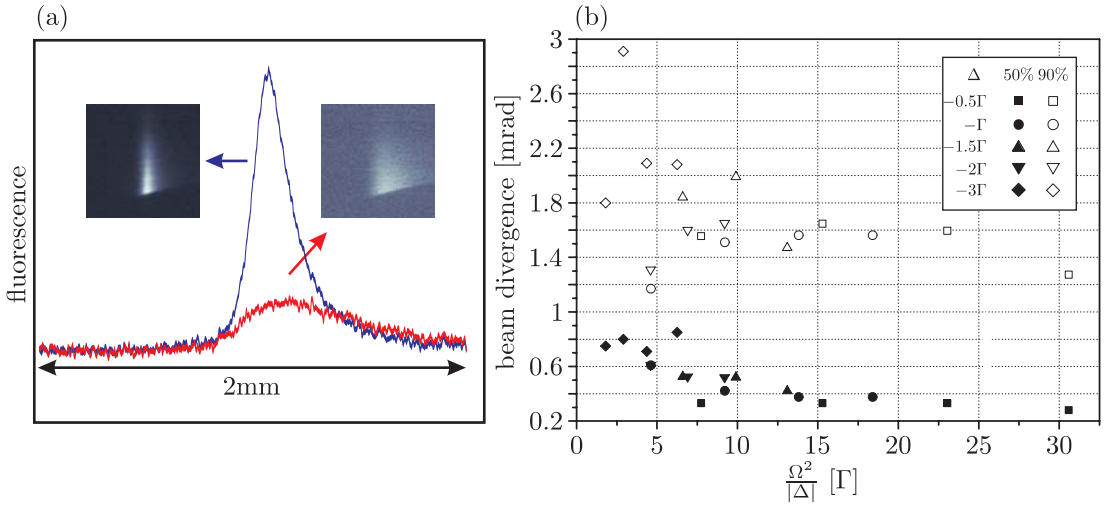

Figure 3.7: (a) Laser induced fluorescence images and cross sections of cooled (left) and uncooled (right) atomic beam 1.2m behind a razor blade. (b) Beam divergences obtained with one dimensional laser cooling in dependence of $\frac{\Omega^2}{|\Delta|}$. The filled symbols represent 50% widths whereas the open symbols show 90% widths.

To find the best collimation parameters we performed a systematic analysis. We varied the light field parameters detuning Δ and Rabi frequency Ω and measured the transversal atomic velocity spread with the razor blade method described in (Scholten *et al.*, 1997). Around 15cm behind the laser cooling stage a razor blade is inserted into the atomic beam such that half of the central part of the beam is blocked. Another 1.2m downstream a sheet of light is shone in perpendicular to the atomic beam[6]. The laser induced fluorescence from the atomic beam at this position is captured with a CCD camera through a viewport. The spatial distribution in these images can be used to deduce the correlated velocity distribution. Fluorescence images of the uncooled and cooled atomic beam and band averaged cross sections are depicted in figure 3.7(a). To determine the beam divergence we utilize the width of the spatial atomic distribution. Taking a longitudinal velocity of $1000\frac{\mathrm{m}}{\mathrm{s}}$ one obtains the associated beam divergence. We see a similar non-Gaussian velocity distribution as the NIST group and follow their line of argumentation of quantifying the degree of collimation. The 50% and 90% quantiles are the divergence angles within which 50% and 90% of the atoms are found. These

[6]This measurement was done in the old high vacuum apparatus with a long flight distance between razor blade and sheet of light. In the new setup, this flight distance was limited to 60cm and allowed to check the laser cooling qualitatively.

quantities are determined by summing the data as a function of angle and assigning the corresponding quantiles. They are displayed in dependence of the light field parameter $\frac{\Omega^2}{|\Delta|}$ in figure 3.7(b). Different laser detunings are indicated by different plotting symbols as can be seen from the inset.

These data reveal the general tendency that small detunings of $-\frac{\Gamma}{2}$ or $-\Gamma$ are favorable because they lead to the smallest 50% and 90% collimation angles. In particular, the optimal 50% width found is 0.3mrad for $\Delta = -\frac{\Gamma}{2}$ whereas the best 90% width is 1.2mrad found for $\Delta = -\Gamma$. These angles are by a factor of two larger than the optimal values achieved by the McClelland group but they provide a sufficient degree of collimation for our experiments such that nanostructures of 50nm or smaller can be fabricated.

3.3.3 Ultra High Vacuum System

The new vacuum chamber with an ultra high vacuum (UHV) deposition stage is shown schematically in figure 3.6. The beam source and collimation part is still a high vacuum stage essentially adapted form the original setup. This chamber also contains the quartz-oscillator for atomic flux measurements, an extricable razor blade, and a view port for a CCD camera to determine the atomic flux and beam collimation from light induced fluorescence measurements.

The second stage acts as an intermediate vacuum chamber with an attainable base pressure of 7×10^{-8}mbar. To abide this pressure difference of two orders of magnitude, we built in a differential pumping stage. It is made of a slightly tapered aluminum cylinder with a little central hole. The maximal outer diameter is chosen equal to the inner diameter of the vacuum tube that connects both high vacuum stages such that the aluminum piece flushes with the tube wall. This ensures that practically all atoms have to pass through the inner hole of the differential pumping stage to get to the neighboring stage. The dimensions of the differential pumping stage have to be chosen so that less atoms can reach the next chamber than can be pumped away by the pump mounted to that chamber. From the pressure relation

$$\frac{p_{\text{low}}}{p_{\text{high}}} = \frac{C}{S_p}, \tag{3.1}$$

where $p_{\text{low,high}}$ are the corresponding chamber pressures, S_p is the pump speed of the vacuum pump, and C is the flow conductivity, one can determine which dimensions of the differential pumping stage are appropriate. For a length $L = 30$mm and a diameter $D = 3$mm, the tube is considered short, i.e. $C = 12.1\frac{D^3}{L+1.33D}$ (Habenicht, 2003). The turbo pump connected to the intermediate chamber has a pumping speed of $240\frac{\text{l}}{\text{s}}$. Thus, the differential pumping stage can abide a pressure ratio of 5.7×10^{-4}, i.e. the attainable base pressure in the intermediate chamber is only limited by its leakage rate.

Both, the beam stage and the intermediate chamber are sealed with rubber gaskets what is sufficient for high vacuum base pressures, however, to realize UHV, a chamber with CF flanges[7] is necessary. Here, bakable copper gaskets with low leak rates are used. To realize a ultra high vacuum better than 10^{-9}mbar in the deposition chamber, a second differential pumping stage between intermediate high vacuum stage and UHV chamber is required. It has the same dimensions as the one described previously, but

[7] ConFlat®, Varian, Inc.

now with an inner diameter of only 2mm. The UHV chamber is pumped with an ion pump[8] with a pump speed of $55\frac{\mathrm{l}}{\mathrm{s}}$. Therefore, a theoretical pressure ratio of 7.8×10^{-4} between these chamber is possible.

This third stage of the vacuum system is the core of the experiment. Here, the focusing light mask made of a standing wave light field is realized and the nanostructures on substrates are fabricated. The UHV requirements set for the production of clean chromium structures lead to several changes in the sample handling and preparation discussed in section 3.3.5.

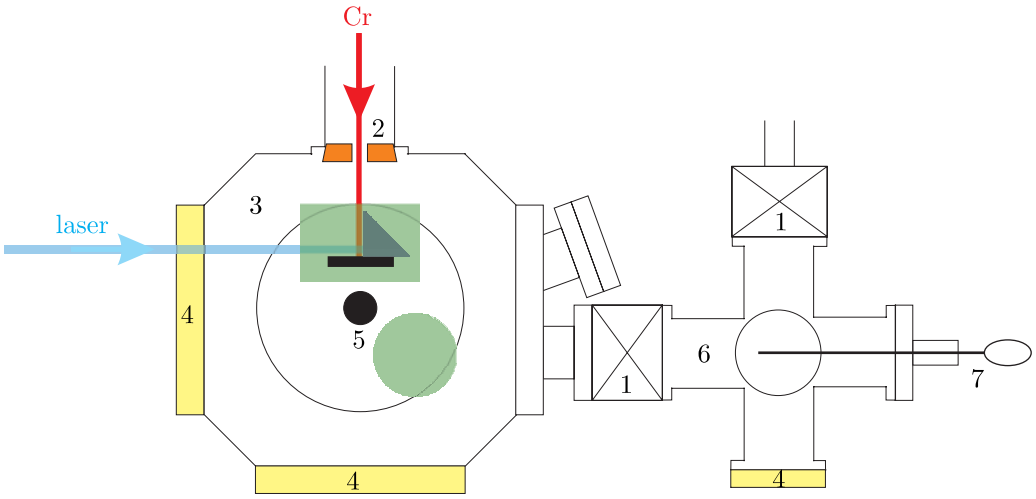

Figure 3.8: Top view of deposition chamber. All vacuum parts have CF flanges. 1 UHV valves, 2 bellow, 3 steel cube, 4 view ports, 5 wobble stick, 6 six way cross, 7 manipulator. The positions of mirror prism and turning foot is indicated within the steel cube.

A sketch of the UHV deposition chamber is depicted in figure 3.8. The chamber itself consists of a DN100 cube (3) made of 316 stainless steel manufactured by the machine shop. The great advantages of this cube over a standard six way cross are that the flanges lie much closer at the inner space of the chamber and its compactness. The cube has six flanges, whereof two are used as view ports (4). One for the standing light wave, and the second for monitoring the atomic flux through differential pumping stage and sample holder. In addition, the He-Ne laser beams used for orienting the mirror prism perpendicular to the atomic beam is incident from this window (more details in section 4.1.3). The ion pump is connected to the bottom flange, whereas the wobble stick (5) used to place the substrate into the sample holder is mounted through the top flange. The chromium beam enters through the differential pumping stage mounted behind a flex bellow[9] from the fifth side of the cube (2). This bellow is crucial for the fine adjustment of the chamber position and orientation. The remaining cube side is used for the sample transfer into another vacuum chamber (6) adjacent to the cube. The samples are transferred by means of a manipulator (7) from the cube into the six way cross; therefore, the UHV valve (1) has to be opened. From here, the samples

[8] VacIon Plus 55 Pump, Varian, Inc.
[9] Caburn-MDC GmbH, as all other UHV parts used, if not stated otherwise.

can be either taken out of the vacuum or transferred into a transfer chamber for further processing in the MBE machine of Professor Schatz's group. One unused flange attached at an angle next to the transfer section is left for purposes like e.g. a pressure gage.

3.3.4 Standing Wave Substrate Assembly

Realization in the High Vacuum System

We have seen in chapter 2 that the lens array for atoms utilized for atomic nanofabrication is realized by standing light waves. In the simplest case, a one-dimensional standing wave is used thus the mask acts as a cylindrical lens array. This scheme was extended in the preceding years to two dimensions using a variety of two dimensional light masks. They were realized by interfering three or four laser beams in more complex mirror setups. To achieve these triangular or square lattice patterns the light masks were realized on so-called deposition plates (Brezger, 1999; Schulze, 2000). Here, the light beam was guided by a single-mode optical fiber into the vacuum chamber where this deposition plate was mounted. The plate itself consisted of an output coupler for the fiber, typically some lenses to produce the desired beam size and a mirror setup of one or two mirrors. Depending on the angle between the mirrors and the angle of incidence of the laser beam different interference patterns could be realized. An advantage of this setup was that the substrates were mounted on this deposition plate directly in front of the mirror and the standing waves could be aligned outside the vacuum chamber. Furthermore, a linear motor was mounted on that plate such that several depositions could be made on one substrate. The crucial alignment of the standing wave perpendicular to the atomic beam was done by a pair of parallel He-Ne laser beams whereof one was aligned parallel to the atomic beam and the second one was directed onto the back surface of the mirror prism. The deposition plate could then be tilted with two stepper motors inside the vacuum chamber until the second He-Ne beam was reflected back in itself.

However, this experimental realization had several drawbacks. First of all, we are concerned about making our nanostructuring scheme compatible with MBE methods. Therefore, the glass fiber technique should be avoided because one expects vacuum problems or leaks. Secondly, the glass fiber limits the available light power. Typically, we could not couple more than 15mW of blue light through the fiber. And thirdly, such a deposition plate setup that is taken in and out of the vacuum chamber every day is not applicable for UHV conditions.

A main reason for such a compact design was its mechanical stability. The apprehension was that vibrations on the nanometer scale could destroy the structures. But this is not a problem as long as we make sure that the substrate does not move with respect to the mirror used for the standing wave.

For compatibility with our new UHV deposition chamber we therefore changed our standing light wave setup to free space propagating laser beams. Initially we made these experiments in the 'old' high vacuum chamber (in particular the on-resonance depositions described in section 4.2). The one dimensional standing wave was realized by focusing our blue laser beam with a spherical lens (focal length f=40cm) from outside the vacuum chamber through a window onto a right-angled $1 \times 1\text{cm}^2$ mirror prism glued on a new steel deposition plate ($16 \times 16\text{cm}^2$) and screwed on the approved vibration isolation unit (Weber, 1995). The advantage of this method was that we were not limited by the

available laser power and, crucial for the background suppression experiments, we were able to position the standing wave with respect to the substrate much more accurately.

It turned out that the mechanical stability or vibrations from vacuum pumps are not a problem because in this setup we tightly pressed the substrate with metal springs against a slide and along the mirror prism. In principal, the nanofabrication worked as well as with the glass fiber setup on the deposition plate.

Ultra High Vacuum System

These positive experiences made us confident for our UHV standing wave setup. Again we had to ensure high mechanical stability of the substrate with respect to the mirror prism. Furthermore, the nanofabrication in UHV sets several additional requirements to the production scheme. A rough schematic overview of the standing wave assembly location within the UHV chamber is indicated in figure 3.8 and a detailed schematic is shown in figure 3.9(a).

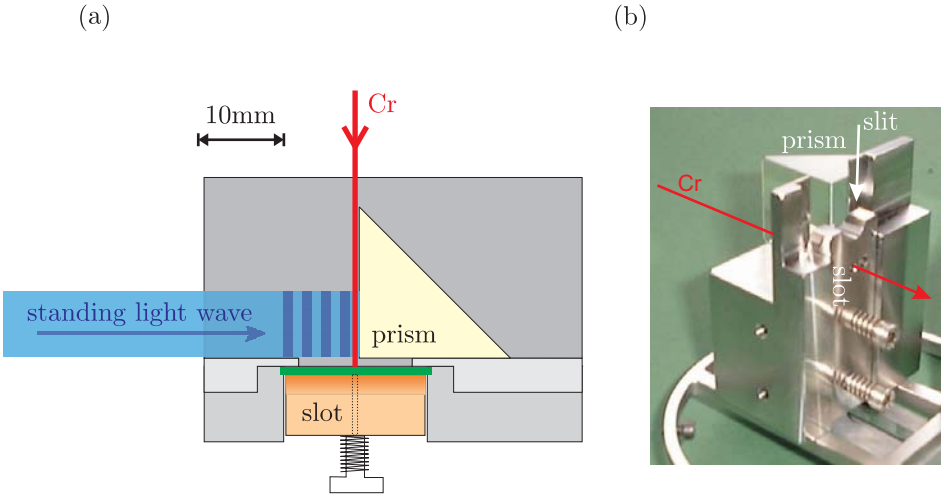

Figure 3.9: Prism holder. (a) Schematic top view: the standing wave perpendicular to the atomic beam is realized by retroreflecting a focused laser beam onto the dielectric mirror surface of a right-angled prism glued on the prism holder made of steel. This massive assembly also contains the slot for the substrate holder. A screw and a spring fix the substrate holder tightly against the prism holder such that the substrate is placed directly in front of the mirror surface without a chance to move. (b) Photograph of assembly. At the bottom part, one can see a ring used to screw the whole assembly against the UHV chamber.

The $25 \times 25\text{mm}^2$ right angled mirror prism is glued with a UHV compatible glue on the prism holder which consists of a ring at the bottom used to screw against the inner walls of deposition chamber. This is a critical and difficult procedure for the height adjustment with respect to the atomic beam. Its height must be chosen such that the chromium beam passes through a hole drilled into the substrate slot that fixes the substrate holder tightly against the prism holder.

For the standing light wave we focus a collimated light beam with a waist of around 1.5mm coming from the frequency doubler with a spherical lens (focal length f=40cm)

onto the dielectric mirror surface. Thus, we achieved beam waists near the mirror of $w_z = 50\mu$m (along the atomic beam axis) and $w_y = 37\mu$m. For an accurate positioning relative to the substrate, the lens is mounted on a controllable translation stage (details are given in section 4.1.3, in particular figure 4.11).

The important angular alignment of the standing wave requires a rotation of the complete deposition chamber but this can be done only for small angles. The rough alignment is already done when the prism holder assembly is mounted. First, two parallel He-Ne laser beams spaced at 5mm are set up (see figure 4.10), Beam 2 is aligned onto the atomic beam axis given by the two differential pumping stages and then tweaked symmetrically onto the aperture behind the effusion cell that defines the beam source. Then the prism holder is built in such that beam 2 passes through the hole in the slot at the substrate height and beam 1 is reflected back in itself from the second cathetus plane perpendicular to the mirror side. Thus, the standing wave will be perpendicular to the atomic beam, at least within few mrad. The final fine alignment must be done experimentally and is described in section 4.1.3.

3.3.5 Sample Manipulation

In the following a brief description of sample preparation and transfer is described to understand the function of the different parts used. Having cleaned the substrates (silicon, germanium, glass or sapphire) thoroughly in acetone and methanol using a ultrasonic bath, they are subsequently dried and carbon dioxide snow cleaned[10]. Afterwards, they are mounted on the substrate holders shown schematically at the bottom of figure 3.10(a).

In the previous section the substrate positioning was already briefly mentioned. From the beginning the presented scheme was outlined for compatibility with the MBE machine in Professor Schatz' group. Therefore, both substrate holders and the transport magazine must be compatible with the utilized high vacuum transfer chamber and the manipulators used in the MBE machine.

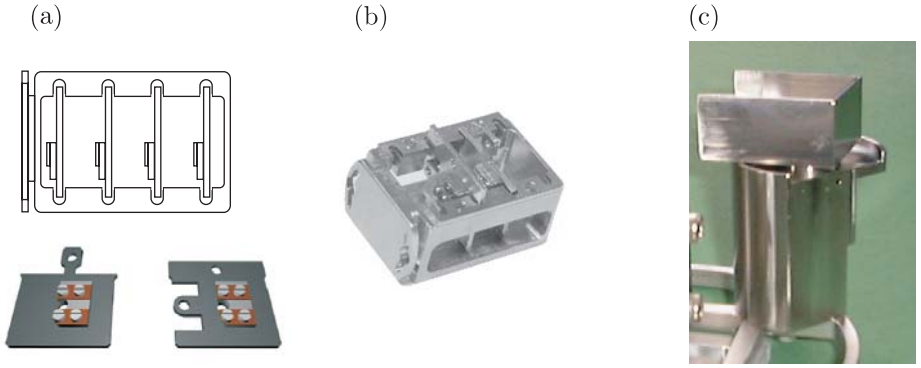

Figure 3.10: (a) Schematics of magazine and substrate holders. The standard holder on the left is made of molybdenum because of it is heat proof whereas the type on the right side is made of steel and used for the transfer to the MBE machine. (b) Photograph of substrates in magazine. (c) Photograph of 'drawer' on turning foot.

[10] Applied Surface Technologies, Snowjet®

They are schematically shown in figure 3.10(a) together with a photograph of two different substrate types in the magazine and a picture of the 'drawer' on the turning foot (c). The substrate holder on the left is used for experiments where the samples are taken out of the vacuum after deposition and analyzed at ambient conditions. The type to the right has two loops used to grasp the substrate holder with a wobble stick. This is necessary when they were transferred to the MBE machine because the AFM built in there can only scan parallel to the substrate edge, i.e. along the chromium lines. Therefore the samples must be turned by 90° in the MBE before an AFM scan. In the center of the substrates two little holes can be seen that are necessary for the alignment laser beam 2 to check the perpendicular alignment of the substrate.

The four screws on top of the substrate holders allow for a coplanar tight alignment such the atomic beam impinges perpendicularly onto the substrate and the substrate edge will not block the standing wave directly before they hit the substrate. Up to four substrates on their holders are then placed in a row in the magazine shown schematically at the top of figure 3.10(a). A photograph of the substrates in place is shown in figure 3.10(b). Usually, we leave the magazine mounted on the manipulator and put in the substrates through the opened top view port of the six way cross shown in figure 3.8. The chamber is afterwards closed and pumped. As soon as the base pressure in this transfer chamber is below 10^{-7}mbar the UHV valve to the deposition chamber is opened and the magazine is transferred with the manipulator into the cube. There it is put down on the 'drawer' shown in figure 3.10(c). The manipulator is turned to unlock the bayonet connector and pulled back into the transfer chamber and the UHV valve is closed again.

After pumping overnight to reach a base pressure of 10^{-9}mbar and checking that the laser-cooled atomic beam passes with maximum flux through differential pumping stages and substrate holder slot, the substrates are built in for deposition. Therefore, one first has to turn the magazine in the 'drawer' on its turning foot (see figure 3.10(c)). Afterwards, a substrate is lifted out of the magazine with a special hook mounted at the tip of a wobble stick on top of the deposition chamber that is threaded through the loop on top of the holder. Then, the substrate is pushed into the slot on the prism holder that finally presses it tightly against the prism and the hook is carefully weaved out of the holder loop.

Having brought the substrate in place the standing wave is positioned and the chromium deposition can start. Afterwards, the sample is taken out of the slot and put back into the magazine and after all depositions were made, the magazine is transferred to the six way cross. From here, it is either taken out of the vacuum for a direct AFM analysis or transferred into the high vacuum transfer chamber. For that purpose, a second manipulator mounted at the bottom of the six way cross is pushed in. This manipulator has the shape of a drawer. The magazine is put down on this drawer and turned by the bottom manipulator. Another magnetic manipulator in the transfer chamber previously flanged to a side of the six way cross then grasps the magazine so that it can be safely pulled into the transfer chamber. From here it can be transferred directly into the MBE machine.

4 Atomic Nanofabrication

In this chapter the results of our atomic nanofabrication experiments are presented and compared to theoretical predictions. Two classes of experiments were performed: the deposition of chromium atoms in off-resonant and exactly resonant light fields. The off-resonant problem can be well understood in the classical picture of the induced dipole force. Our main focus here is on the applicability of the method. It is therefore essential that the background of the produced nanostructures is reduced. For this purpose we performed systematic measurements and it will be shown that our proposed scheme proves successful and agrees very well with theoretical calculations.

The case of on-resonant light fields is a problem of fundamental interest because the classical picture implies that the dipole force on an atom vanishes in this case. But in the quantum picture, where the atom is described as a wave packet, the on-resonant interaction with an inhomogeneous light field leads to a splitting of the atomic wave function in opposite directions and, thus, in a standing wave with $\frac{\lambda}{2}$ periodicity a focusing with $\frac{\lambda}{4}$ periodicity is predicted. Experimentally, we observe that the resulting structure depends on the local intensity such that $\frac{\lambda}{4}$ periodicity is only observed at low intensities whereas at higher intensities the periodicity is only $\frac{\lambda}{2}$. Furthermore, we observe a pronounced asymmetry of the $\frac{\lambda}{4}$ structures which is a signature for the quantum mechanical motion of the atoms. The quantum simulations exhibit excellent agreement with our observations.

4.1 Off-resonant Standing Waves: Systematics

The fundamental requirements to bring atomic nanofabrication closer to application are on the one hand the choice of a technologically interesting atomic species and on the other hand the attainable structure sizes of the nanostructures (width) and the structure background called pedestal as shown schematically in figure 4.1. The achievable structure widths are primarily dependent on the divergence of the atomic beam and the focal length of the standing wave lens as discussed in section 2.3.3. In addition, there is strong evidence that for feature widths smaller than 30nm the growth behavior plays a key role and might prevent further miniaturization (Anderson *et al.*, 1999). The pedestal however originates from lens imperfections: non harmonical deviations in the shape of the potential well lead to spherical abberations of the standing wave lens array. In addition, chromatic aberrations due to the longitudinal velocity spread of the thermal atomic beam become important in the thin lens regime (see figure 2.9(a)), whereas in the thick lens regime the feature broadening is dominated by the beam divergence (Anderson

et al., 1999).

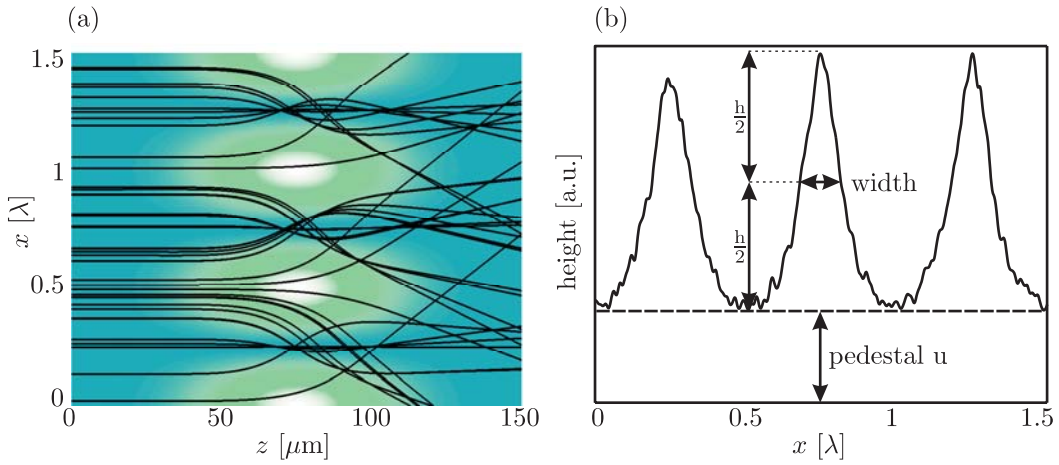

Figure 4.1: (a) Numerically simulated atomic trajectories in a blue detuned standing wave for one longitudinal velocity and vanishing transversal momentum spread $\sigma_t = 0$. The bright regions of the light field denote higher intensities. (b) Flux distribution 20μm behind the standing wave center. The features of the resulting structures are described by the structure width (full width half maximum) and the background also called pedestal.

An improved high contrast (or small pedestal) is desirable for most anticipated applications. Both, the fabrication of photonic crystals based on structured doping (Schulze *et al.*, 2001) and the realization of magnetic nanostructures as it is pursued in this work benefit from progresses in this direction. In the following the differences between red and blue detuned Gaussian standing waves are discussed briefly and strong emphasis is dedicated to the problem how the structure background can be efficiently suppressed. Furthermore, experimental results are presented and compared to numerical simulations.

4.1.1 Initial Conditions for Simulation

For the upcoming discussion of experimental results a series of numerical simulations based on optical Bloch equations described in section 2.4.1 was performed. To ensure a realistic modelling of our experimental conditions, the choice of initial conditions is essential. In analogy to focusing a light beam by an optical lens, the atomic beam parameters such as divergence (transversal velocity spread) and spectral width (longitudinal velocity distribution) determine the attainable resolution of an atom lens.

In our experiment the atomic beam is produced by a thermal source at 1850°C and transversally laser cooled to reduce its divergence. The longitudinal velocity distribution of the uncooled beam was measured earlier (Stuhler, 1996) and found to agree reasonably well with the distribution of an effusive source given by

$$P(v_z)\mathrm{d}v_z \propto v_z^3 \exp\left(-\frac{mv_z^2}{2k_\mathrm{B}T}\right)\mathrm{d}v_z, \tag{4.1}$$

where k_B is the Boltzmann constant and T the source temperature.

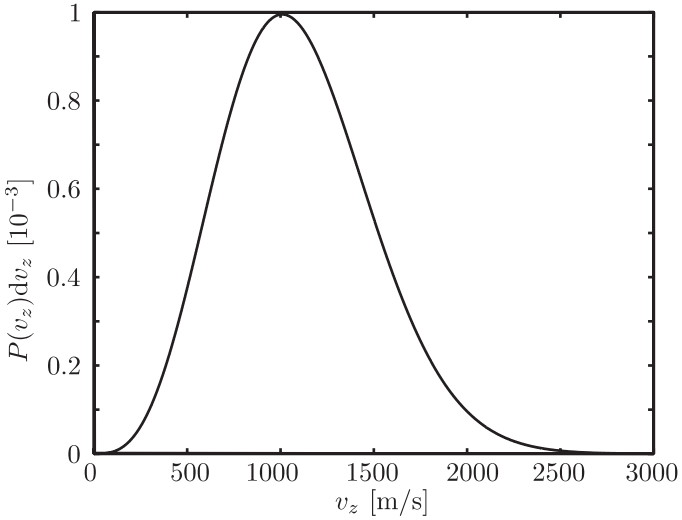

Figure 4.2: Longitudinal velocity distribution of an effusive source at $T = 1850°\mathrm{C}$. $P(v_z)\mathrm{d}v_z$ is the probability for an atom to have a velocity in the range v_z to $v_z \pm 1\frac{\mathrm{m}}{\mathrm{s}}$.

The velocity distribution of an effusive source at the given oven temperature is shown in figure 4.2: the most probable velocity is $1010\frac{\mathrm{m}}{\mathrm{s}}$ and the 50% of all atoms are in the velocity range between 700 and $1300\frac{\mathrm{m}}{\mathrm{s}}$.

The initial transversal velocity distribution is given by the performance of beam collimation via laser cooling. It can be approximately described by a Gaussian normal distribution

$$P(v_t)\mathrm{d}v_t \propto \exp\left(-\frac{v_t^2}{2\sigma_t^2}\right)\mathrm{d}v_t. \tag{4.2}$$

A typical value for the transversal velocity spread reached in the experiment by optimizing the laser cooling[1] is $\sigma_t = 0.3\frac{\mathrm{m}}{\mathrm{s}}$. To account for the effect of an extra tilt of the standing wave of 1mrad the mean value of the initial transversal velocity distribution was $1\frac{\mathrm{m}}{\mathrm{s}}$. The light field parameters (Rabi frequency and detuning) used in the simulations were chosen according to the experimental values.

For each set of parameters 14000 trajectories are simulated in order to reduce discretization errors. The initial conditions are determined as follows: longitudinally, the starting position for all atoms is at $z = -2w_0$, i.e. outside the laser field, where $z = 0$ is defined by the light field center. The initial x position is given by choosing a pseudorandom number homogenously distributed over the interval $[0; 1]$ and subsequent multiplication with λ. The initial transversal velocity is chosen according to equation 4.2 and the longitudinal velocities are distributed between 200 and $2000\frac{\mathrm{m}}{\mathrm{s}}$ at intervals of $10\frac{\mathrm{m}}{\mathrm{s}}$ according to equation 4.1. Furthermore, the atoms are equally distributed among all magnetic sublevels. The different coupling strengths are considered by substituting the incident intensity I_0 by $I_0 \to C^2(m_g, m_e)I_0$ in equation 2.45. Spontaneous emissions may also lead to a redistribution of the magnetic sublevel populations but it can be assumed that this effect averages out.

[1]The transversal velocity distribution in the experiment is typically not exactly Gaussian. Alternatively, the FWHM value or integral values such as the divergence angle are occasionally used that is defined by the width within that 50% or 90% of all atoms are found (see section 3.3.2).

Having performed the numerical integration of the equations of motion, the resulting flux distribution during the interaction with the standing wave is determined by binning the atomic position values at some position in direction of propagation z into equally spaced containers and counting the number of atoms. These histogram plots reflect the local flux distributions. In addition, a convolution with a Gaussian function of 30nm width is applied. This procedure helps to reduce any irregularities that occur due to the finite number of simulated trajectories and accounts qualitatively for the growth phenomena.

An example for simulated trajectories and the resulting flux distribution at a certain point is shown in figure 4.1. The important nanostructure features are the structure width and the pedestal. In general, the width is specified by its full-width half maximum (FWHM) value and the pedestal (background) is characterized by the ratio between pedestal u and total structure height $\frac{\mathrm{u}}{\mathrm{u+h}}$. For clarification, pedestal and width of a simulated structure are depicted in figure 4.1(b).

4.1.2 Blue vs. Red Detuned Standing Waves: Theory

Atom-light interaction based nanofabrication provides a number of different experimental approaches that are promising candidates for the realization of atomic nanostructures with a high structure contrast. In the standard scheme based on using conservative dipole potentials as focusing masks for atoms, the pedestal originates primarily from spherical aberrations of the standing wave lens.

Therefore, a detailed analysis of the to date most commonly used standard thick lens focusing scheme is given here. The dressed state potentials of a standing wave light field with peak Rabi frequency $\Omega_0 = 400\Gamma$ and detuning $\Delta = \pm 50\Gamma$ for both red and blue detuning are shown in figure 4.3(a). For blue detuning, the $|1\rangle$-state is the long-lived state and for $\Delta < 0$ the atoms are predominantly occupying the $|2\rangle$-state.

Obviously, the potential shapes differ significantly around their minima. First of all, around its minimum the curvature of the $|1\rangle$-state potential is much larger but the range where a harmonic approximation is valid is small. Only in a vicinity of $\pm$15nm around the standing wave nodes the deviation of the parabola from the sinusoidal potential is less than 10%. Outside this region, the potential must be described by higher order terms which then lead to aberrations. All atoms entering the standing wave potential outside this quadratic region will cross the optical axis (along the node) later than those starting near the potential minimum. In the focal plane itself given by the paraxial solution given in equation 2.49 this leads to a blurred focus and a nonvanishing pedestal.

One method proposed to reduce spherical aberrations is the use of a mechanical mask that acts as an aperture in front of the light lens array. This mask has to be a free-standing grating accurately manufactured with a pitch[2] of $\frac{\lambda}{2}$. Furthermore, this mask must be perfectly aligned such that the grating bars overlap with the anharmonic parts of the optical potential. This technically challenging setup is currently under experimental investigation in the group of K.A.H. van Leeuwen at the Eindhoven University of Technology (Bosch, 2002).

Using red detuned light fields greatly overcomes the disadvantage of anharmonic potentials as can be seen in the bottom part of figure 4.3(a). Here, the region that

[2]Otherwise, the standing wave period has to be adjusted to the mask periodicity by means of tilting the incident laser beam.

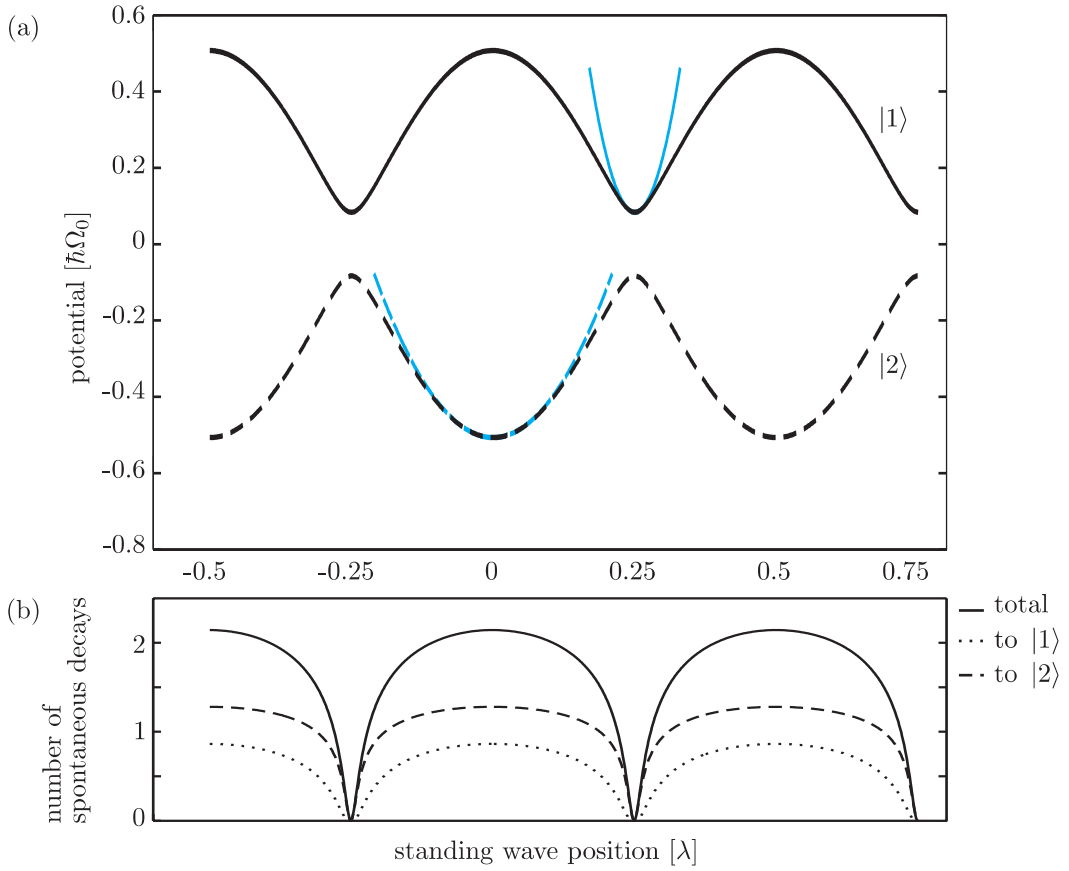

Figure 4.3: (a) Dressed state potentials in a standing light wave with $\Omega_0 = 400\Gamma$ and $\Delta = \pm 50\Gamma$. For $\Delta > 0$, the long-lived state is $|1\rangle$ and vice versa. The parabolas indicate the harmonic range of the standing wave lens around their minima. The curvature of $|1\rangle$-state potential is significantly stronger than the $|2\rangle$-state potential but the range where the parabola approximates the potential is much smaller. (b) Averaged number of spontaneous emissions for an atom during the interaction time 100ns with the light field: near the nodes of the standing wave, the probability for a spontaneous event is strongly suppressed whereas near the maxima around two spontaneous decays may occur.

deviates by less than 10% from the ideal parabola is approximately $\pm\frac{\lambda}{6}$ such that around two third of all atoms entering the light field are focused simultaneously and the resulting background should be greatly reduced.

But this simplified picture is modified by the effect of spontaneous emissions which is expected to be more important for red detuning. In doing so, two processes must be distinguished: first, the atom experiences a recoil kick with an associated velocity change of $1.8\frac{\mathrm{cm}}{\mathrm{s}}$ upon a spontaneous emission event which is negligible in our velocity range of the focused atoms (few $\frac{\mathrm{m}}{\mathrm{s}}$). Whereas the change of dressed state has a much more severe impact because it leads to an instantaneous acceleration of the atom in opposite direction. This momentum diffusion is sometimes referred to as diffusive abberation (Dalibard and Cohen-Tannoudji, 1985).

To elucidate the influence of spontaneous emissions it is instructive to compute their average number in a standing wave during the complete interaction. A rough estimate for the probability of these events can be derived as follows: neglecting the coherences between two dressed states and assuming that the atom occupies only the long-living state the decay rates given in equations 2.35 simplify to

$$\gamma_1 = \Gamma \sin^4 \theta \tag{4.3}$$

$$\gamma_2 = \Gamma \cos^4 \theta \tag{4.4}$$

Since the angle θ depends on the transversal position of the atom in the standing wave and along the Gaussian profile, the numbers of spontaneous events (neglecting the motion of the atom) at some standing wave position can be calculated by integrating the decay rates over the interaction time with the Gaussian light field. The position dependent numbers of spontaneous emissions are shown in figure 4.3(b).

Clearly, the spontaneous emissions are strongly suppressed at the standing wave nodes. Near the intensity maxima approximately two spontaneous emissions occur on average such that the atoms focused to the potential minimum of red detuned light fields have a larger probability to undergo a spontaneous emission when they are focused. At this point it is important to distinguish between state keeping and state changing spontaneous decays. Only those with a change of the dressed state lead to momentum diffusion. For $\Delta < 0$ the atom is initially in state $|2\rangle$. Therefore, the majority of spontaneous emissions does not lead to a change of the dressed state and focusing is only slightly degraded for these processes.

The interesting question that arises here is whether momentum diffusion is more spoiling for focusing in red or blue detuned light fields. From a standpoint of sisyphus-like cooling, blue detuning is clearly favorable (Aspect *et al.*, 1986; Stützle *et al.*, 2003). In these schemes, atoms are decelerated (cooled) and localized near the standing wave nodes upon multiple spontaneous emissions preferably near the high intensity regions of the light field. Furthermore, Aspect *et al.* showed that red detuning leads to a heating of the atoms. However, the sisyphus cooling argument requires interaction times much longer than one natural lifetime because at least hundreds of spontaneous emission events are required to significantly cool and localize the atoms. A nanolithography scheme utilizing this high intensity approach and nonconservative dipole forces has been recently demonstrated in the group of W. Hogervorst at the University of Amsterdam (Petra *et al.*, 2004).

Since the interaction times in our atomic nanofabrication experiments are only on the order of few natural lifetimes, strong localization effects that eventually help to suppress the background originating from spherical abberations cannot be expected. Therefore, the effect of spontaneous emissions must be analyzed numerically using the Monte-Carlo method introduced in section 2.4.1. For comparison, atomic trajectories in red and blue detuned light fields with the following light field parameters typical for an experiment were simulated: the peak Rabi frequency was chosen $\Omega_0 = 400\Gamma$, the detunings $\Delta = \pm 50\Gamma$ and the waist of the laser beam that forms the standing wave is $w_0 = 50\mu$m. The initial conditions for the simulations are discussed in detail in section 4.1.3. A grayscale plot of the simulated atomic flux distributions during interaction with a Gaussian standing wave lens centered at $z = 0$ is shown in figure 4.4.

For both detunings the atoms are focused to their associated dressed state potential

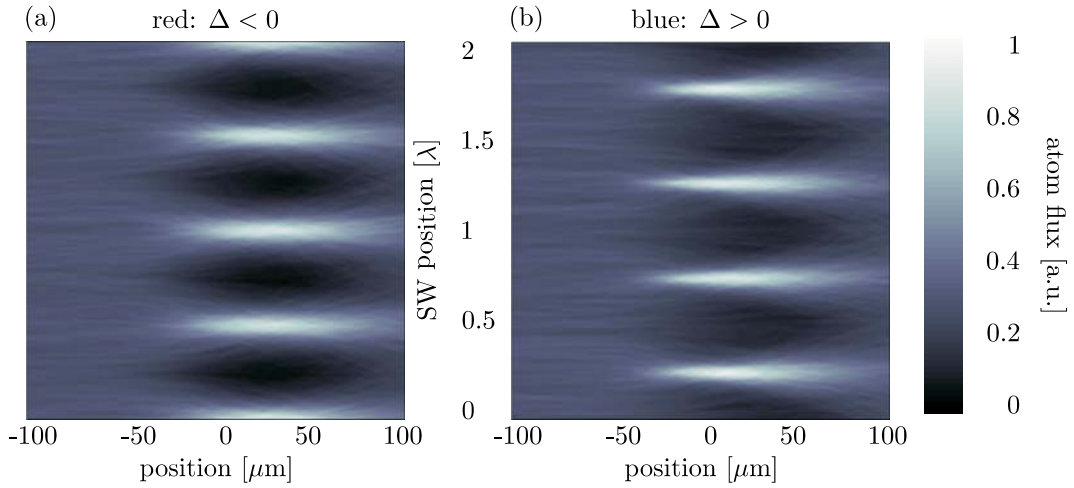

Figure 4.4: Focusing of a thermal atomic beam with a transversal velocity spread of $\sigma_t = 0.3\frac{\mathrm{m}}{\mathrm{s}}$ in a Gaussian standing wave with a laser beam waist of 50μm. The peak Rabi frequency is chosen to be 400Γ. The grayscale picture shows the simulated flux during interaction with the light field. The detunings are (a) $\Delta = -50\Gamma$ (b) $\Delta = 50\Gamma$. Whereas the focusing in the red detuned case leads to a larger contrast, the flux distribution appears narrower for blue detuning.

minima near the center of the Gaussian envelope. In the case of blue detuning the potential gradient is larger as can be seen in figure 4.3 and, thus, leads to a faster localization.

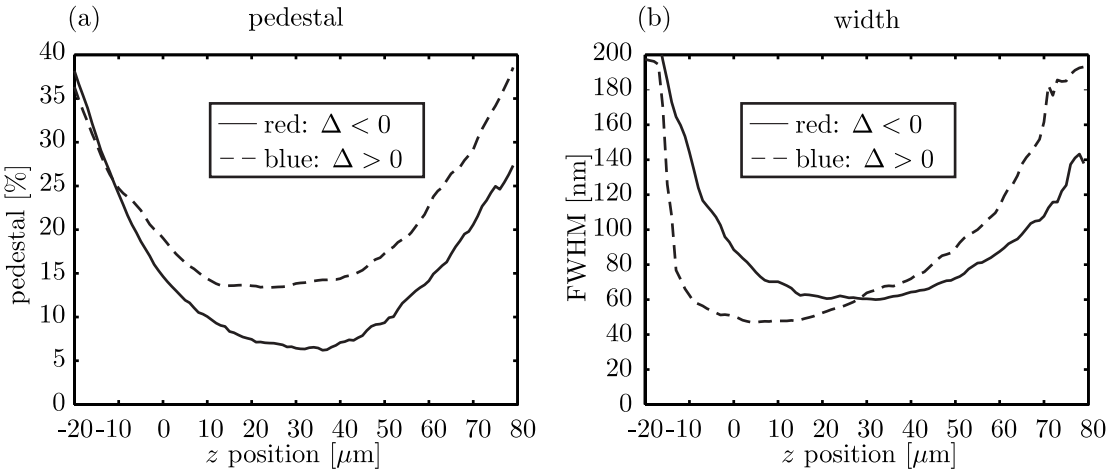

Figure 4.5: Analysis of focusing in red and blue detuned standing waves along direction of propagation z. (a) For $\Delta < 0$ the pedestal can become as small as 6% whereas the minimum for $\Delta > 0$ is 13% (b) Feature widths (FWHM): In blue detuned light fields the attainable feature widths are somewhat smaller. This is primarily due to a larger pedestal.

A detailed quantitative analysis of the focusing is displayed in figure 4.5. Here, the cross sections of the above flux distributions were measured with respect to structure

width and pedestal according to figure 4.1. The remaining pedestals are displayed in figure 4.5(a). For red detuning the pedestal can become as small as 6% at $z = 36\mu$m and remains below 10% for a z range between 10 and 50μm, whereas the minimum for blue detuning is 13% at $z = 24\mu$m. Thus, using red detuned light fields is a promising approach to reduce the important structure background by a factor of two to less than 10%.

The structure widths during interaction with the light field are shown in figure 4.5(b). For $\Delta < 0$ the minimal feature width is 60nm at $z = 33\mu$m, and for blue detuning 47nm at $z = 5\mu$m.

Cross sections for both positive and negative detuning at their optimal focus positions are shown in figure 4.6. For a better comparison, the structures for $\Delta > 0$ are shifted by $\frac{\lambda}{4}$ what compensates the lateral offset in this graph.

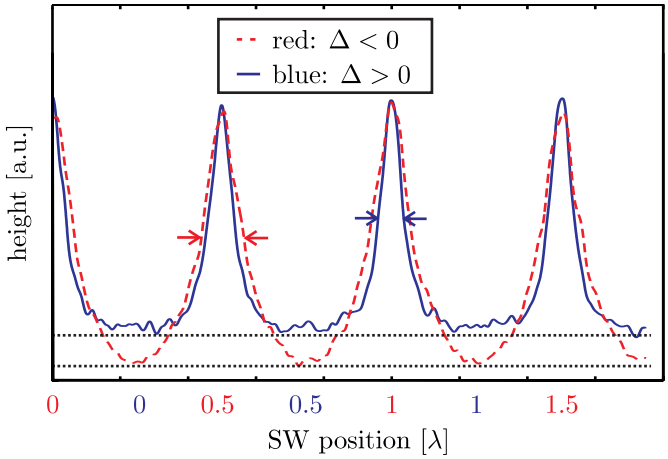

Figure 4.6: Cross sections of the narrowest structures in red and blue detuned standing waves. For convenience the structures obtained from the blue detuned light field were shifted by $\frac{\lambda}{4}$. A larger pedestal as in structures made with blue detuned light fields does eventually lead to smaller structure widths.

The flux distributions obtained from focusing in blue detuned light fields are slightly narrower than those from red detuning. However, the difference of 13nm in feature width is mainly due to the fact that there is a larger pedestal for $\Delta > 0$ as can be seen from figure 4.6. The FWHM values are determined from measuring at first the structure heights from their valleys to the peaks and subsequently the corresponding width. Hence, a structure that completely fits underneath the narrower line shape for blue detuning but with a lower pedestal would also have a larger FWHM value. For an evaluation of the overall performance, one therefore has to keep in mind that it is the combination of both pedestal and structure width that is important to the applicability of nanostructures.

The numerical simulations suggest that using red detuned laser fields in atomic nanofabrication is a promising method to improve the structure contrast because the improved harmonicity of the standing wave potential around its minima significantly reduces spherical and higher order abberations. This advantage even overcomes the drawback that spontaneous emissions are more likely near the antinodes of the standing wave.

4.1.3 Experimental Results

Having discussed the advantages of atom focusing in red detuned off-resonant standing wave, our experimental results are presented here. After the description of the experimental scheme is outlined, the angular and position alignment procedure is discussed. The angle between standing wave and atomic beam and the substrate position relative to the standing wave are the critical parameters of the experiment and can be directly checked by atomic force microscope (AFM) measurements of our nanostructures. This part is an essential preparatory work to achieve optimal suppression of the structure background. Then, a series of atomic nanofabrication experiments with different peak intensities and substrate positions relative to the standing wave was performed and analyzed for both red and blue detuning. Finally, the proposed scheme for background suppression is analyzed in detail. The results found are confirming our proposed scheme and are also in good qualitative agreement with theory.

Experimental Scheme and Analysis

A description of the experimental setup and how a deposition is conducted was already given in chapter 3. Here the main focus is directed towards the important parameters of the experiment and the results obtained from the subsequent AFM analysis. A schematic overview of atomic nanofabrication is shown in figure 4.7(a).

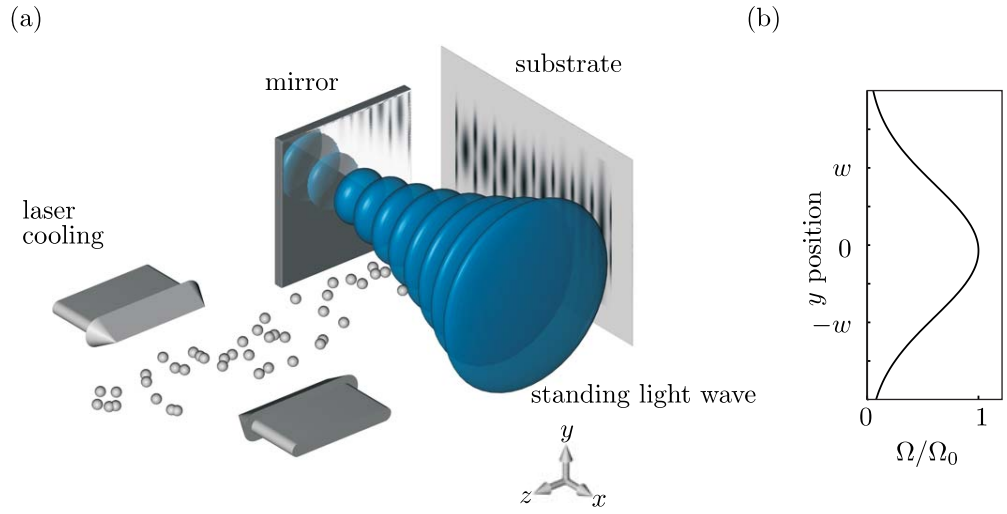

Figure 4.7: (a) Experimental scheme of atomic nanofabrication. A transversally laser cooled atomic beam impinges perpendicular onto a standing light wave. After traversing the light field the chromium atoms are deposited on a silicon substrate which is placed in or behind the center of the standing light wave. (b) The Rabi frequency shows a spatial dependence due to the Gaussian laser beam profile along the y-direction. Thus each individual substrate contains the whole intensity dependence of the atom-light interaction.

An atomic beam collimated by transverse laser cooling to less than 1mrad divergence impinges perpendicular onto a standing light wave which is realized by retroreflecting a Gaussian laser beam from a mirror. After traversing the light field, the chromium atoms

are deposited onto a substrate[3] which is placed in or behind the center of the standing light wave. The laser beam that forms the standing wave lens array is Gaussian in both y and z direction. While the z intensity dependence directly influences the focusing properties of an individual potential well, the intensity profile along the y axis allows to deduce the full intensity dependence of the focusing properties because the intensity and thus the Rabi frequency changes in y-direction as indicated in figure 4.7(b) due to the Gaussian profile of the light field. Thus one deposition represents a whole series of atomic nanofabrication experiments with different peak intensities and a fixed position of the substrate with respect to the light field.

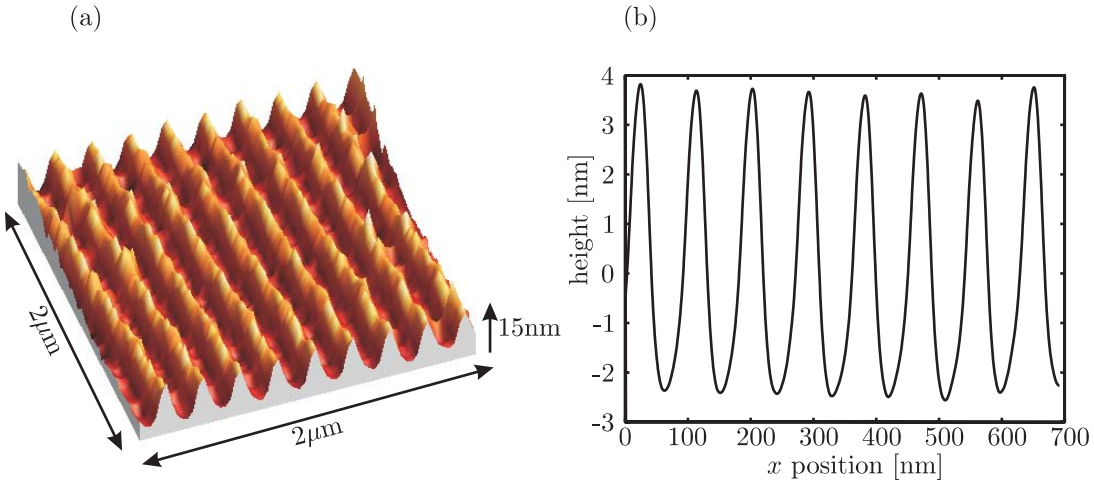

Figure 4.8: (a) AFM image of chromium nanostructures fabricated with an untilted standing wave. (b) Averaged cross section of the adjacent line structure.

After 30 minutes of deposition[4], the sample is taken out of the UHV chamber, mounted on a special sample holder and analyzed with an AFM[5] in air. The nanostructured region on the substrate spans around two to three laser beam waists (100-150μm) in y direction and approximately 1mm along the standing wave in x direction because the atomic beam is only around 1mm in diameter after passing two differential pumping stages as described in chapter 4. When the deposited chromium layer is thick enough, a little grey spot with 1mm diameter is visible near one substrate edge. One then has to scan the AFM tip in x direction over the chromium spot starting at the upper or lower edge (with respect to the y-axis given as shown in figure 4.7) until the expected periodic line structure shows up. Having found the nanostructured region a series of $2 \times 2\mu\text{m}^2$ images at interval of typically 5μm are taken along the y-axis.

Most AFM measurements were performed in tapping mode and few of them in contact mode. A three dimensional top view of a $2 \times 2\mu\text{m}^2$ image is shown in figure 4.8(a). The chromium grating on top of the substrate reveals a pronounced surface modulation of around 7nm height with perfect periodicity. The chromium lines are apparently

[3]Four different types of substrate were used in the experiments: silicon, germanium, glass (SiO_2) and sapphire

[4]This is the deposition time for most experiments presented unless otherwise stated.

[5]Digital Instruments (DI)

continuous and defect free. In order to determine the characteristic quantities of our fabricated nanostructures the two dimensional data set is processed with an averaging algorithm as follows:

First, the raw data obtained from the AFM measurement is read in and converted to a MATLAB-data file. Any obvious imperfections due to dust particles on the sample surface are removed numerically. Then, the data matrix is approximated line by line with a second-order polygonal fit procedure. To allow for a consistent stringing together of all individual AFM pictures this polynomial is then subtracted from the raw data such that the offset is removed. After this step, the mean value for all images is zero which reflects the homogeneous flux throughout the sample. Any lateral offsets due to drifts during data acquisition are compensated by a shear and shift algorithm such that the maxima (chromium lines) of two adjacent AFM images fit together and the chromium lines run vertical. Finally, for the quantitative analysis a vertically oriented line structure is averaged over typically few hundred nanometer along the chromium lines. The averaged cross section associated to the AFM image is shown in figure 4.8(b). Clearly, the line structure exhibits perfect periodicity. In a final step the structure widths and heights are determined for each peak and again averaged.

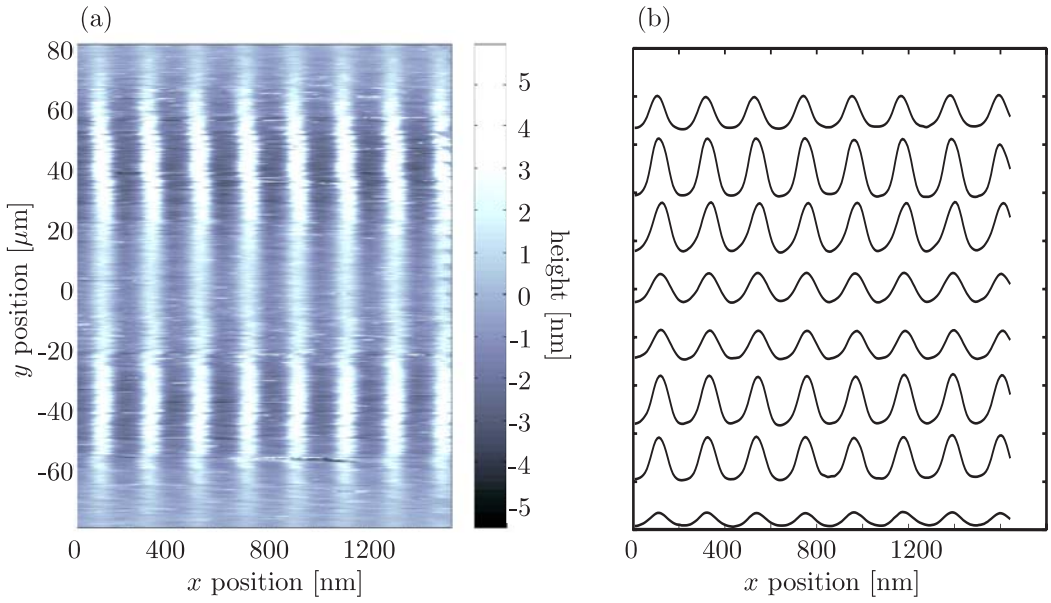

Figure 4.9: (a) Overview of chromium nanostructures revealing the Gaussian envelope in y direction. Here, 33 individual AFM images are strung together. (b) Corresponding cross section averaged over 100nm along y-direction.

An interesting overview of the total nanostructured region is shown in figure 4.9(a) where 33 postprocessed AFM images as the one above are strung together such that a sample segment of approximately $160 \times 2\mu\text{m}^2$ is imaged[6]. The corresponding cross sections averaged along the y-direction are shown in figure 4.9(b). This overview reveals the full symmetric intensity dependence of the focusing properties of a standing wave

[6]It must be noted that due to the 5μm spacing between the images there is a gap of 3μm not shown in the overview. However, the change in the structure shape is comparably slow, therefore, the images are directly strung together.

lens array. It can be seen that the chromium lines in the central range are lower and broader compared to the region approximately 40μm from the beam center. Apparently, the focal plane in this high intensity region is located before the substrate such that the image is out of focus on the substrate and blurred. Whereas about 40μm from the standing wave center the focal plane of the lens array coincides with the substrate and the resulting structure is narrower and higher.

Alignment Procedure

So far, the focusing properties of the standing wave lens array were discussed under the assumption that the light field is aligned perfectly perpendicular to the atomic beam. But this is a critical issue of the experiment, especially when the main focus of the work is on the reduction of the background. In the experiment, the dielectric mirror surface used for the formation of the standing wave is coated onto one leg of a right-angled prism as shown in figure 4.10. The atomic beam is therefore perpendicular to the standing wave when the normal of the second cathetus plane points in the direction of the atomic beam (Greiner, 2003).

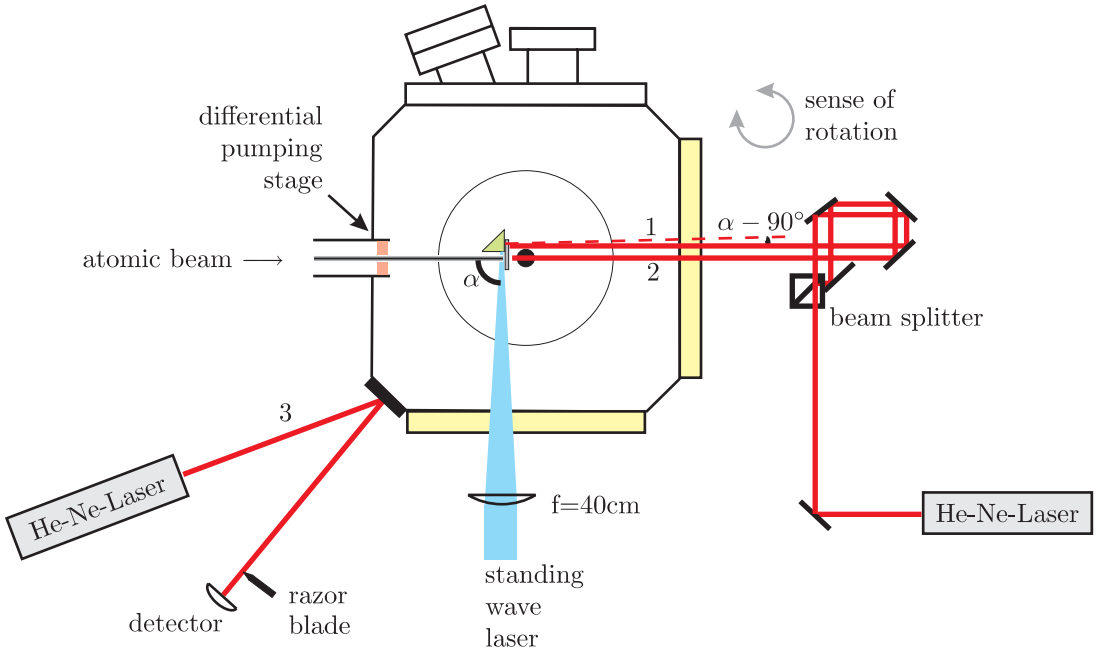

Figure 4.10: Alignment of standing wave. The UHV deposition chamber is rotatable as indicated by the twisted arrow. The coarse alignment of the right-angled prism is done by reflecting laser beam 1 back in itself while the parallel beam 2 points directly onto the atom source. For the fine adjustment another laser beam 3 is reflected from a mirror mounted onto the outside of the UHV chamber and imaged onto a razor blade. A measurement of the the laser power behind the razor blade with a photodetector allows to determine the relative rotation of the chamber with high precision.

To align the prism in this way we used a pair of parallel laser beams from a He-Ne-laser. Beam 2 was aligned onto the atomic beam axis given by the two differential pumping stages and then tweaked symmetrically onto the aperture behind the effusion

cell that defines the beam source. The parallel beam 1 propagates about 5mm parallel to beam 2 and is adjusted onto the back surface of the prism. The pivotable UHV chamber is then rotated such that beam 1 is reflected in itself. According to the prism manufacturer[7], the prism is at a right angle with an accuracy of ±3 minutes of arc or 0.9mrad. The accuracy of the alignment laser beams with respect to the atomic beam is on the same order of magnitude. Thus, a tilt of up to 2mrad of the standing wave with respect to the atomic beam axis is likely to be introduced, even with much care during the alignment. With a geometrical optics argument, one can estimate the shift of the imaged nanostructures with respect to the standing wave. Assuming an atom lens focal length of 50μm and an angular tilt of 2mrad leads to an offset of the line structure of 100nm. Moreover, a 2mrad tilt corresponds to an additional transversal velocity of the atoms of $2\frac{\mathrm{m}}{\mathrm{s}}$. Thus only that portion of atoms with a transversal kinetic energy smaller than the potential depth are sill being focused whereas all faster atoms can overcome the adjacent potential hill and contribute to the feature background.

On the other hand, one can make use of the angular sensitivity for an optimized alignment of the mirror prism. For this purpose, we set up a second He-Ne-laser (beam 3) and a distinctly larger measurement range of 3m that allows for a significantly more accurate relative measurement of the chamber rotation angle of 0.1mrad. Here, the relative angle is determined with a razor blade that must be positioned such that the laser power incident on the detector is just halved.

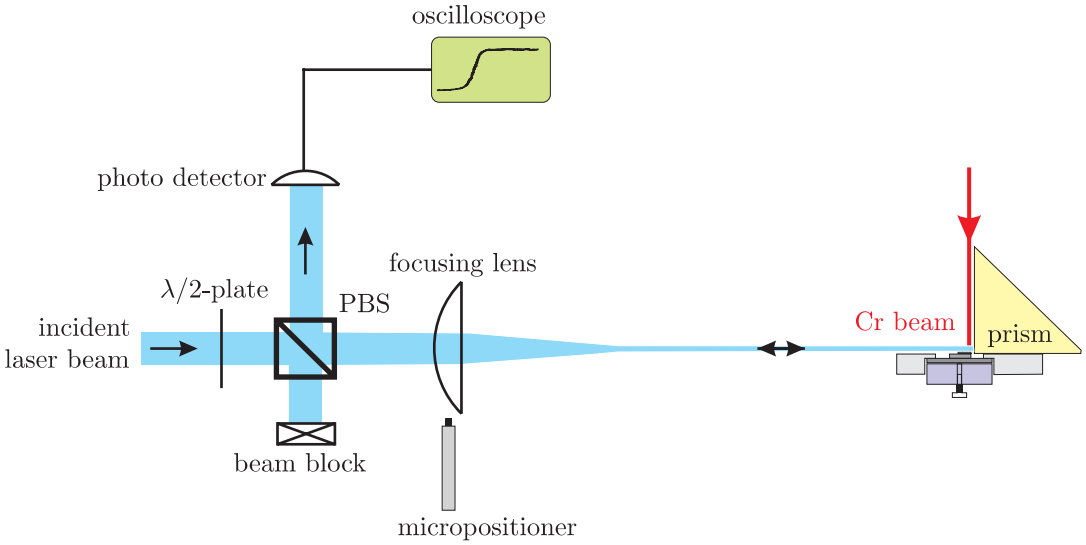

Figure 4.11: Substrate positioning using retroreflected light from the mirror prism. A small amount of the reflected light has the right polarization to be reflected from the beam splitter cube. The focusing lens is mounted on a translation stage with a micropositioner. When the lens is linearly scanned over the substrate edge the reflected power incident on the photo detector has the profile of an error function as denoted on the oscilloscope.

The angular fine adjustment was then done as follows: at first, we performed the alignment procedure for the beams 1 and 2 and measured the corresponding deflection

[7]Laser Components GmbH

value of beam 3. Then we deposited the chromium atoms for 30min through a red detuned light mask with 13mW of incident power and beam waists $w_y = 37\mu$m and $w_z = 50\mu$m. This corresponds to a peak Rabi frequency in the light field of 57 Γ while the laser detuning was -52Γ. The substrate was positioned 50μm behind the laser beam center because focusing in the thin lens regime enhances the angular sensitivity. Furthermore, the intensity dependence of the nanostructured region is expected to be more pronounced: to provide for such an accurate standing wave positioning, a spherical lens (focal length f=40cm) outside the vacuum was mounted on a translation stage. The micrometer screw used for adjusting the axis parallel to the atomic beam was replaced by a controllable micropositioner[8] with a resolution better than 1μm. To find the beam center the power of the reflected light beam is measured with a photodiode while the lens and the beam focus are scanned over the substrate edge. The recorded error function profile allows to determine the half-power value with high precision. The described alignment scheme is shown in figure 4.11. Having produced this sample, two further depositions with relative angles of $\pm$1mrad of the mirror prism with respect to the first one were made whereas all other parameters remained unchanged.

A quantitative analysis of the cross sections from the nominally untilted and the tilted samples is shown in figure 4.12. For all depositions, both structure height displayed in figure 4.12(a),(b) and width shown in figure 4.12(c),(d) show a pronounced intensity dependence which in this representation translates as position dependence. For convenience, the y-axis is chosen symmetric about the local height minimum. Clearly, in this central region the atoms are defocused due to the large peak intensity and the narrowest and highest structures structures are found around 45μm from the center. Samples 1 ($+$) and 3 ($\diamondsuit$) exhibit nearly the same intensity dependence whereas the structures on sample 2 ($*$) are distinctly higher (by a factor of 2) and narrower (by $\approx$ 10nm). We conclude that the standing wave angle with respect to the atomic beam is in fact a critical issue of the experiment and can lead to a significant reduction of the structure contrast. Moreover, from the similarity of the curves for samples 1 and 3 we deduce, that they correspond to depositions made at $\pm$1mrad whereas sample 2 must have been produced with a nearly perfectly orthogonal standing wave.

Simulation Results and Discussion

Experimentally we observe a strong influence of a tilt of the standing wave with respect to the atomic beam. Therefore we conclude that those atoms that are not focused to the nanostructure contribute to the pedestal. To check these findings, simulations with the associated initial conditions, i.e. different mean transversal velocities, were performed. The numerical results for tilted and untilted standing waves are also shown in figure 4.12 as solid lines together with the experimental data. The theoretical data exhibit an excellent quantitative agreement with the experiment, especially, the height relations between the tilted and the untilted case are nicely reproduced. However, in order to find this agreement some parameters must be modified. In order to reproduce the defocusing behavior, the relative substrate positions and the Rabi frequency must be varied. The theoretical data shown here correspond to a peak Rabi frequency of $\Omega_0 = 69\Gamma$ and the substrate position for the untilted sample is 80μm behind the standing wave center

[8] Oriel Instruments, DC Encoder Mike

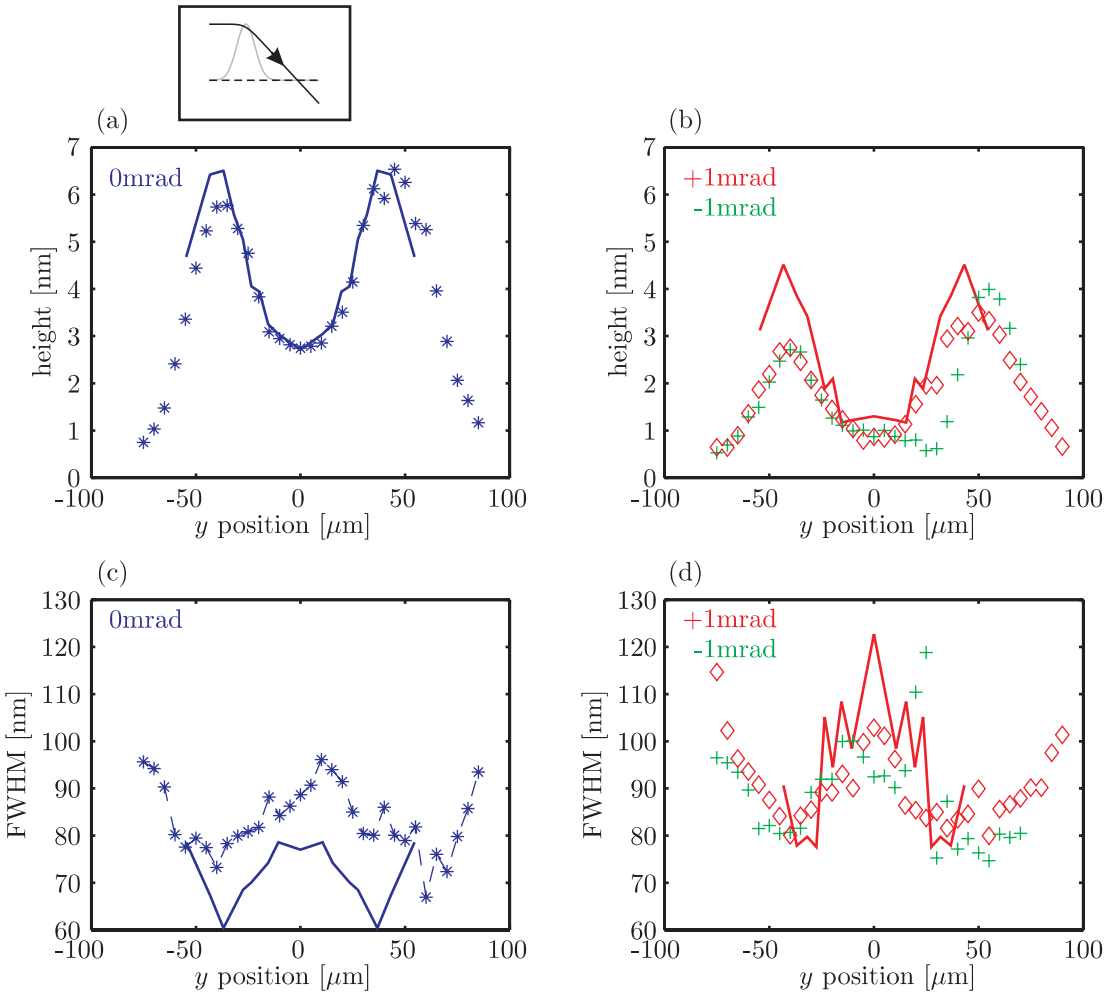

Figure 4.12: AFM measurements of nanostructures fabricated in the thin lens regime with differently tilted standing wave to find the optimum untilted setting. Structure heights in dependence of position y of (a) untilted and (b) $\pm$1mrad tilted standing wave. Structure widths in dependence of position y of (c) untilted and (d) $\pm$1mrad tilted standing wave. The solid lines correspond to theoretical data with a peak Rabi frequency $\Omega_0 = 69\Gamma$ and tilt angles of 0 and ($\pm$1mrad). The substrate position was adjusted to 80μm in the untilted and 100μm in the tilted case to reproduce the defocusing observed in the experiment.

whereas for the 1mrad tilted sample one even has to take a 100μm spacing.

In the following we will discuss whether these deviations are consistent with the error budget of the experiment: at first, the maximum Rabi frequency within the beam profile can be higher when one takes into account that the actual intensity distribution deviates from a Gaussian. The given values for the Gaussian beam waists are determined by measuring the incident power on a photo detector while a razor blade is scanned through the beam profile. The profile can be approximated by an error function but near the beam center the fitted function is typically flatter to compensate for the non-Gaussian decay towards the wings of the profile. Together with an uncertainty in the

(unstabilized) incident laser power of 2mW the peak Rabi frequency has an uncertainty of at least 20% and therefore the optimum value used in the simulation is justifiable.

Another critical point for all experiments is the relative position of the substrate with respect to the standing wave. The procedure described above is based on scanning the standing wave beam over the substrate edge. It certainly allows for reproducibly finding the position where half the beam power is cut off by the substrate.

Nonetheless, there is still a discrepancy in the defocusing behavior of the deposited structure which can only be explained by choosing the substrate position 30μm larger than it was initially set with the micropositioner. Essentially, this observation leads to the conclusion that the half power position measured with the photo detector does not coincide with the center of the light field. There are two points that appear to be responsible for this offset:

At first, the substrate might be slightly tilted, i.e. its normal vector is not perpendicular to the light wave vector. Then the substrate edge casts a shadow which causes an offset because the analyzed structures are near the prism. Knowing that this is a critical error source we used the alignment laser beam 2 (see figure 4.10) which directly points onto the backside of the substrate when it is built in. Since the prism and the substrate holder cannot be rotated independently it is crucial that the substrate is mounted as precisely as possible (see chapter 3) onto the substrate holder. This method allows to reduce the substrate tilt to around 2.5mrad. The width of the substrates is 4mm, thus, the shadow originating from the substrate edge can be estimated to around 10μm. Furthermore, this explains that for the case of 1mrad tipping of the standing wave the substrate position in the simulation must be chosen another 20μm larger.

The next uncertainty that again has to do with clipping the laser beam at the substrate edge is diffraction. Figure 4.13(a) illustrates how the intensity distribution is modified due to diffraction from the substrate edge. Assuming that the substrate surface is perfectly reflecting one can numerically solve the wave equation to determine the light field behind the diffracting edge. This was done (Anderson *et al.*, 1999) and the results are shown in 4.13(b). Profile 1 shows the light intensity distribution in z-direction for the situation where the substrate edge is at the Gaussian beam center and profile 2 for the case when the beam is 60μm above the substrate surface.

Both intensity profiles start from zero at the substrate surface, grow over a distance of a few tens of micrometers, and then decay with a series of oscillations that originate from diffraction. The key point is that the maximum of the diffracted intensity profile is shifted by around 30μm from the substrate surface and the higher orders might even be lost when the reflected beam is observed at a large distance. In either case, the diffraction from the substrate edge has a distinct impact on the intensity profile in z-direction. A numerical treatment of this effect is complicated because one then has to model the diffracted profile for each substrate position and power, at least for the case of immersed focusing.

Concluding, the discrepancy between the substrate position that was experimentally adjusted using the half-power measurement and the one used in the simulation is now understandable and for the comparisons between experimental results with theory one can take the substrate position as a free fit parameter within a certain range of few tens microns. In addition, one has to keep in mind that in future experiments this uncertainty must has to be taken into account for obtaining reproducible results.

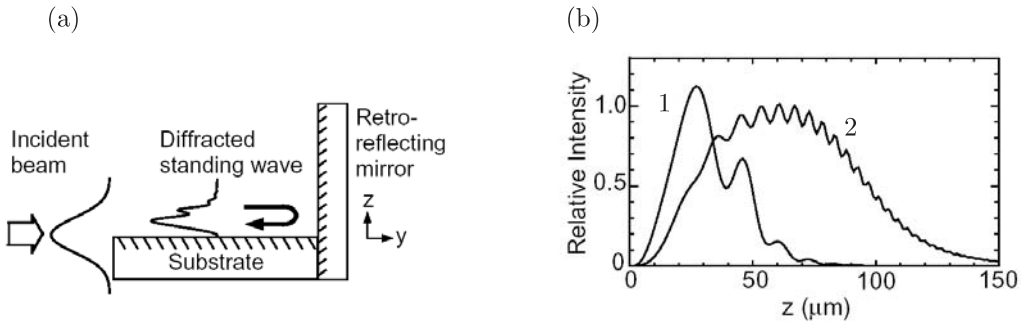

Figure 4.13: (a) Effect of diffraction of a Gaussian standing-wave laser beam at the substrate edge. (b) Calculations are done assuming that the incident beam has a 60μm waist, and the substrate and retroreflecting mirror are perfectly reflecting. The intensity distributions are shown for a position 1mm from the substrate edge. Profile 1 is calculated with the incident Gaussian beam center located at the substrate surface, and profile 2 is calculated with the center located 60μm above the surface. The oscillations in the intensity distribution are attributed to diffraction from the substrate edge (Taken from (Anderson *et al.*, 1999)).

For the further experimental work these results were extremely useful because now the standing wave was aligned perpendicular to the atomic beam with high accuracy.

Thin Lens Focusing

The three samples used to investigate the effect of slightly tilting the standing wave were all made in the thin lens regime, i.e. the substrate was placed behind the standing wave center[9]. The narrowest structures found on the untilted sample had a FWHM of 67nm whereas the narrowest structure width of the tilted samples was 75nm. As discussed in the previous section one observes that the intensity dependence for both structure height and width agrees well with theory, especially near the beam center. Towards lower intensities, i.e. more than one waist from the center, the beam profile differs from a real Gaussian because the intensity does not decay to zero as rapidly as expected. Therefore one observes nanostructures over a larger range than expected. Furthermore, the observed structure width for the untilted sample is around 10nm broader than simulated. In the thin lens focusing regime this can be attributed to an uncertainty in the atomic beam divergence of at least 0.1mrad.

The numerical simulations imply that the pedestal of the untilted sample is suppressed to around 15%, which would be on the order of the best contrast ratios ever produced, but before this can be claimed, it has to be confirmed experimentally as it will be done in a following section.

[9]Strictly speaking this is only true for those intensities that bring the focal plane into the substrate plane. At higher intensities, the focal plane is still within the light field and thus corresponds to the thick lens regime.

Immersed Focusing

Following the simple geometrical argument that the achievable minimal spot size is proportional to the focal length of the atom lens, it is desirable to work in the immersed focusing regime, i.e. the first focal plane lies within the lens. From an experimental point of view, it is ideal to place the substrate at the beam center because it is a special position that is reproducibly adjustable but the limits will be discussed in the following. The disadvantages are the issues discussed above in the context of beam clipping and diffraction at the substrate edge. Actually, real immersed focusing is not realizable in our experimental scheme because the atoms will always traverse a light-free region before they hit the substrate. Using the term 'immersed focusing' thus refers to placing the substrate into the light field. To investigate atomic nanofabrication in the high intensity regime and short focal lengths we performed two depositions at 50mW incident laser power. The substrate was positioned at the beam center according to the previously described 50% method. Special attention is paid to the influence of the laser detuning. Between both experiments we therefore switched the sign of the detuning from -52Γ to $+52\Gamma$.

The intensity dependence of the nanostructure heights is shown in figure 4.14(a),(b) and its widths are depicted in (c),(d). The narrowest structures found on the samples are 43nm for $\Delta > 0$ and 51nm for $\Delta < 0$. Thus, they are around 20nm narrower than those obtained from thin lens focusing as expected from the geometrical optics argument[10]. Again, one finds distinct intensity dependencies as well in feature height as in width. Near the symmetry point identified with the beam center the structures are broader due to defocusing. This effect appears to be slightly more pronounced for negative detuning. In addition, it is striking that the curves are somewhat asymmetric. To check this, we analyzed the AFM performance with another sample where we have seen that the scanner was not calibrated accurately throughout its full scan range of 80μm. Thus, some deviations in the symmetry may be contributed to this error. Nonetheless, the measurements exhibit a similar characteristic for both detunings. The maximal heights are identical but the narrowest structures found for positive detunings are up to 10nm, i.e. 20% smaller in FWHM than for the red detuned case. This finding confirms the theoretical prediction discussed in section 4.1.2. In figure 4.6 it was shown that the structure narrowing is mainly contributed to a larger pedestal underneath the nanostructures.

If one assumes that the beam profile in z-direction remains Gaussian, i.e. all beam clipping effects from the substrate are negligible, one finds that the structure width in the beam center decreases for higher intensities, independent of the sign of the detuning. (Schmidt, 1998; Stützle, 2001). In the high intensity regime atoms are strongly localized to the potential minima due to channeling (Salomon *et al.*, 1987). This is, however, in contrast with our experimental observation, where the focusing is optimal at around 40μm from the peak intensity. A similar observation was already made by Anderson *et al.* but in their work the peak intensity was by a factor of 3 smaller ($P =$ 20mW, waist $w =$ 60μm) than here and the resulting defocusing was less distinct (Anderson *et al.*, 1999).

In the high intensity range atoms are accelerated to higher velocities when they cross the minima due to the deeper potentials. This large velocity spread translates to broader

[10]Both depositions were made one after another with the same laser cooling parameters.

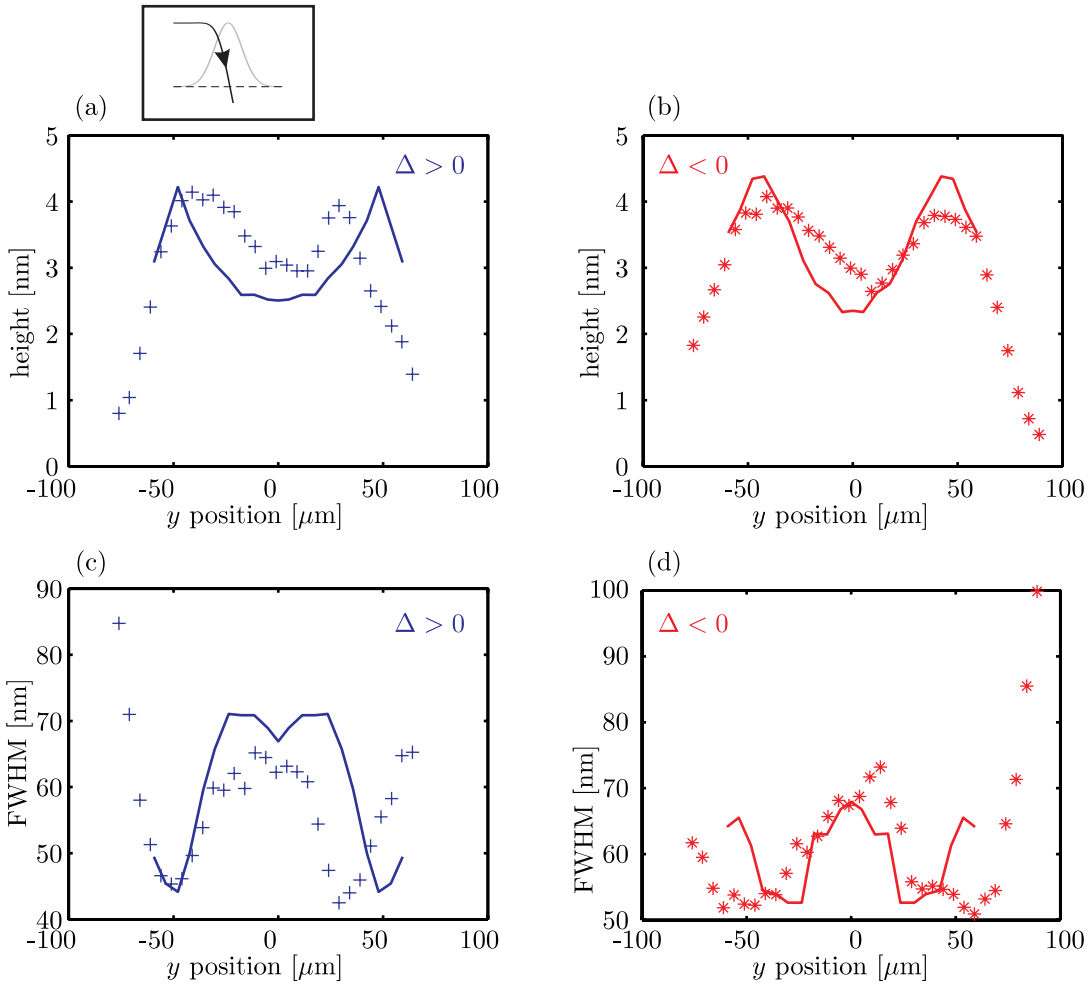

Figure 4.14: AFM measurements of nanostructures fabricated in the immersed focusing regime: Structure heights in dependence of y position for (a) $\Delta > 0$, (b) $\Delta < 0$. Corresponding structure widths for (c) $\Delta > 0$, (d) $\Delta < 0$. The experimental data is represented with markers ($+$ for $\Delta > 0$ and $*$ for $\Delta < 0$.) The theoretical (solid) curves correspond to substrate positions of $z = +22\mu$m for $\Delta > 0$ and $z = +35\mu$m for $\Delta < 0$.

structures when the atoms suddenly leave the light field as it is caused by the diffraction from the substrate edge. As discussed above and illustrated in figure 4.13 the quasi field-free range between intensity maximum and substrate is on the order of 30μm, i.e. the atoms propagate for around 30ns with their transversal exit velocity. Clearly, this can explain the feature broadening of around 30nm found in the experiment. To model the abrupt decay of the light field over the substrate plane the intensity dependence in z-direction was approximated by the following profile

$$g(z) = \frac{1}{2}\left(1 + \tanh\left(\frac{-5(z - 1.8w_0)}{w_0}\right)\right). \tag{4.5}$$

It is shown in figure 4.15 as dashed line ($--$) together with the initial Gaussian ($-$). Qualitatively, it agrees well with the numerical solution given in figure 4.13(b). Moreover,

the amplitude was adjusted to match the 50% value that was used in the experiment.

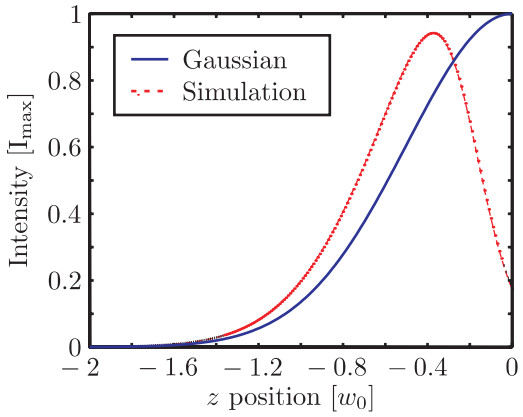

Figure 4.15: Intensity distribution of Gaussian beam and a modified profile as used in the simulation.

The results obtained from solving the optical Bloch equations with this profile and analyzing the calculated nanostructures are shown in figure 4.14. Theoretical plots for both red and blue detuning correspond to the solid lines. The best fits are found when the substrate positions are $z = \quad +22\mu$m for $\Delta > 0$ and $z = \quad +35\mu$m for $\Delta < 0$, respectively. These slightly differing values are attributed to the remaining uncertainty in the actual profile characteristics and shadowing from the substrate. Again, the only free parameter is the substrate position. The scaling factor that fits the theoretical curve for the height of the structures to the maxima of the experimental data is the same for both detunings. The theoretical curves for structure height show an excellent agreement with the experimental data. The theoretical and experimental feature widths also exhibit a reasonable agreement, at least within the error bars of a few nanometers.

In the previous analysis of the intensity dependence of structure height and width in off-resonant standing wave we have found that the theoretical description using optical Bloch equations agrees very well with the experimental findings. With both, blue and red detuned light masks feature widths of approximately 50nm or smaller are realizable in the immersed focusing regime. This is almost a factor of 2 wider then the 28nm lines fabricated in the McClelland group (Anderson *et al.*, 1999). In their work much attention was paid to the atomic beam divergence which was reduced to an angle of 0.17-0.2mrad (FWHM).

A reproducible alignment of such a high degree of collimation requires however, that before each deposition one has to measure the beam divergence and, if necessary, optimize it. But the main focus of this work is on the reduction of the pedestal. In the introducing part of this chapter the various beam parameters and their impact on the nanostructure formation were discussed and it was shown that the divergence angle primarily influences the attainable structure widths and not the pedestal. The results presented so far confirm this prediction because the beam divergence in our experiments was typically 0.5mrad FWHM. Thus the factor of 2 in comparison with McClelland's results is understandable. The next analysis is directed to the determination of the pedestal.

Suppression of Structure Background

In contrast to the surface analysis of the chromium structures using an AFM, the measurement of the pedestal turns out to be more complicated. In the past, several methods were applied. Drodofsky used steel tweezers to remove the chromium layer on top of the silicon substrate (Drodofsky, 1997). Since the oxide layer that covers the silicon is much harder than steel, the silicon surface is not being harmed by this scratch. He found that the pedestal of his structures fabricated in an immersed focusing setup using a blue detuned standing wave with a beam waist of 80μm is 54%. However, he could not perform systemic measurements with this method.

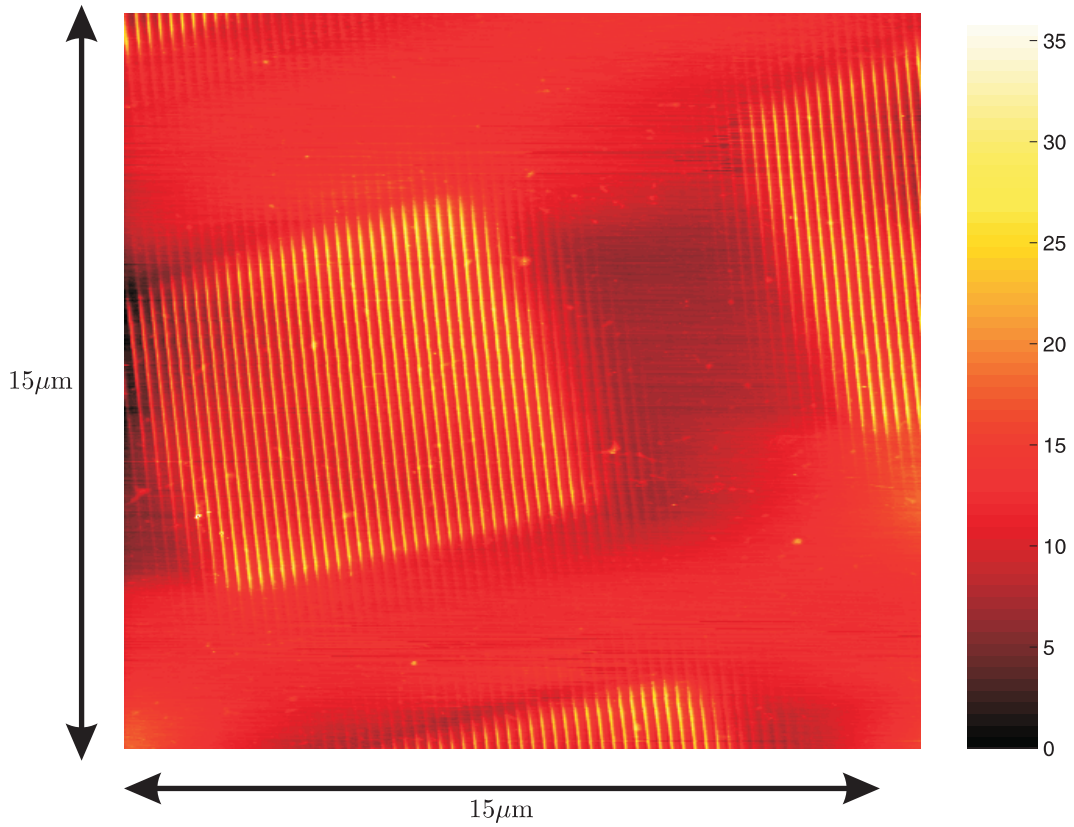

Figure 4.16: AFM image of nanostructures produced with copper grid on top. The chromium lines do not end abruptly at the edge of the grid because of their finite transverse velocity. From the covered regions one can deduce the absolute heights of the deposited nanostructures.

The measurements performed by Anderson *et al.* adopted another idea: by protecting part the chromium layer and subsequent chemically etching the unprotected region, they were able to measure the resulting step edge with the AFM. Here, the etchant does not etch into the substrate and, therefore, this is a reliable method. In addition, the uniform chromium layer thickness outside the structured region was measured with this etching method to determine the average thickness. The results given for the pedestal in that publication are somewhat puzzling and are also not a systematic analysis. Two numbers are explicitly given: for a peak height of 3nm they obtained a pedestal of 1.4nm (31%),

whereas nanostructure with a height of 47nm, the pedestal found amounts to 7nm (13%). Unfortunately, the corresponding widths are not given here and it is not clear whether the 13% are 'best ever' values. Our numerical simulations with slightly different parameters suggest that the lower limit for the pedestal in blue detuned standing waves is 13% which would be identical with their result.

For a more systematic analysis we pursued a different approach: instead of damaging the chromium layer with a chemical etchant or tweezers, we mounted a square TEM[11] copper grid with a pitch of 2000 lines per inch about 0.5mm above the sapphire substrate surface. The grid acts as a mechanical mask that shadows the chromium beam in a two dimensional periodic array with approximately $7 \times 7\mu\text{m}^2$ apertures. This method allows to directly deduce the pedestal by comparing the line structure in the unshadowed region with the uncovered region in the shadow of the grid. Moreover, the spacing between substrate and grid allows to shine in the standing wave beam directly above the substrate surface without damaging the grid.

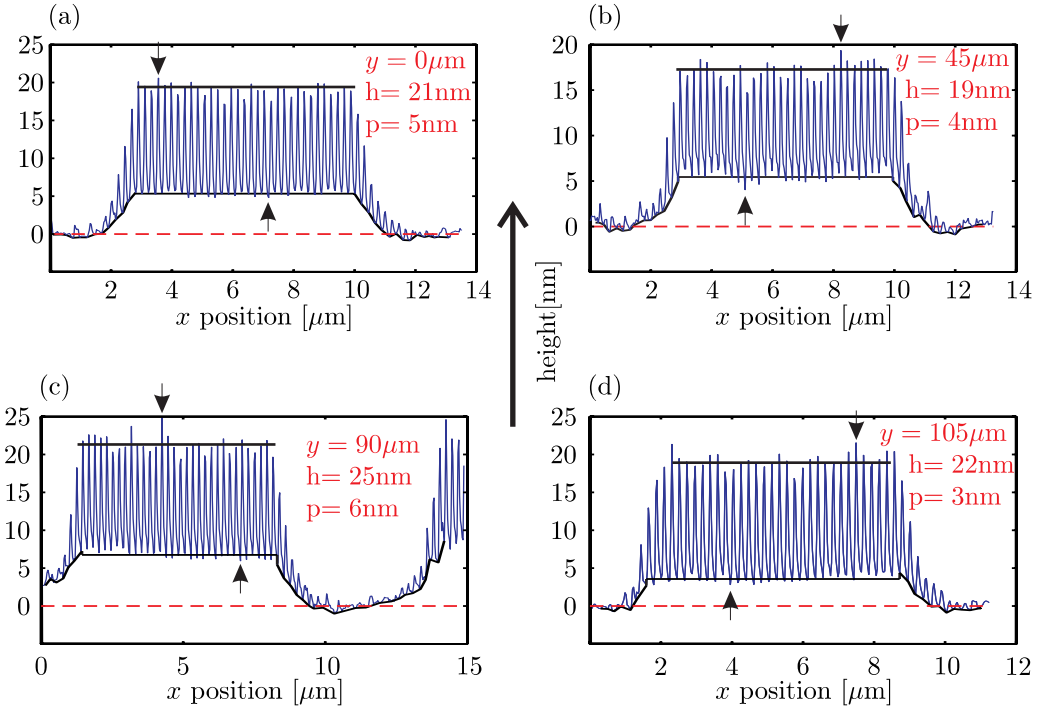

Figure 4.17: (a)-(d) Cross sections through sample fabricated with a copper grid on top. The maximal heights and minimal pedestals (both in nm) are displayed and indicated in the graphs by arrows. Their mean values are shown as solid lines. The lowest relative pedestal deduced from this deposition is found in (d) and amounts to 13%. The decline of structure height at the grid edges is attributed to the finite transversal velocity of the incident atoms.

Since the chromium flux rate at that time was only 2Å per minute we deposited for two hours to improve the signal to noise ratio. The following standing wave parameters were chosen: incident power $P = 20\text{mW}$, detuning $\Delta = -52\Gamma$. The standing wave was

[11] transmission electron microscope

y [μm]	$\overline{\mathrm{h}}$ [nm]	$\overline{\mathrm{p}}$ [nm]	$\mathrm{h_{max}}$ [nm]	$\mathrm{p_{min}}$ [nm]	$\overline{\mathrm{p}}$ [%]	$\mathrm{p_{min}}$ [%]
0	19.0	3.5	20.6	4.8	28	23.3
45	17.2	6.8	19.4	4.0	31.4	20.6
90	21.4	5.4	25.0	6.0	31.8	24.0
105	18.8	5.3	21.5	2.7	18.6	13.0

Table 4.1: Modulation of nanostructure at different y positions. The table shows average and extreme values for the peak and valley heights as indicated in figure 4.17. Average and mean relative pedestals are given in the last two columns.

positioned such that 60% of the incident power was reflected, i.e. still in the immersed focusing regime. An AFM measurement of the sample with $15 \times 15\mu\mathrm{m}^2$ dimensions is pictured in figure 4.16.

The image demonstrates that the chromium topography formed on the substrate is the negative pattern of the copper grid modulated with the periodic line structure from the standing wave. In between two chromium squares the line structure are continued for several μm until one comes to a region which even those atoms with the largest transversal velocities cannot reach. Four cross sections through different chromium squares are shown in figure 4.17. The y-positions of the measured range on the sample is displayed in the graphs. Evidently, the sinusoidal chromium topography drops off near the grid edges. At first, from this decline one can roughly estimate the transversal velocity spread:

By looking at the valleys of the chromium lines we find that the chromium thickness declines within 300nm to its $\frac{1}{\sqrt{\mathrm{e}}}$-fold value. Inserting a grid-substrate spacing of 0.5 ± 0.2mm, one obtains a Gaussian width of 0.6 ± 0.3mrad of the incident atomic beam divergence. This is roughly the same value as we typically found in our knife edge measurements. In the vertical direction, i.e. parallel to the chromium lines, the line height declines within approximately 450nm, which corresponds to a divergence half angle of roughly 1mrad which is in accordance with the vertical beam angle defined by the differential pumping stages.

Furthermore, the cross sections in figure 4.17(a)-(d) allow to determine the pedestal of our chromium nanostructures. The dashed line (–) indicates the substrate level, i.e. in these region no chromium is deposited, whereas the solid lines (-) are associated with the average heights of the minima and maxima found.

The absolute maxima and minima are indicated by an arrow. Comparing the four cross sections shows that the maximal h displayed in the graphs is around 20nm but the pedestal varies between 6 and 3nm. Hence, the structure background can become as small as 13% for figure 4.17(d) and outside this optimal focal regime it is still smaller then 30%. It must be noted that these values are upper limits because the limited pixel resolution of the AFM measurements (512×512 pixels) leads to spatial resolution of around 30nm, i.e. one feature period (213nm) is represented by only seven pixels. This low sampling resolution results in a signal beating visible in the cross sections: the periodic line pattern is modulated by a slowly varying envelope signal with around 2μm periodicity. To account for this effect, we choose the maximum heights and the lowest valleys as indicated by the arrows to determine the pedestal of 13%. The sampling error also complicates the width measurement because it systematically overestimates

the FWHM when the feature heights are not accurate. Nevertheless, the experimental result for the optimal pedestal is in excellent agreement with the theoretical prediction of around 10% depending on the substrate position used.

4.2 On-resonant Standing Waves: Quantum Mechanics

Using off-resonant light fields for atomic nanofabrication like in the preceding part has been widely investigated over the last decade in great detail. Beyond the simple one-dimensional scheme that was also used in the previous section further progress has been achieved in the extension of the method towards two and three dimensions (Gupta *et al.*, 1995; Schulze *et al.*, 2001). On the other hand, nanotechnology research continuously aims at reducing feature sizes and spacings of the fabricated nanostructures. In section 2.3.4 we have introduced the conceptual idea of employing exactly resonant light fields as a universal method to reduce the periodicity by a factor of two and, thus, allows to surpass the $\frac{\lambda}{2}$ limit of the standard atomic nanofabrication scheme for a two-level atom. Here, the experimental results will be presented. First, they are compared to the intuitive dressed state picture and finally a fully quantum mechanical simulation is performed to explain the peculiar findings.

4.2.1 Experimental Results

As in the previous off-resonant experiments the chromium atomic beam is collimated to a divergence of less than 1 mrad (full width at half maximum) and impinges perpendicularly onto the exactly resonant standing light wave which is realized by retroreflecting a linearly polarized Gaussian laser beam (waists $w_z = 21 \pm 3\mu$m and $w_y = 35 \pm 3\mu$m, power $P = 17 \pm 2$mW) from a mirror. Thus the interaction time of the atoms with a mean longitudinal velocity $v_z = 1000\frac{\mathrm{m}}{\mathrm{s}}$ is on the order of the natural life time of the excited state. This implies that the internal dynamics of the atoms in our experiment is not in the steady state limit. The effect of spontaneous emission is not so obvious here because on resonance small intensities are sufficient to induce a spontaneous emission. However it can be estimated that a significant part can pass through the light field without a spontaneous decay and thus a flux modulation is still visible. After traversing the light field the chromium atoms are deposited on a silicon substrate which is placed $35 \pm 5\mu$m behind the center of the standing light wave. After 30 minutes of deposition, the sample is taken out of the high vacuum chamber and analyzed with an AFM.

In figure 4.18(b) the topography of the fabricated nanostructure is shown. The image consists of 42 overlapping AFM scans revealing the topography over 60 μm in y-direction. This method reveals the full intensity dependence of the focusing properties of a resonant standing light wave because the intensity and thus the Rabi frequency changes in y-direction as indicated in figure 4.18(a) due to the Gaussian profile of the light field.

The measured topography shown in figure 4.18(b,c) reveals that for high light intensities nanostructures with a periodicity of $\frac{\lambda}{2}$ corresponding to 213nm are produced. This is the same result as we obtained with an off-resonant standing light wave although in this experiment there is no force expected in the classical atom-light interaction picture. For smaller intensities we produce so far unobserved structures with a periodicity of $\frac{\lambda}{4}$ as can be seen clearly in 4.18(c). The extension of the conventional nanofabrication

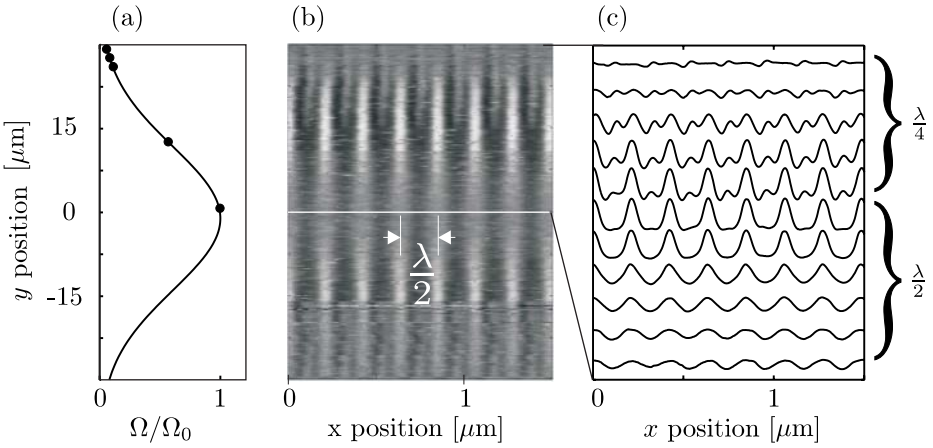

Figure 4.18: Experimental results. (a) The Rabi frequency shows a spatial dependence due to the Gaussian laser beam profile along the y-direction. Thus each individual substrate contains the whole intensity dependence of the atom-light interaction. (b) The AFM image and (c) cross sections reveal the light intensity dependence of the formed structures. For low intensity structures with $\frac{\lambda}{4}$ periodicity are observed showing that the on-resonant method can overcome the standard atomic nanofabrication limit of $\frac{\lambda}{2}$ for a two-level atom.

scheme to exactly resonant standing light waves can overcome the classical $\frac{\lambda}{2}$ periodicity limit. Furthermore, an unexpected asymmetry is observed. The periodicity of the one dimensional line pattern is not perfect as one expects from the intensity distribution of the light mask. A precise measurement of the cross sections reveals that the chromium line spacing differs by approximately 10nm from $\frac{\lambda}{4}$. In the following it will be shown that this feature can be attributed to the quantum nature of the atom-light interaction.

Moreover, a detailed analysis of the experimental findings will be given. At first, the observation of a periodicity of $\frac{\lambda}{2}$ at high intensities and $\frac{\lambda}{4}$ period structures at low intensities, is explained. Thereafter the asymmetry is analyzed thoroughly and finally compared to theoretical results.

Dressed States Description

Surprisingly, the periodicity of the nanostructures fabricated on resonance is not $\frac{\lambda}{4}$ throughout the whole sample. Nonetheless, this finding can be attributed to so-called nonadiabatic transition: near the nodes of the standing wave the energy gap between both dressed states becomes very small, for a perfect standing wave the gap even vanishes and the energy curves of $|+\rangle$ and $|-\rangle$-state merge as can be seen in figure 2.10(b). An atom initially in the $|+\rangle$-state thus will follow the potential curve and oscillate around the $|-\rangle$-state minimum. Given that the standing wave is in reality never perfect, there will always be a small gap between the potential curves. In our case, the dielectric mirror used in the experiment has a reflectivity of $R = 94\%$. Thus, the energy gap amounts to $0.03\hbar\Omega_0$. In deriving the dressed state energies, the atomic motion itself was neglected. This is a justifiable approximation when the atom moves very slowly in the dipole potential. But when the atomic velocity exceeds a certain value, the atom

can reach the other dressed state even without spontaneously emitting a photon. This effect is usually referred to as nonadiabatic transition also described as Landau-Zener tunneling. The probability for a nonadiabatic transition can be estimated by (Dalibard and Cohen-Tannoudji, 1985)

$$p_{i\to j} \leq \sup\left\{\frac{|\langle j,n;\mathbf{r}(t)|\overline{i,n;\dot{\mathbf{r}}(t)}\rangle|^2}{|\omega_{ij}(t)|^2}\right\}. \tag{4.6}$$

Here n stands yet for the (unchanged) photon number in the light field mode and ω_{ij} is the frequency that corresponds to the energy difference between levels i and j at time t, i.e. $\Omega(\mathbf{r}(t))$. To calculate this probability one needs the time derivative of the initial state. Since the problem is symmetric and nonadiabatic transitions will rather occur when an atom starts in the $|+\rangle$-state because it is accelerated to the gap minimum, it will suffice to determine the probability $p_{+\to-}$.

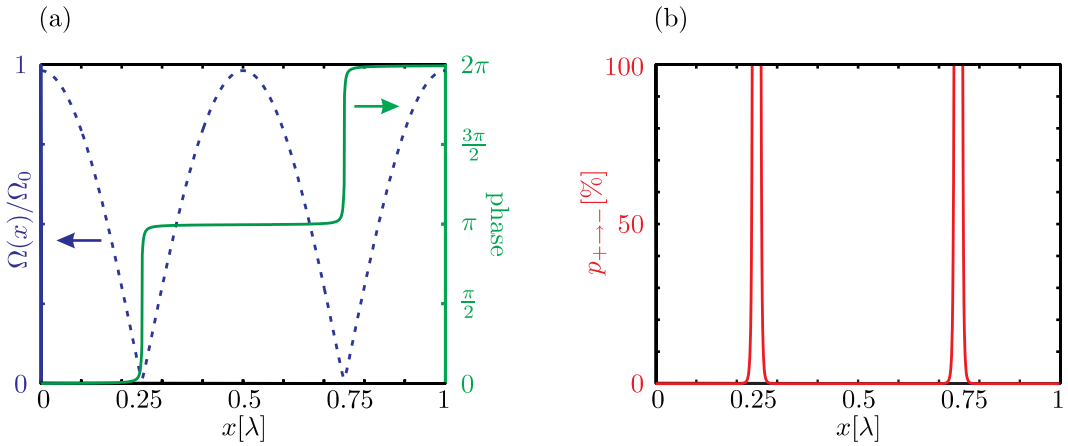

Figure 4.19: (a) Rabi frequency and phase of the light field in an imperfect standing wave ($R = 94\%$). At the nodes the phase of the field jumps by π.(b) Nonadiabatic transition probability in a standing wave with peak Rabi frequency $\Omega_0 = 100\Gamma$. The atomic velocity chosen to compute $p_{+\to-}$ is $2\frac{\mathrm{m}}{\mathrm{s}}$. In a vicinity of ± 5nm around the node the probability even exceeds unity and thus the made assumption of small transition probability breaks down.

The $|+\rangle$-state evolves as

$$\frac{\mathrm{d}}{\mathrm{d}t}|+,\mathbf{r}\rangle = v\frac{\mathrm{d}}{\mathrm{d}x}|+,\mathbf{r}\rangle, \tag{4.7}$$

where v is the velocity of the atom in the light field. Accounting for a mirror reflectivity $R < 100\%$ the phase of the light field has to be considered. Then, on resonance, the dressed states in direction x of the standing wave read

$$\begin{aligned} |+;\mathbf{r}\rangle &= \frac{1}{\sqrt{2}}\left(\mathrm{e}^{-\frac{1}{2}\varphi(x)}|g\rangle + \mathrm{e}^{\frac{1}{2}\varphi(x)}|e\rangle\right) \\ |-;\mathbf{r}\rangle &= \frac{1}{\sqrt{2}}\left(\mathrm{e}^{-\frac{1}{2}\varphi(x)}|g\rangle - \mathrm{e}^{\frac{1}{2}\varphi(x)}|e\rangle\right), \end{aligned} \tag{4.8}$$

where the phase $\varphi(x)$ in a standing wave is deduced from the total electric field

$$\mathbf{E} = \mathbf{E_0}\left(\mathrm{e}^{ikx} + r\mathrm{e}^{-ikx}\right). \tag{4.9}$$

Here, $r = \sqrt{R}$ is the mirror reflectance and $\mathbf{E_0}$ is the incident field. Rewriting the complex field as $\mathbf{E} = |\mathbf{E}|e^{i\varphi}$, one obtains for the magnitude of the electric field

$$|\mathbf{E}| = |\mathbf{E_0}|\sqrt{1 + R + 2r\cos 2kx}, \tag{4.10}$$

whereas the phase of the field and its gradient are given by

$$\varphi(x) = \arctan\left(\frac{1-r}{1+r}\tan kx\right) \tag{4.11}$$

$$\frac{\mathrm{d}}{\mathrm{d}x}\varphi(x) = \frac{k(1-R)}{1+R+2\sqrt{R}\cos 2kx}. \tag{4.12}$$

Inserting the reflectivity of our mirror used in the experimental setup, the phase dependence in the standing wave takes the form shown in figure 4.19(a).

Now, the spatial derivative of $|+,x\rangle$ can be easily determined and from that follows the subsequent expression for the nonadiabatic transition probability

$$p_{+\to-} \leq v^2\left(\frac{\frac{\mathrm{d}}{\mathrm{d}x}\varphi(x)}{\Omega(x)}\right)^2. \tag{4.13}$$

This expression for the nonadiabatic transition probability is in contrast to the usual treatment where the probability originates from the gradient of θ (Dalibard and Cohen-Tannoudji, 1985). In the on-resonant case $\nabla\theta$ vanishes whereas $\nabla\varphi \neq 0$ because of the nonperfect mirror reflectivity. Thus the nonadiabatic transition probability here is completely attributed to the gradient of the phase.

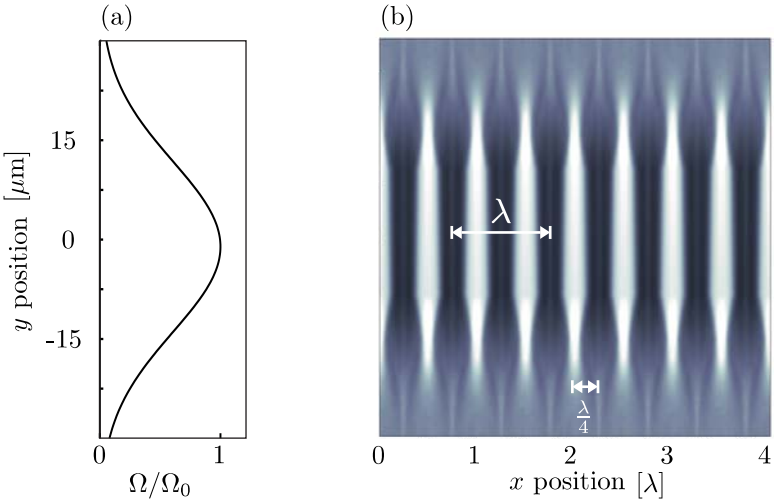

Figure 4.20: Theoretical prediction based on the simple potential picture. (a) Gaussian envelope on y-direction. (b) Simulated flux distribution 35μm behind the standing wave center. Here, nonadiabatic transitions between both dressed states are considered. For low intensities, chromium lines spaced at $\frac{\lambda}{4}$ periodicity can be found whereas for higher intensities the periodicity is only $\frac{\lambda}{2}$. Spontaneous emissions were neglected.

The position dependence of the nonadiabatic transition probability in a standing wave is plotted in figure 4.19(b). The maximum coupling strength was chosen to be

$\Omega_0 = 100\Gamma$ and the atomic velocity is directly deduced from the maximal potential energy in the light field where an atom can be accelerated up to $2\frac{\mathrm{m}}{\mathrm{s}}$. Near the nodes the nonadiabatic transition probability can become quite large and in a vicinity of $\pm$5nm around the node the probability even exceeds unity and thus the assumption of small transition probabilities (Fermi's golden rule) breaks down[12]. We also found out that the observation of $\frac{\lambda}{4}$-structures in this picture strongly depends on the position where a nonadiabatic transition occurs. If one chooses that the transition takes place directly at the node, no remaining localization at the node is found. Thus we conclude that the localization at the node originates from the transition 5nm away from the node. The atom in the $|-\rangle$-state then first has to run up the associated potential hill what retards the focusing to the lower potential minimum.

This estimate nonetheless shows that it is very likely for all atoms that approach the node of an on resonant standing wave in the $|+\rangle$-state to make a nonadiabatic transition to the $|-\rangle$-state and thus be focused to the minimum of that potential, i.e. to the antinode of the standing wave.

This also explains the observation made in our experiment: in the high intensity region, the oscillation time for atoms in the $|+\rangle$ potential is shorter than the interaction time, but when the atoms cross the node, they tunnel to the lower potential and are then focused at $\frac{\lambda}{2}$ periodicity to the antinodes of the standing wave. However, for interaction times shorter than a quarter of an oscillation time in the (upper) axicon potential, which depends on the light intensity, a localization at both, nodes and antinodes can be expected. Thus, the dressed state analysis gives a very simple way of understanding why the $\frac{\lambda}{4}$ patterns are formed in the region with weak light intensities. These findings are also confirmed by a semiclassical dressed state simulation. Here, initially one halve of the atoms starts in the $|+\rangle$-state and the other halve in the $|-\rangle$-state. Their motions are governed by the associated dressed state potentials and nonadiabatic transitions are incorporated by the following method: the dressed atom changes its state when the nonadiabatic transition probability $p_{+\to-}$ exceeds the arbitrarily chosen value[13] 0.3. The light field parameters for the simulation are chosen according to the experimental values.

The atomic flux distribution 35μm behind the standing wave center is shown in figure 4.20. In the high intensity region the periodicity is $\frac{\lambda}{2}$. About one waist from the beam center, nanostructures perfectly spaced at $\frac{\lambda}{4}$ are found. Therefore, this simple potential picture gives a good qualitative agreement with the experimental observation. The strong defocusing observed at high intensities is not reproduced by our simulation. This is because spontaneous emissions were neglected here. According to section 2.2.4 they lead to a feature broadening due to momentum diffusion upon a dressed state changing spontaneous transition.

Furthermore, the simple dressed state potential picture cannot explain another prominent observation made:

In figure 4.18(c) and figure 4.21(a), one can see that the fabricated $\frac{\lambda}{4}$ nanostructures reveal a pronounced asymmetry although the dressed state potentials are perfectly symmetric. However, the symmetry is broken due to the phase of the Rabi frequency. The discussed semiclassical description of the motion is only correct for light fields with

[12]This range is not too sensitive on the atomic velocity. It is rather the mirror reflectivity and thus the phase gradient that determines the range where nonadiabatic transitions occur.

[13]This value is not critical due to the fact that the nonadiabatic transition probability anyway increases quickly at the nodes.

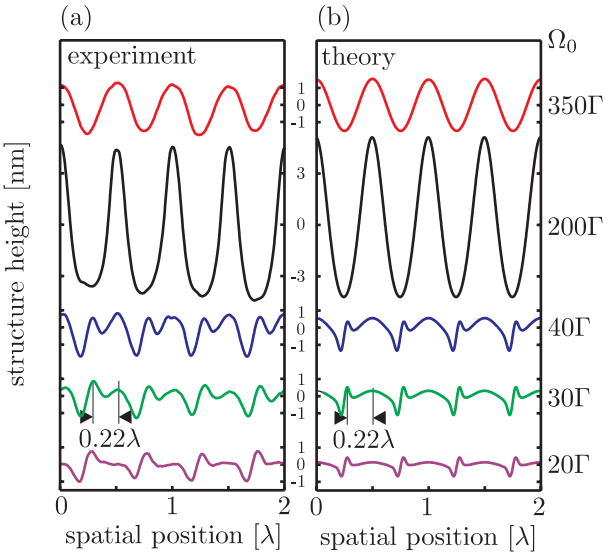

Figure 4.21: Asymmetric line structures: (a) AFM cross sections taken at different positions as indicated with solid circles in figure 4.18(a). (b) Cross sections of the calculated atomic flux 35μm behind the center of the standing wave for the indicated Rabi frequencies. For large Rabi frequencies, $\lambda/2$ period nanostructures are formed, whereas low Rabi frequencies lead to $\lambda/4$ period structures with a distinct asymmetry. The experimental findings are in excellent quantitative agreement with the simulation with respect to the relative heights and the asymmetry of the formed nanostructures.

vanishing phase gradients. Therefore near the node the motion of the atoms has to be numerically integrated. But the dressed state picture allows us to understand the asymmetry qualitatively. As indicated on the right hand side of figure 4.22(b), an atomic wave packet in the ground state at rest at the light field node is described in the dressed state basis by a coherent superposition of dressed state wave packets moving with a momentum $mv = \frac{\hbar}{2}\nabla\varphi$. Starting from equation 4.12 the maximal phase gradient for our experimental situation is found at the node and amounts to

$$\left(\frac{\mathrm{d}}{\mathrm{d}x}\varphi\right)_{\max} = k\frac{1+r}{1-r} = 64k. \tag{4.14}$$

However, the slope quickly drops off over the extension of the wave packet. Within ±3nm around the node the phase changes by $\frac{3\pi}{4}$. From that we estimate the phase gradient induced velocity of a dressed state wave packet at the node of the standing light wave to be $\sim 26v_r$ where $v_r = \frac{\hbar k}{m_{Cr}} = 1.8\frac{\mathrm{cm}}{\mathrm{s}}$ is the recoil velocity and k is the wave number of the light. Thus one expects that atoms in the $|+\rangle$-state near the node run up the potential due to this velocity (indicated in figure 4.22(b)). An estimate of the expected asymmetry can be found by calculating the classical trajectory of a particle starting at the node with an initial velocity $\sim 26v_r$ in the linear potential $V(x) = \frac{\hbar k|\Omega_0|}{2}x$. For the interaction time of 40ns and a Rabi frequency of $|\Omega_0| = 20\Gamma$ we find the position to be shifted by 14nm from the node of the standing light wave. Experimentally we observe 12 ± 3nm as can be seen in figure 4.21(a).

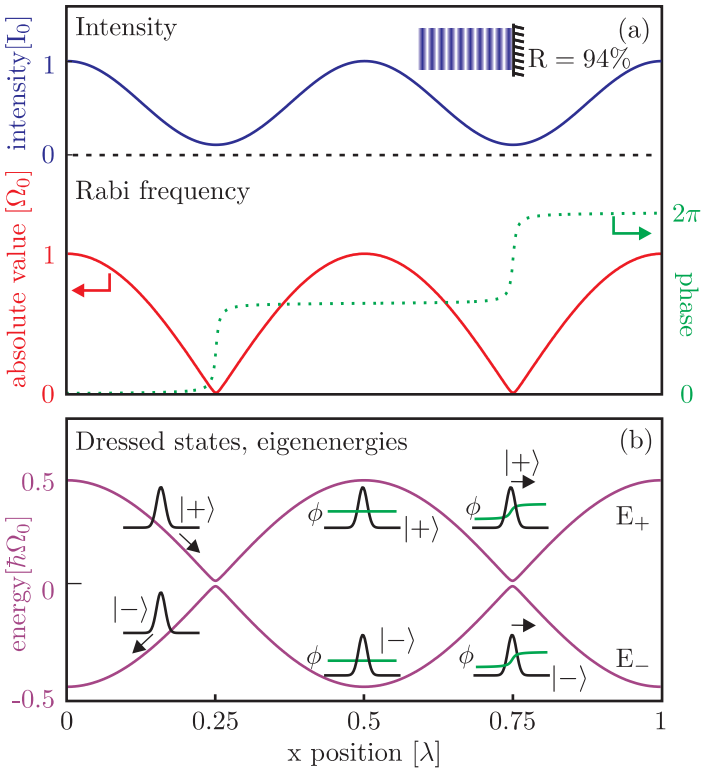

Figure 4.22: Dressed states description of on-resonant atom-light interaction: (a) The standing light wave is formed by retroreflecting a laser beam from a mirror with reflectivity $R = 94\%$ as shown in the inset. This leads to periodic intensity distribution that is not fully modulated. Hence, the Rabi frequency is complex. The change in phase proves to be dramatic at the standing wave node, where the phase jumps by π within few nanometers. (b) When the phase is constant, the ground state wave packet is decomposed into two resting dressed state wave packets as shown in the middle of the graph. Whereas near the nodes, this decomposition leads to two moving dressed state wave packets as depicted on the right hand side. Their motion is deduced from the dressed state eigenenergies, therefore a $|+\rangle$-state wave packet is attracted to the node and a $|-\rangle$-state wave packet to the antinode of the standing wave.

4.2.2 Quantum Simulation

In order to understand these experimental findings quantitatively, especially the asymmetry, we numerically solve the Schrödinger equation for the two level atom in momentum space as described in sections 2.3.5 and 2.4.2 (Efremov *et al.*, 2003). The two-level approach is still valid because the intensive linearly polarized standing wave light field couples only magnetic substates with equal quantum number ($\Delta m = 0$). Thus, there is no Raman coupling between different magnetic states that leads to a more complicated situation such as in polarization gradient light masks that were already discussed in section 1.2.3 (Gupta *et al.*, 1996).

Initial Conditions

The transversally collimated atomic beam is modelled as an incoherent sum of plane matter waves with a Gaussian momentum distribution. The calculations are done in momentum space (see section 2.3.5), thus the initial amplitudes a_n for a plane wave perpendicularly incident on a standing wave are: $a_0 = 1$ and $a_i = 0$, if $i \neq 0$. Accordingly, the initial values for a plane wave incident onto the light field with a transversal velocity component $v_t = nv_{\mathrm{rec}}$ are $a_n = 1$ and $a_i = 0$, if $i \neq n$. Because of the large computation times and giant amount of data produced the quantum motion is simulated for only one longitudinal velocity $v_z = 1000\frac{\mathrm{m}}{\mathrm{s}}$. Using an averaged Clebsch-Gordan coefficient of 0.65 accounts for the different coupling strengths of the involved magnetic substates. As in the off-resonant case we assume equally populated substates because after leaving the laser cooling stage where they might be polarized the atoms travel around one meter in a magnetically unshielded region before they enter the focusing region.

Effect of Spontaneous Emission

In order to find a quantitative agreement between the experimental findings and the numerical solution one has to empirically include the effect of spontaneous emission induced diffusion (Dalibard and Cohen-Tannoudji, 1985). The broadening effect due to the growth behavior of Cr (Anderson *et al.*, 1999) is in our experiment negligible since our structure widths are in the order of 70nm.

As discussed in section 2.3.5, spontaneous emissions lead to momentum diffusion that is proportional to the local Rabi frequency. The broadening of our nanostructures due to diffusion is incorporated into the quantum simulation by convoluting the probability distributions of the wave function with a Gaussian function of width $\Delta x = \frac{\Omega}{\Gamma} x_0$, where $x_0 = \frac{v_{\mathrm{rec}}}{\Gamma} = 6\text{Å}$ is the characteristic diffusion length (see section 2.2.4). Thus the impact of spontaneous emissions is only large in the high intensity regime $\Omega > 100\Gamma$ where experimentally a strong defocusing is observed ($\Delta x > 60$nm). Whereas in the $\frac{\lambda}{4}$ focusing regime ($\Omega < 50\Gamma$) the diffusion effect is comparably small ($\Delta x < 30$nm).

Simulation Results and Discussion

Cross sections of the calculated atomic flux 35μm behind the center of the standing wave are shown in figure 4.21(a) and are compared to the experimental findings shown in figure 4.21(b). The experimental cross sections are taken at positions indicated in figure 4.18(b) with solid circles. The shown theoretical curves are obtained for the indicated Rabi frequencies. These values are consistent within the uncertainty of the independent measurement of the incoming power and of the beam waists. The simulated flux is in very good agreement with the experimental finding for all Rabi frequencies, especially the asymmetry is very well reproduced. It is important to note that the structure width and height at high Rabi frequencies is dominated by the momentum diffusion resulting from spontaneous emission.

4.2.3 Nearly Resonant Standing Wave

In a further experiment we tested the prediction of the developed theory. The asymmetry should almost vanish for a $\Delta = 1\Gamma$ blue detuned standing light wave. Furthermore,

such a slight detuning shifts the dressed states populations towards a larger occupation of the $|+\rangle$ state. One can therefore expect a smaller tunneling rate between the dressed states and thus the $\frac{\lambda}{4}$ periodicity should be found all over the sample.

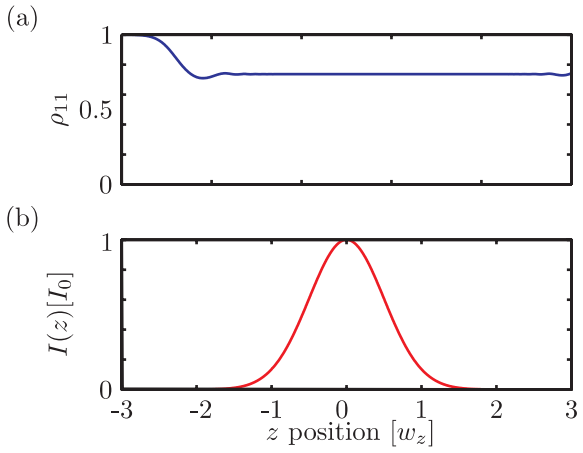

Figure 4.23: Optical Bloch equations: (a) Spatial dependence of dressed state population ρ_{11} during interaction with a Gaussian light field (b) Intensity distribution along the direction of propagation z.

The degree of adiabatic following when an atom enters an inhomogeneous light field depends however on the turn-on rate. An atom that enters the light field in its ground state can only evolve adiabatically into the new eigenstate $|+\rangle$ when the laser detuning is much larger than the critical detuning given by the turn-on rate of the laser field. For an atom moving with $1000\frac{\mathrm{m}}{\mathrm{s}}$ and a Gaussian light field distribution with a waist $w_z = 50\mu$m as shown in figure 4.23(a), this turn on rate is $50\mathrm{ns}^{-1} = 20$MHz, i.e. for detunings smaller than this critical value one can still expect a population of both dressed states and, thus, atomic focusing in both potentials. To obtain the resulting relative distribution of the dressed state populations one has to integrate the optical Bloch equations in longitudinal direction (Sleator *et al.*, 1992) neglecting any transversal motion. The population of the $|+\rangle$ state during the interaction is given in figure 4.23(a) for a Rabi frequency $\Omega_0 = 380\Gamma$ and a detuning $\Delta = +1\Gamma$. Outside the light field, the $|+\rangle$ state population equals one, since the atom is initially in its ground state. The population then drops off to a steady state value of 0.74, i.e. the $|-\rangle$ state will also be populated for such a small detuning. It is interesting to note that the redistribution reaches its steady state distinctly before the field maximum.

This experiment was done with a different experimental setting than those with $\Delta = 0$. Whereas the previous experiment was done in the thin lens regime, i.e. the substrate was positioned behind the standing wave, now the deposition took place in the immersed regime, i.e. the reflected power was cut off at 50%. The beam waist was 50μm, i.e. significantly larger than exactly on resonance, but the interaction length is still almost the same. The incident beam power was $P = 50$mW and the detuning was $\Delta = +1\Gamma$.

The AFM analysis shown in figure 4.24 is done in analogous manner as previously.

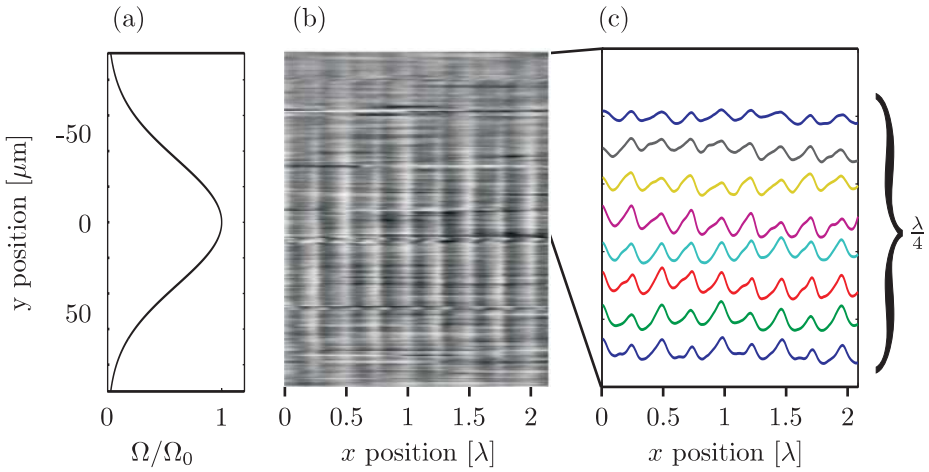

Figure 4.24: Experimental results. (a) Spatial dependence of Rabi frequency due to the Gaussian laser beam profile along the y-direction. (b) The AFM image and (c) band averaged cross sections. Throughout the whole sample nanostructures with $\frac{\lambda}{4}$ periodicity are observed.

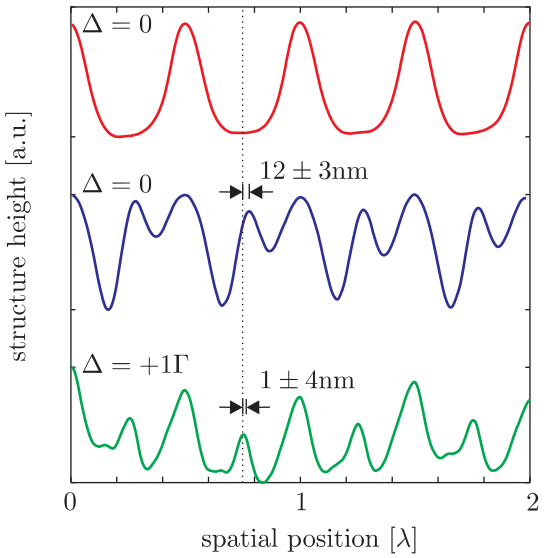

Figure 4.25: Comparison between nanostructures fabricated with different detunings: For $\Delta = 0$, $\lambda/2$ and $\lambda/4$ structures are shown to illustrate the asymmetry of 12 ± 3nm. The nanostructures obtained by detuning the laser frequency $\Delta = 1\Gamma$ exhibit a much smaller asymmetry of 1 ± 4nm. The observed behavior confirms the prediction by our quantum simulation.

For experimental reasons[14], the substrate on which the chromium was deposited had to be made of a thick glass slide. The cutting procedure was done with a diamond saw such that the surface was heavily contaminated with oil that could hardly be removed.

[14]Whilst the exactly resonant experiment was done in the 'old' high vacuum chamber, this deposition was already made in the new UHV chamber.

As can be seen the AFM image quality is distinctly worse than for the other sample. Nonetheless, the AFM image and the associated cross sections definitely show that the periodicity is now $\frac{\lambda}{4}$ throughout the whole sample in contrast to the exactly resonant case. Furthermore, no obvious asymmetry is apparent. The feature heights are quite small which can be attributed to a reduced atomic flux, but this makes is difficult to make more sophisticate quantitative statements. At least, one can see that the relative heights in the high intensity differ more than further outside the beam center.

To conclude the presented work on resonant atom-light interaction, our experimental findings are shown in figure 4.25, where we compare $\frac{\lambda}{2}$ focusing in the high intensity limit with the low intensity focussing for exactly on resonance $\Delta = 0$ and detuned $\Delta = +1\Gamma$ standing light wave. The observed asymmetry for exactly resonant standing light waves of 12 ± 3nm is in excellent agreement with the theoretical prediction of 12.7nm. In the detuned case the theory predicts 0.7nm which is also consistent with the measured asymmetry of 1 ± 4nm deduced from the pattern shown in figure 4.25.

4.3 Magnetic Nanostructures

Another fascinating perspective is the possibility to utilize chromium for the realization of nanostructured magnetic nanoalloys. In its crystalline form chromium is antiferromagnetic at room temperature, i.e. it exhibits no macroscopic magnetization. The chromium-platinum alloy $CrPt_3$ however can form a face centered cubic (fcc) crystal lattice with two possible states. Whereas the chemically disordered state is non-magnetic,

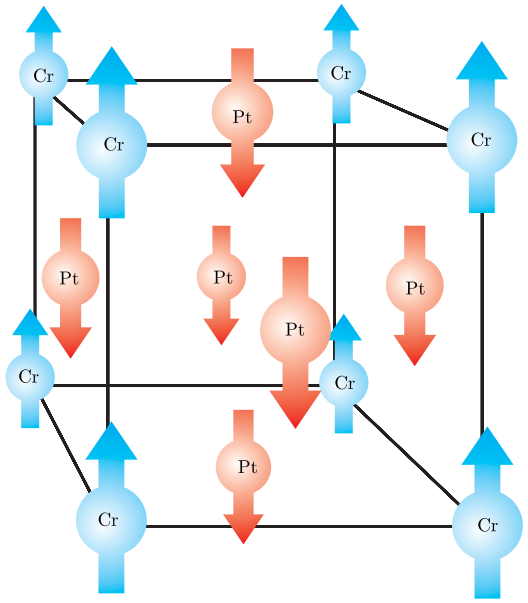

Figure 4.26: Lattice structure of $CrPt_3$. The chromium atoms occupy the edges of the unit cell and the faces of the cube are occupied by platinum atoms. The magnetic moments (indicated by arrows) of the chromium atoms point in opposite directions than those of platinum. The smaller magnetic moment for platinum than for chromium results in a net magnetization and ferrimagnetism.

the chemically ordered $L1_2$ state, that equals the $AuCu_3$ crystal structure, is ferrimagnetic (Maret *et al.*, 2000). A unit cell of the $CrPt_3$ crystal structure is shown in figure 4.26.

The magnetic moments of chromium are then aligned in the same direction whereas the magnetic moments of platinum point in the opposite direction. The magnetic moments of chromium and platinum are $\mu_{Cr} = 3.37\mu_B$ and $\mu_{Pt} = 0.26\mu_B$, respectively. Thus, the net magnetic moment amounts to $\mu_{total} = 2.59\mu_B$.

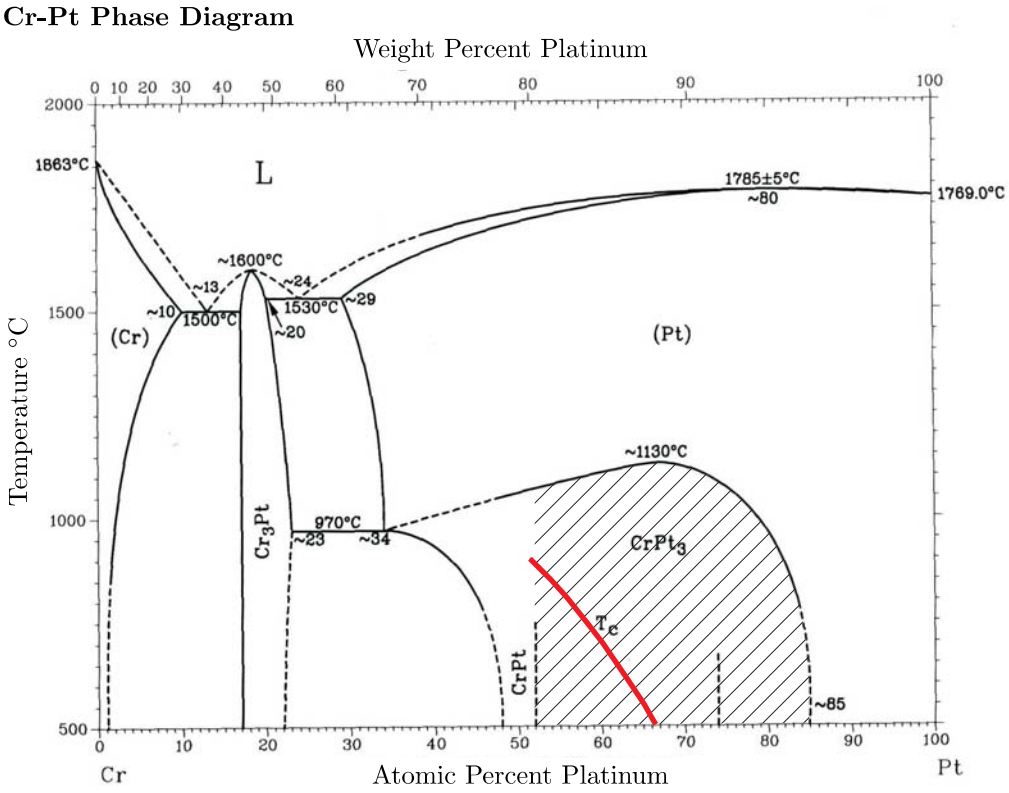

Figure 4.27: Phase diagram of Cr-Pt. The hatched region indicated the relevant range. The red straight line show the dependence of the Curie temperature on the platinum concentration (taken from (Massalski, 1996)).

The phase diagram of Cr-Pt is shown in figure 4.27. The hatched region indicates under which conditions $CrPt_3$ is formed. The Curie temperature curve furthermore indicates for which temperature value the ferromagnetism is lost. It depends on the relative concentrations of chromium and platinum and spans from 0K for 83at% Pt to 1173K for 52at%. In order to fabricate ferrimagnetic nanoalloys the Cr-Pt ratio has to be chosen such that the Curie temperature is above room temperature. Moreover, the substrate material is critical. To ensure crystalline growth of both platinum and chromium, silicon and germanium substrates are well suited because they provide a good lattice match with chromium and platinum.

4.3.1 Sample fabrication

The background suppression scheme we studied in detail in section 4.1 offers an ideal method to produce the described $CrPt_3$ nanostructures because we expect that the ferrimagnetic phase will be formed only in regions with an appropriate chromium-platinum ratio.

In close cooperation with the MBE group of Professor Schatz we have fabricated low background chromium structures for the subsequent magnetic nanostructure conversion. We pursued two different fabrication schemes in order to achieve this goal depicted in figure 4.28.

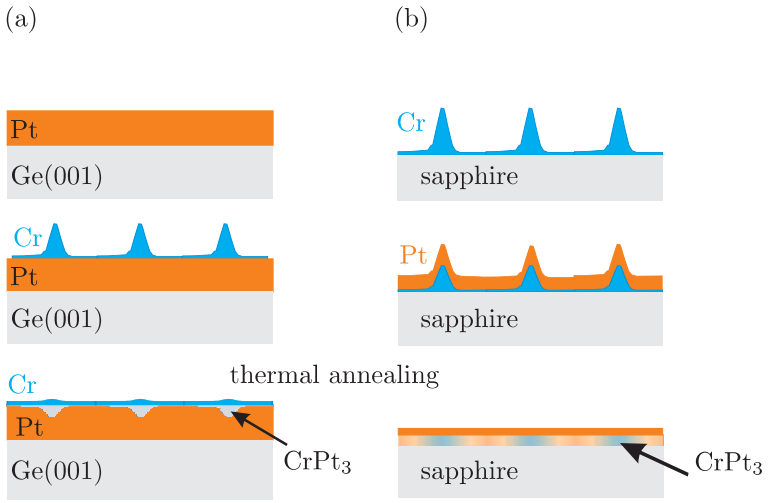

Figure 4.28: Fabrication schemes for ferrimagnetic $CrPt_3$ nanostructures. (a) After growing a platinum film on a germanium substrate, chromium nanostructures are deposited on top. Upon thermal annealing periodic ferrimagnetic $CrPt_3$ nanostructures should form. (b) First, chromium nanostructures are deposited on a sapphire substrate. This step is followed by a deposition of a platinum layer on top. Again, upon thermal annealing periodic ferrimagnetic $CrPt_3$ nanostructures should form.

The first one is shown in figure 4.28(a). A platinum buffer layer is grown on a germanium substrate in the MBE machine. These substrates where transferred into our UHV chamber and we deposited chromium nanostructures on top. Finally, they were transferred back into the MBE machine for thermal annealing.

The alternative method is shown in figure 4.28(b) where we first deposited our chromium nanostructures onto a sapphire substrate. The samples were then transferred to the MBE machine in order to deposit platinum on top[15].

Up to this point both processes proved successful. We were able to fabricate three samples with the first method and nine samples with the second one. Unfortunately, some problems with the sample heater in the MBE machine occurred so that up to now, the final thermal annealing step and an analysis of the magnetic properties of the samples could not yet be performed. But we still hope the best!!!

[15] A co-deposition of chromium and platinum could also work. But in our current setup no platinum source was built in.

4.4 Surface Growth of Nanostructures

So far, the comparison of our experimental results with the theoretical model was purely based on the assumption that the resulting nanostructures are a direct image of the flux distribution found from calculating atomic trajectories in the light field. This contradicts, however, the observations made by the group at NIST (Anderson *et al.*, 1999). Their very thorough analysis of all atomic beam and light field parameters essentially lead to the conclusion that the feature sizes of the chromium nanostructures are always 20-30nm larger than predicted by the calculations. Furthermore they found that in contrast to the simple geometrical optics argument, that suggests a linear dependence between atomic beam collimation and resulting feature width, there is 'no variation of the feature width seen over a range of collimations from 0.16 to 0.37mrad'. The observation that the feature width is dependent on the chromium film thickness suggests that the growth behavior has a strong influence on the attainable feature sizes. Another peculiar effect was observed when the substrate temperature during their depositions was varied between -70 and $+90$°C: the structure width revealed no temperature dependence.

Our experimental studies cannot doubtlessly confirm these observations. But in our experimental setup we were not able to measure the collimation of the atomic beam each time before we conducted a deposition. Thus, our knowledge of this important parameter is rather a rough estimate deduced from measurements once made before the final setup was in place. It is very challenging to realize collimations better then 0.5mrad and requires continuous realignment and a daily control. However, we could at least reproducibly adjust the beam collimation to values better than 1mrad. Accordingly, the feature sizes of our structures are at least twice as large as the 'best ever'-samples from the McClelland group. Hence, any growth effects that might play a role on the 20nm scale are certainly less pronounced for feature widths larger than 50nm as it is the case in our experiment.

Since it was found out that the atomic nanofabrication process is compromised by growth effects, several theoretical studies devoted to the role of nanostructure growth were conducted.

4.4.1 Growth Models

Jurdik *et al.* attempted to explain the broadening of the Cr nanostructures using thermally activated surface diffusion as a mechanism (Jurdik *et al.*, 1999). Various atomistic models were explored, and they found that the resulting structures exhibit a very strong dependence on substrate temperature and on the diffusion parameters which is in clear contrast with the experimental finding.

Then, Bradley *et al.* investigated the hypothesis that the surface diffusion was caused by the energy released when the atoms hit the surface, a process dubbed impact cascade diffusion (Bradley *et al.*, 2000). However, this theory does not explain the immense dependence on sample preparation conditions found in the in the atomic nanofabrication experiments with sodium citepbehringer1996.

Just recently, te Sligte extended Jurdiks thermal surface diffusion model, but accounted also for the effects of pollution (te Sligte *et al.*, 2004). For this purpose, they introduced two barriers to this model: a thermally activated Ehrlich-Schwoebel barrier, and impurities due to the residual gas in the vacuum system. Their results from

Monte Carlo simulations show that the Ehrlich-Schwoebel barrier cannot explain the insensitivity to temperature variations observed experimentally.

But the pollutant adatom hypothesis proves successful in explaining the observed dependencies of the structure width on temperature, vacuum conditions, and beam characteristics, at least for the results from Anderson *et al.*. Only the variation of structure width with deposition duration is not entirely reproduced by this model which they attribute to the one-dimensional nature of the simulations.

An interesting prediction made in their work is that improved vacuum conditions, i.e. less pollutant flux, will lead to an increased diffusion of chromium atoms such that the features will significantly become broader. The NIST experiments were performed in a vacuum system with a pressure of 10^{-8}mbar, which corresponds to a molecular background flux of around 2.5×10^{-3}ML/s. In our experiments, the pressure in the UHV deposition chamber is at least one order of magnitude better, i.e. $p < 10^{-9}$mbar. Since the molecular flux is proportional to the gas pressure, the pollutant flux during our depositions was reduced by at least a factor of 10. But it is rather the ratio between chromium and pollutant flux that determines the growth behavior. We can only estimate this ratio, but from the numbers given in the work published by McClellandd group (Anderson *et al.*, 1999), it appears that our flux is about five times smaller than in their experiment ($1\frac{\text{nm}}{\text{min}}$) and our chromium-pollutant ratio is only twice as high. For these numbers, the simulations shown in the paper published by the Eindhoven group (te Sligte *et al.*, 2004) suggest that the feature contrast would be reduced by 50% and the structure widths should become at least 80nm. At least the last statement cannot be confirmed by our experimental findings since we observe no feature broadening under UHV conditions but we also have to admit that the contributing flux numbers are not really too well known. Anyway, the question arises here whether the role of surface diffusion of chromium is overestimated.

4.4.2 Nanostructure Growth Studies

To elucidate the effect of surface diffusion for the resulting nanostructure we performed a series of chromium depositions in UHV with grids and colloids acting as mechanical masks. The idea is that one can measure the edge of the structure cast by the shadow of the mask to deduce the diffusion of chromium atoms after deposition.

Using a colloid monolayer as lithographic mask provides an extremely well-defined experimental situation for the determination of nanostructure growth. With our transversally laser-cooled atomic beam whose collimation is around 1mrad and the colloidal mask made of polystyrol colloids with a diameter of 1500nm on top of the silicon substrate, one expects from geometrical considerations that the nanostructures formed will exhibit very sharp edges with widths smaller then 1nm.

The colloidal masks used here were produced by J. Boneberg from the group of Prof. Leiderer at the University of Konstanz. Therefore, spherical polystyrene or glass spheres with diameters of 1500nm and 800nm were used to form lithographic masks on surfaces. When a droplet of the colloidal suspension is placed on a substrate, the masks form independently via a self-organized process upon solvent evaporation. The masks consist of hexagonally arranged mono- and bilayers of these particles (Burmeister *et al.*, 1997).

In figure 4.29(a) the experimental scheme is depicted. The laser cooled atomic beam impinges perpendicularly onto the substrate with the colloidal mask on top. The top

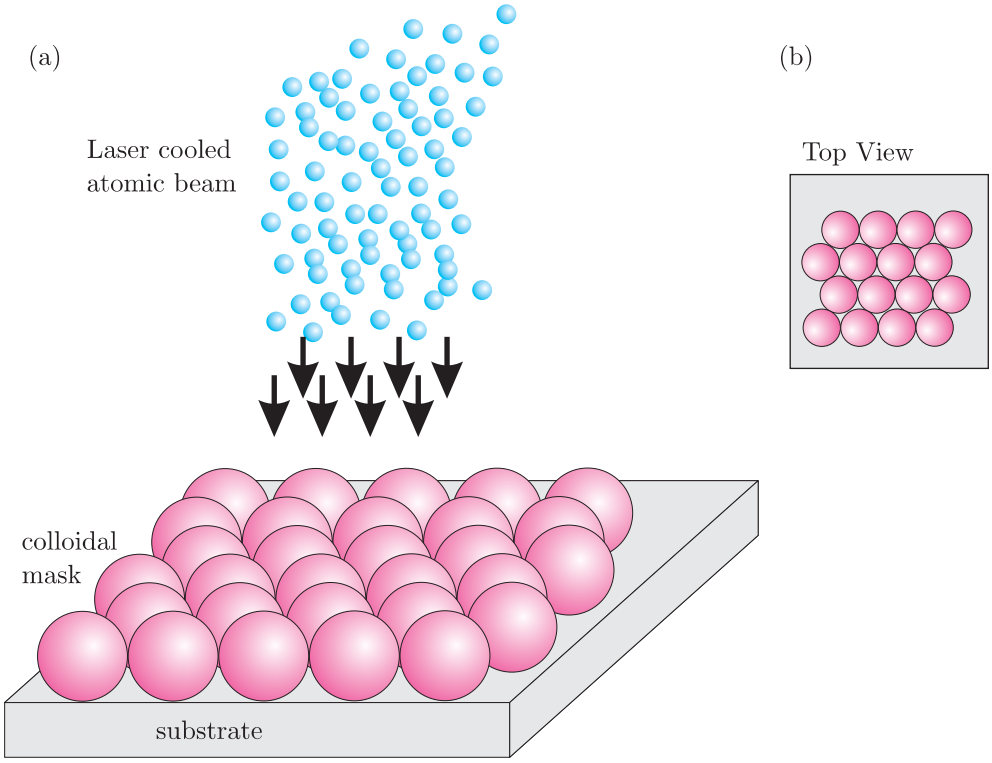

Figure 4.29: (a) Scheme of nanostructure fabrication using a colloidal mask. A collimated atomic chromium beam impinges perpendicularly on the mechanical mask made of polystyrol

view of the substrate with the self-assembled mask shown in figure 4.29(b) shows the hexagonal pattern formed. Besides the fact that we used a highly collimated atomic beam the procedure is analogous to the one described in (Boneberg *et al.*, 1997). After a deposition time of 30 minutes the sample was taken out of the vacuum chamber and the colloids were removed. Two methods were therefore applied: first, the mask was removed with an ultrasonic bath and second, an adhesive tape was used to lift off the colloids. Both methods proved equally successful.

The remaining chromium structure on the substrate that constitute the negative of the mask were then analyzed with an AFM. A $2 \times 2\mu m^2$ section of the topography of a sample fabricated with 800nm colloids is shown in figure 4.30(a).

Several triangular Cr structures as well as larger islands can be observed. Furthermore, the contours of the spheres are apparent. A zoom from a triangular nanostructure is shown in figure 4.30(b) and cross sections through this Cr island are shown in figure 4.30(c). One can see, that the edge of the nanostructure is not as sharp as the geometrical considerations suggest. The edge widths are approximately 30-40nm in horizontal direction and 50-60nm in vertical direction, i.e. much broader than the incident transversal velocity of the atoms implies. The atomic beam is laser cooled only in horizontal direction but not vertically. Nevertheless, the beam is collimated below 2mrad due to the differential pumping stage that acts as a collimation slit.

This finding is a strong indication for surface diffusion of chromium atoms and a

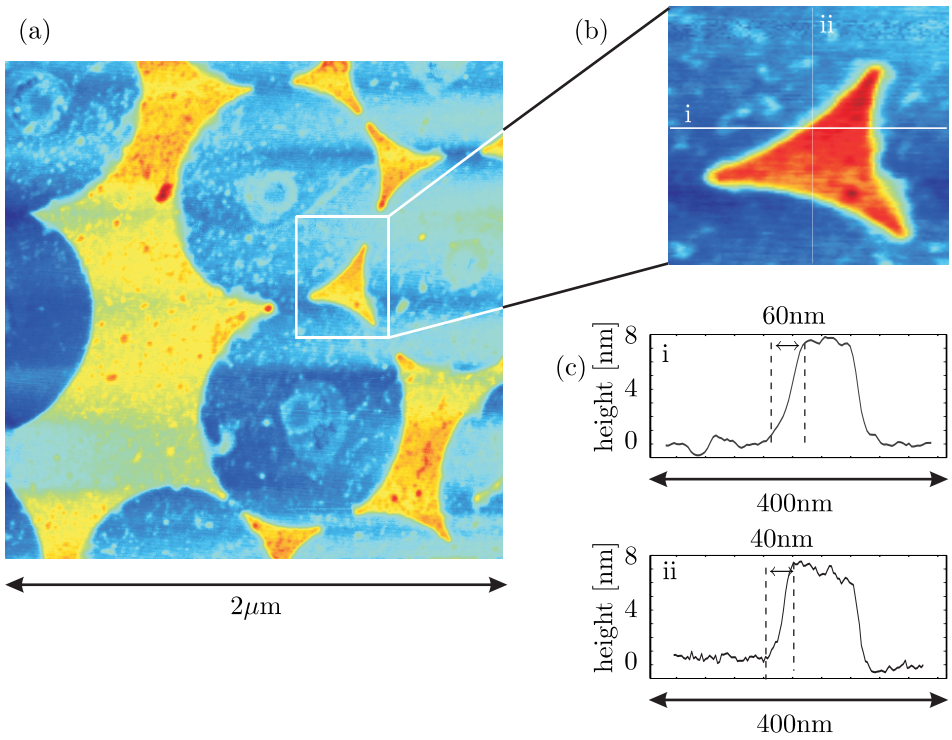

Figure 4.30: Structure obtained from deposition through a colloidal mask. The colloids' diameter was 800nm. (a) AFM picture and (b) zoom into remaining triangular structure. (c) Cross sections through upper image. The nanostructure edges have widths of 40nm (i) and 60nm (ii).

subsequent broadening effect of the resulting nanostructures. Thus, the observations made in the McClelland group can be confirmed by our experiment, however, our results imply that even in the UHV range surface diffusion is present and leads to a feature broadening on the order of 30nm. On the other hand, we cannot confirm the predictions made by the barrier-limited surface diffusion theory. But we cannot quantify the effect of surface pollution which might play a role in the colloidal mask depositions.

To avoid any contamination effects from the colloids themselves or the removal procedure we made further mechanical mask depositions with TEM grids mounted above the substrate surface. Similarly, as in the experiment performed for the determination of the structure background, the well-collimated chromium beam was deposited for 30 minutes through a copper lattice with a 10μm pitch. The grid was about 0.5mm above the silicon substrate surface.

The AFM measurement and corresponding cross sections are depicted in figure 4.31. Surprisingly, the chromium square does not immediately fall off towards the substrate near its edge. On the contrary, the edges reveal a pronounced ridge that can become more than double the plateau height.

This effect is only observed with silicon and germanium substrates, but not with glass or sapphire[16]. This implies a growth phenomenon that originates from the substrate

[16]Hence, the deposition for the background measurement in the previous section was made onto a sapphire substrate because the nanostructures were completely smeared out on silicon.

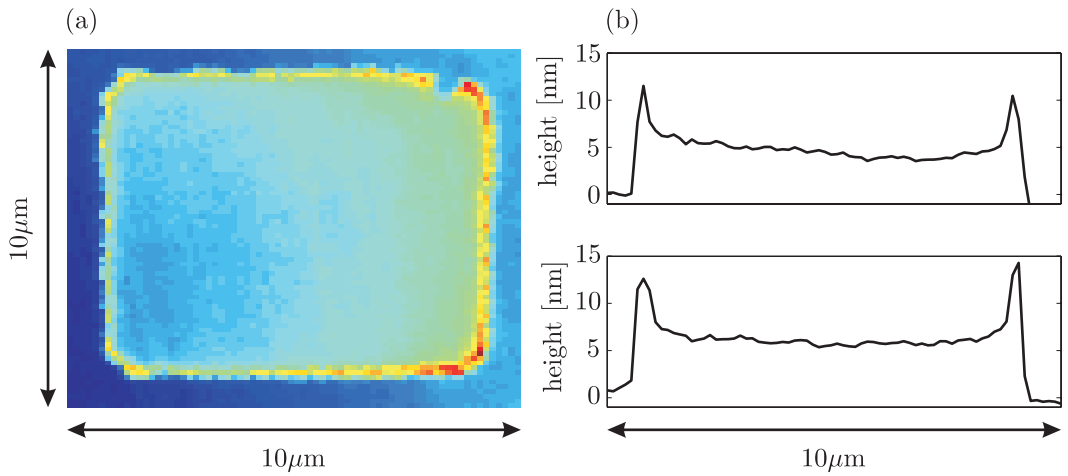

Figure 4.31: Structure obtained from deposition through a copper lattice. (a) AFM picture and (b) cross sections. Along the edge of the chromium square the plateau is superelevated. These superelevations can become more than twice as large as the plateau height.

chromium interface. Furthermore, we observed that this effect is amplified with growing lattice-substrate spacing. In turn, from that one might deduce that the chromium lattice exerts a force on the incident atoms and it is not a growth effect. But this force only acts on the atoms when the substrate is either made of silicon or germanium. An estimate of the force on the atoms suggests that the acceleration is on the order of $10^7 \frac{\mathrm{m}}{\mathrm{s}^2}$ when one assumes that the force acts only between lattice and substrate. The only forces that appear to be realistic are either from electric ore magnetic fields, but it is absolutely unrealistic that fields of this order of magnitude are present. Van der Waals forces are also unrealistic because they should be independent of the substrate material.

In any case, these results remain quite puzzling and suggest that further studies are necessary to understand the growth processes that might lead to either a broadening or a reduced surface diffusion of chromium in the UHV case. Moreover, it is not clear what causes these ridges to grow on nanostructures fabricated with mechanical grids.

5 Summary and Outlook

5.1 Summary

The goal of this thesis work was devoted to three major problems:

We were interested in the extension of the previously studied classical schemes of atomic nanofabrication to the unexplored quantum regime where the formation of nanostructures cannot be understood in the classical picture of the induced dipole force.

Secondly, we were working towards the fabrication of ferrimagnetic nanoalloys. For this purpose, the apparatus was rebuilt so that the nanostructures can be now grown under defined ultra high vacuum conditions. In addition, compatibility with the MBE machine in the group of Professor Schatz was ensured because our experimental scheme requires that the samples are transferred between both vacuum apparatus.

Thirdly, this step towards real applications of nanostructures fabricated with light forces required in particular the development of a reliable and reproducible scheme. For this purpose systematic measurements that allow to optimize the relevant parameters of the deposited structures, the feature width and the background called pedestal, were performed.

We have demonstrated for the first time that exactly resonant standing wave light fields can be utilized to halve the standard two-level atom periodicity limit of $\frac{\lambda}{2}$. Here we make use of the fact that an atomic ground state wave packet in a resonant light field splits into a fifty-fifty superposition of the new eigenstates (dressed states) of the coupled system. In an inhomogeneous intensity distribution like a standing wave the motion of both dressed state wave packets is primarily governed by their associated potentials that only differ in sign. The dressed state wave packets are therefore accelerated into opposite directions, one to the intensity maximum and the other to the minimum. The advantage of the method is its applicability to basically all atomic or molecular species that can be prepared in an effective two-level system. Our experimental studies of this scheme furthermore show that the atomic motion in resonant light fields is not only governed by the intensity gradient of the light field distribution but also by the phase gradient near the nodes of an imperfect standing light wave (Jürgens *et al.*, 2004).

For the fabrication of ferrimagnetic nanostructures and other applications it is desirable to produce structures with a high contrast, i.e. to reduce the background of the structures. We were able to show that using red detuned standing light waves is advantageous over the usually used blue detuned standing waves because their potential shape is distinctly more harmonic. This advantage even surpasses the negative influence of spontaneous emissions that naively suggests that blue detuned standing waves are more appropriate. We measured that the feature background is suppressed to at least 13% and found excellent agreement with results obtained from Monte-Carlo simulations

based on optical Bloch equations.

With the knowledge at hand to produce high contrast nanostructures we were able to produce clean chromium samples under UHV conditions and transfer them under vacuum into the MBE machine. There, a platinum layer was deposited on top so that ferrimagnetic nanoalloys can now be made when the thermal annealing process succeeds. Unfortunately, technical problems in the epitaxial chamber prevented this important step to date.

5.2 Outlook

After the experimental work of this thesis was finished, the experiment was completely dismantled and moved to the University of Stuttgart where it will be rebuilt for new experiments. It is now being continued in the group of Tilman Pfau. The former diploma student on this experiment Alexander Greiner is currently planning new exciting nanofabrication experiments.

The experimental realization of Bose-Einstein condensation (BEC) reviewed in (Ketterle, 2002) and the first demonstrations of an atom-laser (Mewes *et al.*, 1997; Bloch *et al.*, 1999, 2001) has lead to a real boom in atom optics comparable to the invention of optical lasers. Experiments and devices whereof no one had dared to dream ten years ago seem to come into reach. The availability of a coherent matter wave source with short de Broglie wavelengths will enable researchers to drive the field of atomic nanofabrication to ultimate resolutions determined by the diffraction limit and thus structure widths below 10nm might be achievable. In order to achieve short de Broglie wavelengths of around 1nm, the BEC must be accelerated to velocities of around $10\frac{\mathrm{m}}{\mathrm{s}}$. This is difficult to realize by gravity, but using Bragg pulses to accelerate the BEC might be a convenient solution (Kozuma *et al.*, 1999; Eiermann *et al.*, 2003, 2004). Coherent atom optics will also increase its attractiveness when holographic masks for the generation of arbitrary submicron structures become available (Morinagaa *et al.*, 1996; Shimizu and Fujita, 2002). However, the flux of current atom lasers is still many orders of magnitude too small to attain nanostructures at realistic deposition timescales that are comparable in height with our structures. But even with small atom numbers some highly interesting novel techniques for nanotechnology are conceivable:

In particular the recent demonstration of a Mott insulator transition in ultracold atomic gases holds great potential for driving atomic nanofabrication to the single particle limit. (Greiner *et al.*, 2002; Köhl *et al.*, 2004). In a Mott insulator state, exact numbers of atoms are localized at individual lattice sites of a periodic potential. It can be realized by superimposing a BEC with a three dimensional optical dipole potential by adiabatically increasing the intensity of the lattice laser beams. When the potential depth exceeds a certain value, tunnelling between adjacent lattice sites is suppressed and the total energy of the system is minimized when each lattice site is filled with exactly the same number of atoms. Such a state with defined atom numbers arranged in a perfectly periodic array is highly attractive, in particular when each lattice site is filled with exactly one atom. The ability to deposit one layer of such an ordered array of atoms onto a surface represents a scheme for the ultimate nanofabrication device. This scheme has an enormous advantage over scanning probe techniques where individual atoms can be arbitrarily placed (Eigler and Schweitzer, 1990; Manoharan *et al.*, 2000). It founds

in the possibility to arrange in a controlled way hundreds of thousands or even millions of single atoms simultaneously in a periodic array.

Kane proposed such a square lattice array of atoms for the realization of a solid state quantum computer (Kane, 1998). He suggests that the nuclear spins of ^{31}phosphorus dopant atoms buried inside a silicon crystal directly beneath a metal contact that acts as a gate, can be used as qubits. At temperatures near absolute zero (100mK) the donor electron of phosphorus is weakly bound to the phosphorus ion and its spin can influence the state of the nuclear-spin qubit. By applying a gate voltage the electron is polarized and changes its overlap with the donor nucleus and the relative energies of the two spin states. A radio-frequency signal can thus be used to flip the spins. The associated coupling of neighboring electrons influenced by other gates leads to an entanglement with neighboring atomic qubits and can thus be used for quantum computing. This scheme is based explicitly on the condition that each lattice site on the surface is occupied by exactly one donor atom, a requirement that cannot be fulfilled with standard lithography techniques.

The realization of the single atom deposition scheme is currently pursued by Alexander Greiner with our chromium apparatus. On the way, many technical difficulties must be overcome, especially the fact that Bose condensation of chromium is not yet achieved. But lots of progress was made recently (Schmidt *et al.*, 2003; Hensler *et al.*, 2003), and they hope to reach BEC with a similar technique as recently applied in the successful Bose condensation of cesium (Weber *et al.*, 2003).

Furthermore, it will be interesting to see how applications of atomic nanofabrication in its conventional scheme will develop. In particular the structured doping method in combination with epitaxial growth holds large potential for the fabrication of novel nanostructured materials. The most promising material systems are the heterostructure semiconductor materials aluminum gallium arsenide (AlGaAs) or indium aluminum arsenide (InAlAs). Modulating the composition of the materials at periodicities might significantly alter the electronic and optical properties of the materials.

Bibliography

W. R. Anderson, C. C. Bradley, J. J. McClelland, and R. J. Celotta. Minimizing feature width in atom optically fabricated chromium nanostructures. Phys. Rev. A **59**, 2476 (1999).

A. Aspect, J. Dalibard, A. Heidmann, C. Salomon, and C. Cohen-Tannoudji. Cooling Atoms with Stimulated Emission. Phys. Rev. Lett. **57**, 1688 (1986).

K. K. Berggren, A. Bard, J. L. Wilbur, J. D. Gillaspy, A. G. Helg, J. J. McClelland, S. L. Rolston, W. D. Phillips, M. Prentiss, and G. M. Whitesides. Microlithography by using neutral metastable atoms and self-assembled monolayers. Science **269**, 1255 (1995).

J. E. Bjorkholm, R. R. Freeman, A. Ashkin, and D. B. Pearson. Observation of Focussing of Neutral Atoms by the Dipole Forces of Resonance-radiation Pressure. Phys. Rev. Lett. **41**, 1361 (1978).

I. Bloch, T. Hänsch, and T. Esslinger. Atom Laser with a cw Output Coupler. Phys. Rev. Lett. **82**, 3008 (1999).

I. Bloch, M. Köhl, M. Greiner, T. Hänsch, and T. Esslinger. Optics with an Atom Laser Beam. Phys. Rev. Lett. **87**, 030401 (2001).

J. Boneberg, F. Burmeister, C. Schäfle, P. Leiderer, D. Reim, A. Fery, and S. Herminghaus. The Formation of Nano-Dot and Nano-Ring Structures in Colloidal Monolayer Lithography. Langmuir **13**, 7080 (1997).

R. Bosch. *Ferromagnetic Nanostructures by Laser Manipulation.* Ph.D. thesis, Eindhoven University of Technology (2002).

R. M. Bradley, A. Eschmann, and S. A. Lee. Theory of feature broadening in direct-write optical lithography. J. Appl. Phys. **88**, 3316 (2000).

B. Brezger. *Neue Lichtmasken in der Atomlithographie.* Ph.D. thesis, Universität Konstanz (1999).

B. Brezger, T. Schulze, U. Drodofsky, J. Stuhler, S. Nowak, T. Pfau, and J. Mlynek. Nanolithography with neutral chromium and helium atoms. J. Vac. Sci. Technol. B **15**, 2905 (1997).

B. Brezger, T. Schulze, P. O. Schmidt, R. Mertens, T. Pfau, and J. Mlynek. Polarization gradient light masks in atom lithography. Europhys. Lett. **46**, 148 (1999).

F. Burmeister, C. Schäfle, T. Matthes, M. Böhmisch, J. Boneberg, and P. Leiderer. Colloid Monolayers as Versatile Lithographic Masks. Langmuir **13**, 2983 (1997).

J. Chen, J. Story, and R. G. Hulet. Evolution of atomic motion in an intense standing wave. Phys. Rev. A **47**, 2128 (1993).

C. Cohen-Tanoudji, J. Dupont-Roc, and G. Grynberg. *Atom-Photon Interactions*. John Wiley & Sons (1992).

R. J. Cook. Optical Stern-Gerlach effect. Phys. Rev. A **35**, 3844 (1987).

K. Corwin, Z.-T. Lu, C. Hand, R. Epstein, and C. Wieman. Frequency-stabilized diode laser with the Zeeman shift in an atomic vapor. Appl. Opt. **37**, 3295 (1998).

J. Dalibard, Y. Castin, and K. Mølmer. Wave-Function Approach to Dissipative Processes in Quantum Optics. Phys. Rev. Lett. **68**, 580 (1992).

J. Dalibard and C. Cohen-Tannoudji. Dressed-atom approach to atomic motion in laser light: the dipole force revisited. J. Opt. Soc. Am. B **2(11)**, 1707 (1985).

J. Dalibard and C. Cohen-Tannoudji. Laser cooling below the Doppler limit by polarization gradients: simple theoretical models. J. Opt. Soc. Am. B **6**, 2023 (1989).

W. Demtröder. *Laser Spectroscopy*. Springer-Verlag, 3 edition (2003).

R. Dersch, T. Liu, A. Schaper, A. Greiner, and J. Wendorff. Electrospun nanofibers: Internal structure and intrinsic orientation. J. Polym. Sci. B **41**, (4), 545 (2003).

M. Drewsen, U. Drodofsky, C. Weber, C. Maus, G. Schreiber, and J. Mlynek. Sisyphus polarisation gradient laser cooling of Cr-atoms on the $4s^7S_3 \rightarrow 4p^7P_{2,3,4}$ transition. J. Phys. B: At. Mol. Opt. Phys. **29**, L843 (1996).

U. Drodofsky. *Atomlithographie mit Lichtkräften*. Ph.D. thesis, Universität Konstanz (1997).

U. Drodofsky, J. Stuhler, B. Brezger, T. Schulze, M. Drewsen, T. Pfau, and J. Mlynek. Nanometerscale Lithography with Chromium Atoms using Light Forces. Microelectron. Eng. **35**, 285 (1997a).

U. Drodofsky, J. Stuhler, T. Schulze, M. Drewsen, B. Brezger, T. Pfau, and J. Mlynek. Hexagonal nanostructures generated by light masks for neutral atoms. Appl. Phys. B **65**, 755 (1997b).

M. Efremov, M. Fedorov, V. Yakovlev, and W. Schleich. Dynamical suppression of radiative decay via atomic deflection by a standing light wave. Laser Physics **13**, 995 (2003).

B. Eiermann, T. Anker, M. Albiez, M. Taglieber, P. Treutlein, K.-P. Marzlin, and M. Oberthaler. Bright Bose-Einstein Gap Solitons of Atoms with Repulsive Interaction. Phys. Rev. Lett. **92**, 230401 (2004).

B. Eiermann, P. Treutlein, T. Anker, M. A. M. Taglieber, K.-P. Marzlin, and M. Oberthaler. Dispersion management for atomic matter waves. Phys. Rev. Lett. **91**, 060402 (2003).

D. Eigler and E. Schweitzer. Positioning single atoms with a scanning tunnelling microscope. Nature **344**, 524 (1990).

J. Fleischhauer. Der Millionstel-Markt. DER SPIEGEL **23** (2004).

R. Frisch. Experimenteller Nachweis des Einsteinschen Strahlungsrückstoes. Z. Phys. **86**, 42 (1933).

W. Gerlach and O. Stern. Der experimentelle Nachweis des magnetischen Moments des Silberatoms. Z. Phys. **8**, 110 (1921).

A. Greiner. *Optimierte Lichtmasken für Atomlithographie zur Erzeugung magnetischer Nanostrukturen*. Diploma thesis, Universität Konstanz (2003).

M. Greiner, O. Mandel, T. Esslinger, T. Hänsch, and I. Bloch. Quantum phase transition from a superfluid to a Mott insulator in a gas of ultracold atoms. Nature **415**, 39 (2002).

R. Gupta, J. J. McClelland, Z. J. Jabour, and R. J. Celotta. Nanofabrication of a two-dimensional array using laser-focused atomic-deposition. Appl. Phys. Lett. **67**, 1378 (1995).

R. Gupta, J. J. McClelland, P. Marte, and R. J. Celotta. Raman-Induced Avoided Crossings in Adiabatic Optical Potentials: Observation of $\lambda/8$ Spatial Frequency in the Distribution of Atoms. Phys. Rev. Lett. **76**, 4689 (1996).

A. Habenicht. *Resonante Lichtmasken zur Erzeugung von Chrom-Nanostrukturen*. Diploma thesis, Universität Konstanz (2003).

T. W. Hänsch and B. Couillaud. Laser frequency stabilization by polarization spectroscopy of a reflecting reference cavity. Opt. Comm. **35**, 441 (1980).

S. Hensler, J. Werner, A. Griesmaier, P. Schmidt, A. Görlitz, T. Pfau, S. Giovanazzi, and K. Rzazewski. Dipolar Relaxation in an ultra-cold Gas of magnetically trapped chromium atoms. Appl. Phys. B **77**, 765 (2003).

E. Jurdik. *Laser manipulation of atoms and nanofabrication*. Ph.D. thesis, University of Nijmegen (2001).

E. Jurdik, J. Hohlfeld, H. van Kampen, T. Rasing, and J. J. McClelland. Laser-focused nanofabrication: Beating of two atomic resonances. Appl. Phys. Lett. **80**, 4443 (2002).

E. Jurdik, T. Rasing, H. van Kampen, C. C. Bradley, and J. J. McClelland. Surface growth in laser-focused atomic deposition. Phys. Rev. B **60**, 1543 (1999).

D. Jürgens, A. Greiner, R. Stützle, E. te Sligte, A. Habenicht, and M. Oberthaler. Quantum features in atomic nanofabrication using exactly resonant standing waves. submitted to Phys. Rev. Lett. (2004).

B. Kane. A silicon-based nuclear spin quantum computer. Nature **393**, 133 (1998).

W. Ketterle. Nobel lecture: When atoms behave as waves: Bose-Einstein condensation and the atom laser. Rev. Mod. Phys. **74**, 1131 (2002).

M. Köhl, H. Moritz, T. Stöferle, C. Schori, and T. Esslinger. Superfluid to Mott insulator transition in one, two, and three dimensions. arXiv:cond-mat **0404338** (2004).

M. Kozuma, L. Deng, E. Hagley, J. Wen, R. Lutwak, K. Helmerson, S. Rolston, and W. Phillips. Coherent Splitting of Bose-Einstein Condensed Atoms with Optically Induced Bragg Diffraction. Phys. Rev. Lett. **82**, 871 (1999).

C. J. Lee. Quantum-mechanical analysis of atom lithography. Phys. Rev. A **61**, 63604 (2000).

H. Manoharan, C. Lutz, and D. Eigler. Quantum mirages formed by coherent projection of electronic structure. Nature **403**, 512 (2000).

O. Marago. private communication (2003).

M. Maret, M. Albrecht, J. Köhler, R. Poinsot, C. Ulhaq-Bouillet, J. Tonnerre, J. Berar, and E. Bucher. Magnetic anisotropy and chemical long-range order in epitaxial ferrimagnetic $CrPt_3$ films. J. Magn. Magn. Mater. **218**, 151 (2000).

P. Marte, R. Dum, R. Taïeb, P. D. Lett, and P. Zoller. Quantum wave function simulation of the resonance fluorescence spectrum from one-dimensional optical molasses. Phys. Rev. Lett. **71**, 1335 (1993).

T. Massalski, editor. *Binary Alloy Phase Diagrams*, volume I,II, and III. William B. Scott, Jr., 2nd edition (1996).

J. J. McClelland. Atom-optical properties of a standing-wave light field. J. Opt. Soc. Am. B **12**, 1761 (1995).

R. Mertens. *Physikalische Grenzen der Atomlithographie mit Chrom*. Diploma thesis, Universität Konstanz (1999).

D. Meschede and H. Metcalf. Atomic nanofabrication: atomic deposition and lithography by laser and magnetic forces. J. Phys. D: Appl. Phys. **36**, R17 (2003).

M.-O. Mewes, M. Andrews, D. Kurn, D. Durfee, C. Townsend, and W. Ketterle. Output Coupler for Bose-Einstein Condensed Atoms. Phys. Rev. Lett. **78**, 582 (1997).

B. R. Mollow. Power Spectrum of Light Scattered by Two-Level Systems. Phys. Rev. **188**, 1969 (1969).

G. Moore. Electronics Magazine **38**, 114 (1965).

M. Morinagaa, M. Yasuda, T. Kishimoto, F. Shimizu, J. Fujita, and S. Matsui. Holographic Manipulation of a Cold Atomic Beam. Phys. Rev. Lett. **77**, 802 (1996).

M. Mützel, S. Tandler, D. Haubrich, D. Meschede, K. Peithmann, M. Flaspöhler, and K. Buse. Atom Lithography with a Holographic Light Mask. Phys. Rev. Lett. **88**, 083601 (2002).

M. Oberthaler and T. Pfau. One-, two- and three-dimensional nanostructures with atom lithography. J. Phys.: Condens. Matter **15**, R233 (2003).

T. Petelski, M. Fattori, G. Lamporesi, J. Stuhler, and G. Tino. Doppler-free spectroscopy using magnetically induced dichroism of atomic vapor: a new scheme for laser frequency locking. Eur. Phys. J. D **22**, 279 (2003).

S. J. H. Petra, L. Feenstra, W. Hogervorst, and W. Vassen. Nano-lithography with metastable helium atoms in a high-power standing-wave light field. Appl. Phys. B **78**, 133 (2004).

W. D. Phillips and H. Metcalf. Laser Deceleration of an Atomic Beam. Phys. Rev. Lett. **48**, 596 (1982).

S. Rehse, R. McGowan, and S. Lee. Optical manipulation of group III atoms. Appl. Phys. B **70**, 657 (2000).

S. J. Rehse, W. M. F. Jr., and S. A. Lee. Measurement of the hyperfine structure of the $4d^2D_{3/2,5/2}$ levels and isotope shifts of the $4p^2P_{3/2} \rightarrow 4d^2D_{3/2}$ and $4p^2P_{3/2} \rightarrow 4d^2D_{5/2}$ transitions in gallium 69 and 71. J. Opt. Soc. Am. B **18**, 855 (2001).

C. Salomon, J. Dalibard, A. Aspect, H. Metcalf, and C. Cohen-Tannoudji. Channeling atoms in a laser standing wave. Phys. Rev. Lett. **59**, 1659 (1987).

P. Schmidt, S. Hensler, J. Werner, A. Griesmaier, A. Görlitz, T. Pfau, and A. Simoni. Determination of the s-wave Scattering Length of Chromium. Phys. Rev. Lett. **91**, 193201 (2003).

P. O. Schmidt. *Lichtmasken in der Atomlithographie*. Diploma thesis, Universität Konstanz (1998).

R. E. Scholten, R. Gupta, J. J. McClelland, R. J. Celotta, M. S. Levenson, and M. G. Vangel. Laser collimation of a chromium beam. Phys. Rev. A **55**, 1331 (1997).

T. Schulze. *Nanostrukturierung mit Lichtkräften*. Ph.D. thesis, Universität Konstanz (2000).

T. Schulze, B. Brezger, R. Mertens, M. Pivk, T. Pfau, and J. Mlynek. Writing a superlattice with light forces. Appl. Phys. B **70**, 671 (2000).

T. Schulze, B. Brezger, P. O. Schmidt, R. Mertens, A. S. Bell, T. Pfau, and J. Mlynek. Sub-100 nm Structures by Neutral Atom Lithography. Microelectron. Eng. **46**, 105 (1999).

T. Schulze, T. Müther, D. Jürgens, B. Brezger, M. K. Oberthaler, T. Pfau, and J. Mlynek. Structured doping with light forces. Appl. Phys. Lett. **78**, 1781 (2001).

F. Shimizu and J. Fujita. Reflection-Type Holograms for Atoms. Phys. Rev. Lett. **88**, 123201 (2002).

SIA. *The international technology roadmap for semiconductors* (2003).

T. Sleator, T. Pfau, V. I. Balykin, O. Carnal, and J. Mlynek. Experimental Demonstration of the Optical Stern-Gerlach Effect. Phys. Rev. Lett. **68**, 1996 (1992).

J. Stuhler. *Atomlithographie mit Chrom*. Diploma thesis, Universität Konstanz (1996).

J. Stuhler. *Kontinuierliches Laden einer Magnetfalle mit lasergekühlten Chromatomen*. Ph.D. thesis, Universität Konstanz (2001).

R. Stützle. *Atomlithographie mit dissipativen Lichtmasken*. Diploma thesis, Universität Konstanz (2001).

R. Stützle, D. Jürgens, A. Habenicht, and M. Oberthaler. Dissipative light masks for atomic nanofabrication. J. Opt B **5**, S164 (2003).

E. te Sligte. private communication (2004).

E. te Sligte, K. M. R. van der Stam, B. Smeets, P. van der Straten, R. E. Scholten, H. C. W. Beijerinck, and K. A. H. van Leeuwen. Barrier-limited surface diffusion in atom lithography. J. Appl. Phys. **95**, 1749 (2004).

G. Timp, R. Behringer, D. Tennant, J. Cunningham, M. Prentiss, and K. Berggren. Using Light as a Lens for Submicron, Neutral-Atom Lithography. Phys. Rev. Lett. **69**, 1636 (1992).

C. Weber. *Lichtdruck-Lithographie mit Atomen*. Diploma thesis, Universität Konstanz (1995).

T. Weber, J. Herbig, M. Mark, H.-C. Nägerl, and R. Grimm. Bose-Einstein Condensation of Cesium. Science **299**, 232 (2003).

C. Wieman and T. W. Hänsch. Doppler-free Polarization Spectroscopy. Phys. Rev. Lett. **36**, 1170 (1976).

Danksagung

Zu guter Letzt möchte ich mich noch bei allen Personen bedanken, ohne die diese Arbeit nicht möglich gewesen wäre:

- Prof. Markus Kurt Oberthaler für die herausragende Betreuung an dem von ihm 'geerbten' Experiment. Durch sein Engagement und seine Begeisterung für Atome in stehenden Lichtwellen hat er es immer wieder geschafft für neue Motivation zu sorgen, auch wenn mal wieder kein Licht am Ende des Tunnels oder Chromatome auf dem Substrat zu sehen war.
- Prof. Jürgen Mlynek für die Aufnahme in seinen Lehrstuhl im Sommer 1999. Auch nach seinem Weggang in die Hauptstadt hat er nie den Draht zur Atomlithographie verloren, und ohne seinen Riecher zu Beginn des Experiments wäre es auch nie zu dieser Arbeit gekommen. Insbesondere danke ich ihm für viele lehrreiche und vor allem anwendbare Aphorismen.
- Prof. Paul Leiderer, der sich bereit erklärt hat die vorliegende Arbeit zu begutachten und für die großzügige Bereitstellung des AFM's.
- Johannes Boneberg für die schönen Kolloidmasken zur Messung des Chromwachstums.
- Meinen Diplomanden und Mitstreitern bei der 'horizontalen Verdampfung hochschmelzender Materialien' Ralf Stützle, Alexander Greiner und Anja Habenicht. Ohne Ralf gäbe es bei weitem nicht so viel blaues Licht mit dem natürlich vieles leichter fällt. Außerdem danke ich ihm für die große Geduld beim Erklären der Feinheiten der Atom-Licht Wechselwirkung. Zudem musste er mit mir die längste Durststrecke des Experiments durchmachen, ich denke da nur an die regelmäßigen Besuche von Herrn Glatz von Coherent. Ohne Alex hätte das ganze komplizierte Handling der Proben im UHV nie so geklappt, weil ich wohl die Hälfte hätte fallen lassen, und die besten Ergebnisse lägen vielleicht jetzt noch im Cube. Anja danke ich für das Design der UHV-Kammer.
- Meinen Litho-Kollegen der ersten Monaten Thomas und Tobias für die spannenden Arbeiten zur strukturierten Dotierung.
- Allen Mitgliedern der 'matterwave optics' Gruppe, die mit Rat und Tat zur Seite standen und auch stets großzügig beim Teilen des Equipments waren, als da wären: Bernd Eiermann, Thomas Anker, Michael Albiez, Martin Störzer, Martin Göbel, Matthias Taglieber, Phillip Treutlein, Karen Forberich, Igor Mourachko und Mary-Jo Bellanca.

- Den anderen Chromis Sven, Jürgen, Piet, Björn und Jörg für zahlreiche Tipps zu Spektroskopie und Geheimnissen des Chroms. Jürgen habe ich die Idee mit dem DAVLL-Lock zu verdanken.

- Unserem Holländer Edwin te Sligte, der als 'Nanofab'-Austauschwissenschaftler die Anfangszeit der On-Resonance Experimente miterlebte und zu den ersten wichtigen Einsichten zur Rolle des Phasengradienten beigetragen hat.

- Onofrio Maragò für die Entwicklung der On-Resonance Strategien und das Wickeln von Wolfram-Drähten zum Eigenbau eines Chromofens.

- Prof. Oliver Benson, Prof. Achim Peters und Prof. Jürgen Mlynek für das Gästebüro an der Humboldt-Universität zu Berlin, mitsamt der Möglichkeit der Nutzung der Infrastruktur während der Zeit des Zusammenschreibens.

- Allen nichtwissenschaftlichen Mitarbeitern und guten Seelen der Universität Konstanz, die unser Forschen erst ermöglichen, insbesondere danken möchte ich der 'Task Force' von P8: Ute Hentzen für ihre unkomplizierte und stets hilfsbereite Art, Stefan Hahn für seine Hilfe bei allen Problemen innerhalb und außerhalb des Labors, Stefan Eggert für viele wunderbare Lockboxen, sowie Herrn Jauch aus der Werkstatt für seine ausgeklügelten präzisionsmechanischen Meisterwerke.

Am Schluss möchte ich meiner Familie und meinen Freunden für die Unterstützung und Aufmunterung während der letzten Jahre danken.

Und der größte Dank gebührt natürlich meiner Alexandra, die über all die Jahre so viel Geduld bewiesen hat. Erst durch sie sind die letzten Jahre für mich zu einer solch wunderbaren Zeit geworden.